

Structural Investigations on layered Manganites and Ruthenates

Olaf Jochen
Schumann

Structural Investigations on layered Manganites and Ruthenates

Inaugural Dissertation

zur

Erlangung des Doktorgrades
der Mathematisch-Naturwissenschaftlichen Fakultät
der Universität zu Köln

vorgelegt von

Olaf Jochen Schumann

aus Leverkusen

Köln, 2010

Dieses Arbeit stellt eine von der Mathematisch-Naturwissenschaftlichen Fakultät der Universität zu Köln angenommene Dissertation dar.

Berichterstatter: Prof. Dr. M. Braden
Priv.-Doz. Dr. J. Hemberger

Vorsitzender
der Prüfungskommission: Prof. Dr. U. Ruschewitz

Tag der mündlichen Prüfung: 15. Januar 2010

Bibliografische Information der *Deutschen Nationalbibliothek*

Die Deutsche Nationalbibliothek verzeichnet diese Publikation in der Deutschen Nationalbibliografie; detaillierte bibliografische Daten sind im Internet über <<http://dnb.ddb.de>> abrufbar.

ISBN: 978-3-86664-848-7

Zugl.: Köln, Univ., Diss., 2010

Dissertation, Universität zu Köln

Dieses Werk ist urheberrechtlich geschützt.

Alle Rechte, auch die der Übersetzung, des Nachdruckes und der Vervielfältigung des Buches, oder Teilen daraus, vorbehalten. Kein Teil des Werkes darf ohne schriftliche Genehmigung des Verlages in irgendeiner Form reproduziert oder unter Verwendung elektronischer Systeme verarbeitet, vervielfältigt oder verbreitet werden.

Die Wiedergabe von Gebrauchsnamen, Warenbezeichnungen, usw. in diesem Werk berechtigt auch ohne besondere Kennzeichnung nicht zu der Annahme, dass solche Namen im Sinne der Warenzeichen- und Markenschutz-Gesetzgebung als frei zu betrachten wären und daher von jedermann benutzt werden dürfen.

This document is protected by copyright law.

No part of this document may be reproduced in any form by any means without prior written authorization of the publisher.

Alle Rechte vorbehalten | all rights reserved

© Mensch und Buch Verlag 2010

Choriner Str. 85 - 10119 Berlin

verlag@menschundbuch.de – www.menschundbuch.de

*Et is wie et is,
et kütt wie et kütt
un et hätt noch immer jot jejang!*

§§1-3, KölschGG

Contents

1	Introduction	1
2	Fundamentals	3
2.1	Temperature depended Powder Diffractometry	4
2.2	Single Crystal Diffraction	6
2.3	Data Integration of HeiDi Measurements	8
2.4	Cell choices for Manganite Structures	8
3	Crystal and magnetic structure of layered manganites	11
3.1	Preparation of poly- and single-crystalline samples	12
3.2	Crystal structure of charge-ordered $\text{La}_{0.5}\text{Sr}_{1.5}\text{MnO}_4$	17
3.2.1	Charge and Orbital ordering	18
3.2.2	Charge and Orbital ordering in the magnetically ordered phase	23
3.2.3	Crystal structure from X-ray single diffraction	25
3.2.4	Magnetic order at low temperatures	27
3.3	Ruthenium co-doping	34
3.3.1	Neutron powder diffraction	35
3.3.2	Elastic TAS measurements at the IN12	36
3.4	Properties of $\text{Pr}_{0.5}\text{Ca}_{1.5}\text{MnO}_4$	42
3.4.1	Basic Properties	43
3.4.2	High temperature structure	47
3.4.3	Charge and Orbital ordered Phase	51
3.5	Conclusions	56
4	Structural aspects of layered Ruthenates	61
4.1	Transitions in $\text{Ca}_{2-x}\text{Sr}_x\text{RuO}_4$	62
4.1.1	Sample Preparation	62
4.1.2	L-Pbca to S-Pbca Transition	64
4.1.3	Rotational Distortion	68
4.1.4	Phase Diagram	71
4.2	Magnetic structure of $\text{Ca}_3\text{Ru}_2\text{O}_7$	73
5	Clip	81
5.1	Program Description	82
5.2	Future developments	91
5.3	Summary	93

6 Powder Diffractometers	95
6.1 Cryostat Control	95
6.1.1 Front Panel	101
6.2 Temperature Sweeps	103
6.3 Calibration Tools	105
A TasFit	111
B Prepared samples	117
List of Figures	121
Bibliography	123
Abstract	135
Kurzzusammenfassung	137
List of Publications	139
Danksagung	141

1 Introduction

The question of what constitutes matter has been a subject perhaps since the days of Leukippos und Demokrit. They postulated that matter consists of " $\alpha\text{-}\tau\epsilon\mu\nu\omega$ " and indeed their atoms were discovered in the 19th and 20th century.

Answering that question that matter is made of atoms is clearly not exhaustive. Graphite and diamond differ greatly in their characteristics and their prices despite both are solely made from carbon atoms. Only the different structure determines their physical properties. Thus the knowledge of the structure is one key ingredient to the understanding of a material. Therefore the question could be: Where are the atoms.¹ In my thesis I will present results of the structural properties of two families of transition metal oxides and I'll try to find an answer to this question.

Transition-metal oxides are a class of materials showing spin, charge, orbital and structural degrees of freedom which may under certain circumstances lead to an ordered phase. Their ground state depends delicately on the different energy scales and small perturbations could introduce large changes in the properties. Strong electronic correlations are present, i. e. their electrons could not be described as a free electron gas like in simple metals nor as being completely localized like in a pure ionic insulator but are somewhat in between. This often leads to complex phase diagrams. From these diagrams interesting new phenomena emerge one prominent example may be the high temperature superconductivity of the cuprates.

The transition metal oxides investigated in this thesis are layered manganites and ruthenates. Manganites are well known for the colossal change of the resistivity at the presence of a magnetic field. This effect, known as CMR effect, occurs in the vicinity of a phase boundary between an antiferromagnetic insulating phase and a ferromagnetic metallic one. The balance between these two phases is such delicate, that the small energy of the magnetic field is sufficient to switch between these phases and introduce a change of the resistivity of several orders of magnitude. Moreover the antiferromagnetic insulating phase exhibits a very fascinating structural property. From resistivity curves a charge ordering transition is clearly established in this phase. Diffraction studies could observe the superstructure peaks associated with it but reveal additional superstructure peaks pointing to a complex structural phase. Two models have been proposed for this phase. Firstly, the so called Goodenough model and secondly the Zener-Polaron model. To decide which model is correct is difficult but chapter 3 will present investigations that were performed to answer this question.

¹and of course, what do they do.

The interest in the layered ruthenates was triggered by the discovery of superconductivity in Sr_2RuO_4 . Up to now, it is the only superconductor that is isostructural to the cuprates but does not contain copper. The inclusion of calcium for strontium leads to a very rich phase diagram, despite the substitution is isovalent. The system $\text{Ca}_{2-x}\text{Sr}_x\text{RuO}_4$ shows a large number of interesting phenomena beyond the superconductivity, like magnetic instabilities, metamagnetic transitions or the Mott-state of Ca_2RuO_4 . The investigations on the phase-diagram of this system and also on the magnetic and nuclear structure of $\text{Ca}_3\text{Ru}_2\text{O}_7$ are presented in chapter 4.

In addition to the scientific work several computer programs have been designed and implemented. Chapter 5 introduces CLIP, a program for the semi-automatically indexing of Laue-photographs. This is used for the routine work of quite a lot of people in the institute since three years. Recently it was released as free software to the public and gained some external users until now. Finally chapter 6 presents changes done on the control program for the powder diffractometers with a special focus to the one used for cryostat operations.

2 Fundamentals

Diffraction is certainly the standard tool for structure determination since the first Laue photograph of Friedrich, Knipping and von Laue [1]. As long as one could neglect effects like absorption, extinction effects, defects and inelastic scattering the most elegant formulation, from which all the basic equations could be derived, is expressing the scattered intensity as the Fourier transform of some scattering density.

$$F(\mathbf{k}) = \int_V \rho(\mathbf{r}) e^{i\mathbf{k}\cdot\mathbf{r}} d\mathbf{r}$$

This formula describes the process, where a plane wave with wave-vector \mathbf{k}_i hits the sample and secondary spherical waves are emitted from every point, whose amplitude depends on the scattering power at its origin. All these secondary waves interfere with each other and possibly build up an outgoing wave with wave-vector \mathbf{k}_f . The structure factor F , which is only dependent on the scattering vector $\mathbf{k} = \mathbf{k}_f - \mathbf{k}_i$, describes the amplitude of the outgoing wave.

All laws which are known from the textbooks could be derived just from the fundamental properties of the Fourier transform. For instance, the a periodic scattering density leads to a discrete grid of scattering vectors where the form-factor does not vanish, the well known reciprocal lattice. This is in turn an equivalent formulation of the Laue equation $\mathbf{k} = \mathbf{G}$ from which the Bragg equation could be derived.

$$\lambda = 2 \cdot d \sin(\theta)$$

Also the conventional form factor equations, with atom form factors and phase factors could easily be derived. Depending on the type of the probe, different scattering densities have to be considered and different results could be obtained. X-rays interact with the electron density, which is rather extended, a fact that under the Fourier transform gives a decrease of the form factor at large scattering vectors. Additionally, heavy atoms with many electrons contribute more to the result than light ions like oxygen or the extreme case of hydrogen, where the precision is reduced.

Electrons also interact with the charge density and with the potential of the core nucleus. They exhibit a much increased cross-section, therefore multiple scattering is the dominant process and the above formalism does only hold partially. Electron scattering could be employed to analyze the reciprocal lattice, e. g. weak superstructure reflections from very small single-crystals or even single crystalline

grains of a powder sample in order to determine the symmetry and space group, whereas the intensities are much harder to model.

Neutrons interact with two different scattering densities. On the one hand, they sense the nuclear core potential, that compared to the wavelength, has a very small extension and thus yields an only weak dependency on the scattering vector under the Fourier transform. Thus even high-indexed reflections show a finite intensity. Also the cross section does not depend on the atomic number, but varies strongly between different elements and even isotopes. Especially the important hydrogen and oxygen atoms show a fair contribution, which increases the precision with which the position and thermal parameters could be determined, or in the case of hydrogen even allows the determination at all. On the other hand, the neutron possesses a magnetic dipole moment and may therefore interact with the magnetization density. This is carried by the valence electrons, and therefore the decrease of the form-factor at large scattering vectors due to the extension shows up here.

The rest of this section will outline only some special details of the experimental methods used in this thesis. The fundamentals of the structure determination by scattering methods could be found in many excellent textbooks on this topic, e. g. [2]. A very good description of the Bruker Apex single-crystal diffractometer and instructions how to use it is given by M. Cwik and W.-D. Stein in their PhD-theses [3, 4]. The powder diffractometers are described in the diploma-theses of M. Cramm, D. Senff, P. Steffens or M. Haider [5–8].

2.1 Temperature depended Powder Diffractometry

One problem which was addressed during the work was the compatibility between high- and low-temperature lattice constants measurements. These frequently could not be interpolated to a consistent room temperature value but instead show a jump at that point, see figure 2.2. There might be numerous reasons for this effect, like a large sample displacement or an inappropriate theta zero point of the high-temperature device, possible deviations in the vertical sample position between both temperature devices or different instrumental resolutions. As different tests did not yield a better result, an internal standard was employed which does not solve the principal problem but its implications.

Silicon was chosen for this purpose because of various reasons. It is relatively cheap, easily available and shows only few, very sharp peaks which minimizes the possible overlap with sample peaks. Furthermore the thermal expansion is rather small, no temperature-driven phase transitions is present and no fluorescence, which would contribute to the background, is observed for common anode materials. As silicon is the basis material of the semiconductor industry, it is one of the best characterized materials available. Extremely pure, large single-crystals are commercially grown, which results in the availability of high purity powder with defined properties even in the long term. That is an important fact for the

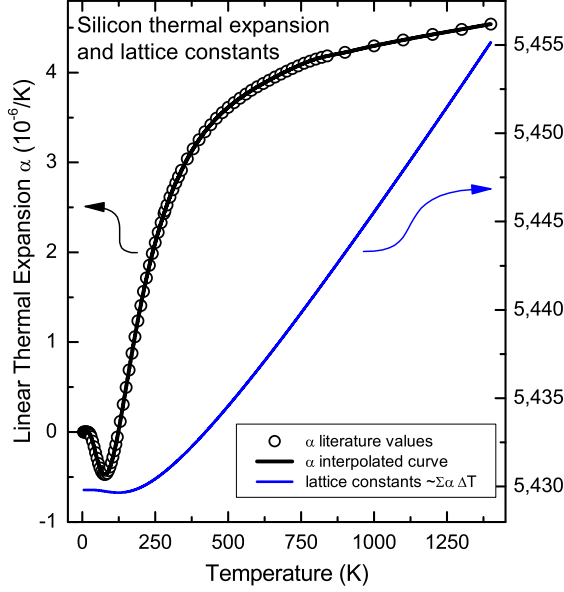


Figure 2.1: Interpolated lattice constants of silicon. The dots indicate literature data from [9–12], the black line the interpolation to these data. The blue line denotes the silicon lattice constants derived by integration of α and scaling to the value suggested for SRM640c by NIST [13].

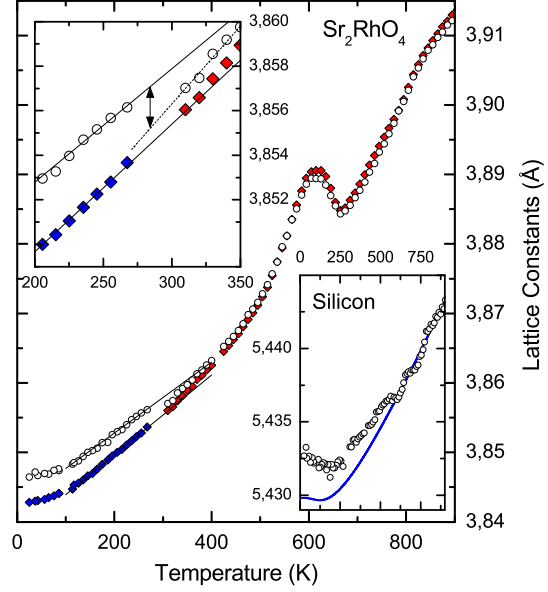


Figure 2.2: Lattice constants of Sr_2RhO_4 from [14]. Results of two fits with the silicon lattice constant either left free running or fixed to the value corresponding to the actual temperature, respectively. Solid points denote the fit with fixed Si lattice constant.

application as an internal standard, as impurities might have an effect on the lattice constants. These facts might have persuaded the American National Institute of Standards and Technology to use silicon as a Standard Reference Material (SRM 640c) [13] for the line position of diffraction patterns vis. as standard for lattice constants measurements. The NIST certificate for SRM 640c also states the precisely determined lattice constants at 22.5 °C. For its application in temperature dependent measurements, the thermal expansion data in a wide temperature range was extracted from a series of papers [9–12], which did not provide the lattice constants but only the linear thermal expansion $\alpha = \frac{1}{L_0} \frac{\partial L}{\partial T}$.

The whole dataset was interpolated in Matlab with an Akima spline function at intervals of 0.1 K from 5 K to 1400 K. This data was then numerically integrated with the simple trapezoidal rule and scaled to get the certified NIST lattice constant $a_0 = 5.4311946(92) \text{ \AA}$ at 22.5 °C.

$$a(T) = a_{\text{Nist}} \left(\int_{22.5^\circ\text{C}}^T \alpha(T) dT + 1 \right)$$

This procedure then yield a compilation of silicon lattice constants at intervals of 0.1 K as shown in figure 2.1.

Measurement The sample is grounded with about the same volume fraction of silicon powder and otherwise handled as usual. The silicon might not only serve as an internal standard but could be used to determine or adjust the sample displacement from the center of the diffractometer because of the known position of the Si $\{111\}$ reflection at 28.4° with Cu K_α radiation.

In the subsequent refinement of the diffractograms with FULLPROF [15], for each temperature step the temperature is read from the datafile and the corresponding lattice constant is looked up from the compilation. This is then used as the lattice constant of the silicon phase and held constant during the refinement.

Figure 2.2 shows the result, compared with a second refinement, where the silicon lattice constant was allowed to run freely. Blue and red symbols represent the data from the cryostat and HTK measurements with fixed silicon lattice constants, respectively. The open symbols represent refinements to the same data with a running silicon lattice constant. In the upper inset, the transition from cryostat to HTK is shown, together with linear fits to the low temperature data. Obviously the extrapolation from low temperatures to the high-temperature data works much better with the fixed lattice constants. In fact, the two refinements matches quite good at high temperatures and starts to deviate from each other when the temperature is lowered. This effect could also be observed from the silicon lattice constant. In the lower panel the integrated thermal expansion data and the refined lattice constants are shown. Also here the high-temperature data matches quite well, while the low temperature data are off by about 0.4 %.

2.2 Single Crystal Diffraction

Single-crystal diffraction experiments have been carried out on the Bruker X8 Apex x-ray diffractometer in the institute and at the neutron diffractometers HeiDi (FRM II, Munich) and 5C.2 (LLB, Paris). The data both in the x-ray case and for most neutron measurements has been treated with JANA2000 [16] or FULLPROF [15] in the case of magnetic structures.

X-Ray Diffraction with Bruker X8 Apex The X8- Apex is a single-crystal diffractometer equipped with a kappa goniometer and a large, untapered CCD area detector. A sealed x-ray tube with a molybdenum anode and a graphite (002) monochromator is employed as radiant source. A measurement consists of a series of runs. In each run the sample is rotated around either the ω or the ϕ axis with otherwise fixed settings. Frames are taken during the rotation of the axis in intervals of 0.5° . Normally, two frames are taken in the same interval and correlated in order to suppress spurious events like cosmic radiation. Typical exposure times per frame were in the range of 5 s to 150 s and are controlled by a dedicated timing shutter.

Details of the sample preparation and data handling / reduction could be found in the PhD-theses of M. Cwik and W.-D. Stein [3, 4]. Two enhancements were

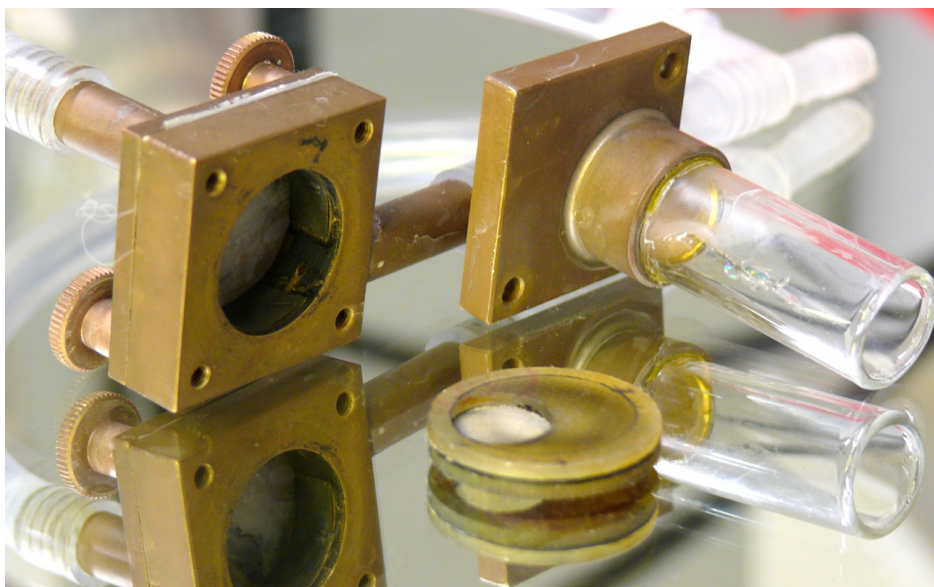


Figure 2.3: Image of the extraction ball mill. On the left side the mill body with its two air inlets is shown. In the background the T piece with the tapping for the extraction air stream connected to the back of the mill is visible. The ball mill cover with the glass extraction cylinder is on the right, the filter disc with a 100 μm wire mesh on the front.

introduced in the course of this thesis. First the air-drier K-MT 5 for the Kryoflex cryostat was replaced with a much larger and more powerful model BS-P 35, both from Zander Aufbereitungstechnik GmbH. This solved the problem of ice formation at the cryostat nozzle and the crystal. Measurements down to 120 K could be carried out routinely without posing any difficulties, below 120 K down to 90 K sometimes ice formation is still observed.

The second enhancement concerns the ball mill, which is used to prepare the single-crystal spheres. The original device of Bond [17] is very successful in producing small spheres, but the sphere sizes are not reproducible and one has to carefully choose the milling time and air pressure in order to not completely mill the valuable sample to powder. In this design, the exhaust is covered by a very fine sieve through which only the dust could escape. Several ball mills of that type were used at the institute, but the mentioned problems led finally to the adaption of a design of Cordero-Borboa [18]. Here, a first coarser sieve with a mesh size comparable to the desired sphere diameter allows pieces smaller than the mesh size to leave the mill. These are caught in a storage cylinder and prevented from escaping by a second fine sieve. Several samples of stainless steel gauzes with different mesh sizes were kindly provided by Haver & Boecker Drahtweberei and the mentioned bakelite disc has been replaced by a piece of glass fiber reinforced plastic, a piece of a printed circuit board provided by the electronic tool shop. This grinder (see figure 2.3) now allows to reproducibly create spheres of 100 μm diameter without the need to constantly supervising the grinding process and without the risk of losing the valuable sample.

	3×3	5×5	5×10	10×10 _d
3×3	•	$(h-k, h+k, l)$	$(h-k, 2\cdot(h+k), l)$	$(2(h-k), 2(h+k), 2l)$
5×5	$(\frac{h+k}{2}, \frac{-h+k}{2}, l)$	•	$(h \ 2k \ l)$	$(2h \ 2k \ 2l)$
5×10	$(\frac{h}{2} + \frac{k}{4}, -\frac{h}{2} + \frac{k}{4}, l)$	$(h \ \frac{k}{2} \ l)$	•	$(2h \ k \ 2l)$
10×10 _d	$(\frac{h+k}{4}, \frac{-h+k}{4}, \frac{l}{2})$	$(\frac{h}{2} \ \frac{k}{2} \ \frac{l}{2})$	$(\frac{h}{2} \ k \ \frac{l}{2})$	•

Table 2.1: Formulas for the conversion of reciprocal indices between different cells. The cell from where to convert is on the left, the cell to where to go on the top.

2.3 Data Integration of HeiDi Measurements

HeiDi is the single-crystal diffractometer at the hot source of the Forschungsneutronenquelle Heinz Maier-Leibnitz (FRM II), München. It features the choice of three different monochromators, Cu-(2 2 0), Cu-(4 2 0) and Ge-(3 1 1) and three fixed scattering angles $2\theta=20^\circ, 40^\circ$ and 50° , giving a total of nine different available wavelengths. The $\lambda/2$ contamination could be reduced by a suitable filter. In the case of the Ge-(3 1 1) monochromator, it is not present at all, as the second order reflection (6 2 2) is systematically extinct in its space group $Fd\bar{3}m$. For the measurements presented in this thesis, the employed wavelength was 0.873 \AA , generated by the Cu-(2 2 0) monochromator at a diffraction angle of $2\theta=40^\circ$. At this wavelength, a $500 \mu\text{m}$ erbium filter reduces the $\lambda/2$ -radiation to 1.13% of the fundamental one [19, 20].

The sample is positioned by an acentric Euler cradle, which could host a closed cycle cryostat or a furnace for temperature work between 2.5 K to 1000 K. A ^3He proportional tube acts as a point detector. The diffractometer is controlled by a modified version of the dif4 program [21].

2.4 Cell choices for Manganite Structures

In the description of order phenomena in single-layered manganites, different cell choices have been introduced in the literature and will be used in this thesis. This section will present the different cells, the procedure to translate between the cells and especially their nomenclature in the thesis.

The basic cell is that of the ideal layered perovskite structure. Its cell constants are in the order of $3.86 \text{ \AA} \times 3.86 \text{ \AA} \times 12.4 \text{ \AA}$. This is the cell of the prototype structure K_2NiF_4 with the symmetry $I4/mmm$. $\text{La}_{1-x}\text{Sr}_{1+x}\text{MnO}_4$ possesses this symmetry at room temperature, $\text{Pr}_{1-x}\text{Ca}_{1+x}\text{MnO}_4$ presumably above 466 K. This cell will be called the *tetragonal cell* or 3×3 cell in this thesis and is used if not otherwise stated. Reciprocal space vectors will be labelled with a “t”, if necessary, e.g. $(0.75 \ 0.25 \ 0)_t$.

The next cell is derived by a rotation around the **c**-axis by 45° . It will be

	3×3	5×5	5×10	$10\times 10_d$
Mn ³⁺ magnetic reflection	$(\frac{3}{4} \frac{1}{4} \frac{1}{2})$	$(1 \frac{1}{2} \frac{1}{2})$	$(11 \frac{1}{2})$	(211)
Mn ⁴⁺ magnetic reflection	$(\frac{1}{2} 0 \frac{1}{2})$	$(\frac{1}{2} \frac{1}{2} \frac{1}{2})$	$(\frac{1}{2} 1 \frac{1}{2})$	(111)
Orbital magnetic reflection	$(\frac{9}{4} \frac{1}{4} 0)$	$(2 \frac{5}{2} 0)$	(250)	(450)
Principal reflection	(200) (110)	(220) (020)	(240) (040)	(440) (040)

Table 2.2: Reflections indices for the different sources of order represented in the different cells.

denoted as *orthorhombic cell* or 5×5 cell with an index “o”. The new lattice constants, expressed by the tetragonal ones are $a_o = a_t - b_t$ and $b_o = a_t + b_t$, their length is roughly $\sqrt{2}$ times the length of the tetragonal lattice constants, $5.46 \text{ \AA} \times 5.46 \text{ \AA} \times 12.4 \text{ \AA}$, but a and b need not to be equal. The symmetry is orthorhombic in this case.

The third cell is derived from the orthorhombic cell by doubling the b -lattice constant. This is the cell for the description of the combined charge and orbital order. Its dimensions are roughly $5.46 \text{ \AA} \times 10.92 \text{ \AA} \times 12.4 \text{ \AA}$ and it will be labeled as 5×10 -cell despite the b lattice constant is closer to 11 \AA .

The magnetic order emerges from the charge and orbital ordered phase but doubles the orthorhombic cell in \mathbf{a} - and \mathbf{c} -direction. For a combined description of charge, orbital and magnetic order, or in order to handle the twinning of the 5×10 -cell it is sometimes desirable to use this rather large cell with dimensions $10.92 \text{ \AA} \times 10.92 \text{ \AA} \times 25.8 \text{ \AA}$. It will be labelled as 10×10 in the cast of a non doubled c lattice constant ($c=12.4 \text{ \AA}$ or $10\times 10_d$ in case of a doubled c lattice constant).

Table 2.1 summarizes the transfer formulas to transfer between different cells. Table 2.2 shows the representations of some important superstructure reflections in the different cells.

3 Crystal and magnetic structure of layered manganites

The interest in the perovskite-type manganite is conducted by two major observations. First the prediction and discovery of a charge- and orbital-ordered phase by Goodenough [22] and Wollan and Koehler [23], respectively and second by the observation of the colossal magnetoresistivity (CR) by von Helmolt *et al.* [24].

For half-doped manganites (i. e. with a formal valence of $\text{Mn}^{3.5+}$) Goodenough predicted a segregation in Mn^{3+} and Mn^{4+} ions, which are ordered in a checker-board fashion. As the Mn^{3+} ions possesses a single electron in the e_g orbital, they offer an additional orbital degree of freedom, which is not present at the Mn^{4+} -sites. Simultaneously to the charge order an orbital order is formed, where the Mn^{3+} - e_g orbitals form a zig-zag arrangement. This phase is called charge- and orbitally-ordered phase (COO-model) or from the thereof emerging magnetic order CE-phase (figure 3.1).

The CMR effect was explained by a switch from an antiferromagnetic, insulating phase as found by Wollan *et al.* to a ferromagnetic metallic phase by an external magnetic field.

Large effort was conducted in order to establish the universality of the ground state order predicted by Goodenough in different manganites, as this is a key ingredient for CMR models: $\text{Pr}_{1-x}\text{Ca}_x\text{MnO}_3$ [25], $\text{Pr}_{1-x}\text{Sr}_x\text{MnO}_3$ [26], $\text{Pr}_{0.5}\text{Ca}_x\text{Sr}_{0.5-x}\text{MnO}_3$ [27, 28], $\text{La}_{1-x}\text{Ca}_x\text{MnO}_3$ [29–31], $\text{Tb}_{0.5}\text{Ca}_{0.5}\text{MnO}_3$ [32], $\text{Nd}_{0.5}\text{Ca}_{0.5}\text{MnO}_3$ [33] and $\text{Nd}_{1-x}\text{Sr}_x\text{MnO}_3$ [26, 34].

In 2002, Daoud-Aladine *et al.* [35] proposed a new symmetry of the charge-ordered ground state based on the crystal structure refinement of $\text{Pr}_{0.6}\text{Ca}_{0.4}\text{MnO}_3$, where the charges are bond centered, as opposed to the site-centered model of Goodenough. This so-called Zener-Polaron model was additionally supported by Hartree-Fock calculations [36]. Resonant x-ray scattering [37] and an alternative neutron diffraction experiment [38] on the other hand favor a conventional site-centered scenario for this composition, however there is no statistical evidence in the neutron powder diffraction data powder for the preference of one model. Thus the experiments are subject of controversial discussion, at least those concerning the praseodymium-calcium 113 compound.

One drawback of all of these structure determinations is the use of pseudo-cubic manganites. As the phrase "pseudo" suggests, their real structure deviates from a cubic one, but the discrepancy are rather small. They emerge from the ideal cubic perovskite structure by rotations of their MnO_6 octahedra already in the non-charge-ordered phase and show mostly rhombohedral or orthorhombic

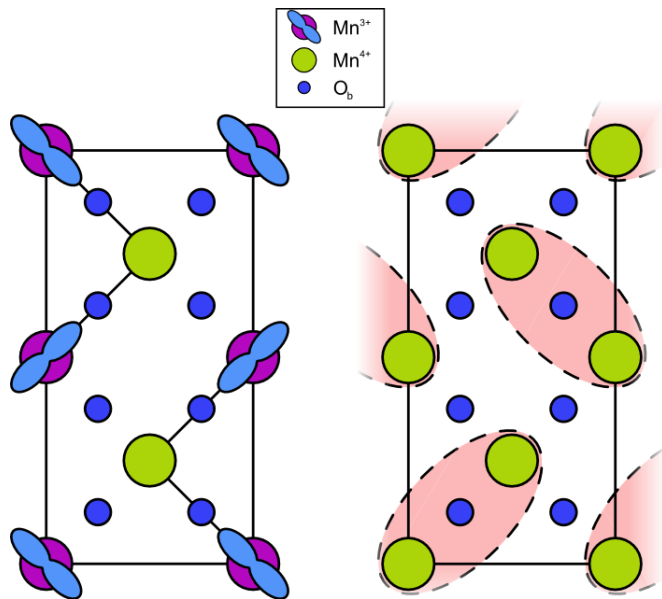


Figure 3.1: Sketch of the COO and Zener-Polaron model. Shown is one MnO₂ layer. In the COO-model shown on the left, charges order in a checkerboard arrangement of Mn³⁺ and Mn⁴⁺ ions. Mn³⁺ ions possess a single electron in the e_g orbital which orders in the indicated zig-zag chains. In the Zener-Polaron picture on the right, one excess electron is shared between two Mn-ions, leading to the formation of dimers which arrange in zig-zag chains as well.

symmetries. As the deviation from the cubicity is mostly small, they are prone to twinning and because of the three dimensional structure, a large number of twin domains, i. e. up to twelve different orientations could appear. The twinning severely complicates an exact structure determination.

One alternative is the usage of layered structures. Especially La_{0.5}Sr_{1.5}MnO₄ is a very promising material. First of all, it is possible to grow large single-crystals, which is the basis for single-crystal diffraction but additionally allows to perform inelastic neutron scattering. At high temperatures the compound possesses the K₂NiF₄ structure, space group *I4/mmm*, where the MnO₆ octahedra are not rotated and no twinning is present. At 225 K a rise in the resistivity is observed, which correlates with a structural transition. In this phase, the crystal shows charge order and consists at most of two twin domains, as the underlying structure itself is untwinned. Thus investigations do not suffer from the heavy twinning as in the case of the perovskite manganites which increases the chances of more significant results.

Two series of layered manganites were synthesized in the course of this thesis. This work is presented in section 3.1. Investigations of the crystal and magnetic structure of the La_{0.5}Sr_{1.5}MnO₄ compound are shown in section 3.2 which extend to ruthenium co-doping in section 3.3 and finally, section 3.4 gives the results obtained for the Pr_{0.5}Ca_{1.5}MnO₄ compound.

3.1 Preparation of poly- and single-crystalline samples

Experimental work in condensed-matter physics relies on the availability of suitable samples. Thus the preparation of samples is an important first step for

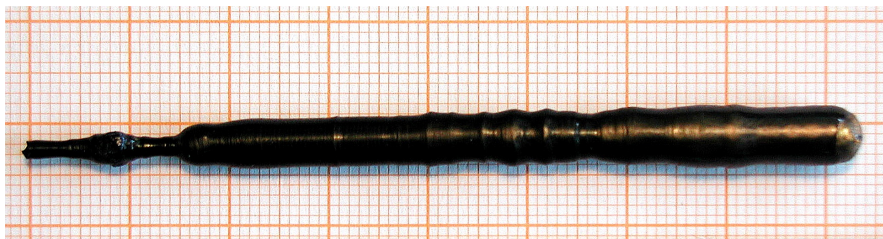


Figure 3.2: Single crystal of $\text{La}_{0.5}\text{Sr}_{1.5}\text{MnO}_4$, OJS35EK6. Growth direction is from left to the right. On the left, the end of the necking process is visible.

successful condense matter research. Especially inelastic neutron scattering is a potent consumer of large single-crystals. Unsurprisingly the authors first contact with single-crystal preparation was due to the demand for a larger single-crystal for an inelastic neutron experiment. In this course, several different manganite samples have been prepared, both poly-crystalline and single-crystalline ones. Appendix B gives the complete list of samples prepared during this thesis. These include samples of $\text{La}_{1-x}\text{Sr}_{1+x}\text{MnO}_4$ with various doping levels, ruthenium co-doped $\text{La}_{1-x}\text{Sr}_{1+x}\text{Ru}_y\text{Mn}_{1-y}\text{O}_4$ and $\text{Pr}_{1-x}\text{Ca}_{1+x}\text{MnO}_4$ but also various $\text{Ca}_{2-x}\text{Sr}_x\text{RuO}_4$ samples.

A comprehensive description on the synthesis, the chemistry and the challenges in preparation of $\text{La}_{1-x}\text{Sr}_{1+x}\text{MnO}_4$ is given in the PhD-thesis of P. Reutler and M. Benomar [39, 40]. It was found that the synthesis conditions presented in these two theses do not only work for the pure lanthanum-strontium series, but also for ruthenium co-doping and even the praseodymium-calcium compounds could be prepared by this procedure. Thus, only the basic steps and variations the procedure will be discussed in the following.

For the preparation of poly-crystalline samples and precursors for single-crystal work, stoichiometric amounts in powder form of MnO_2 , dried La_2O_3 and SrCO_3 for the La-Sr series, Pr_2O_3 ¹ and CaCO_3 for the Pr-Ca series and additionally RuO_2 for the ruthenium co-doping were grounded in an agate mortar with acetone until the latter is fully evaporated and then calcinated at 1000 °C for 24 h under air. The resulting powder was regrounded with acetone, pressed to a rod and fired at 1450 °C for 36 h under air. Only these two heat treatments with intermediate grinding were performed, instead of the up to five steps described by P. Reutler. The faster preparation route and especially the less contamination opportunities were favored over a possible better homogeneity and higher density of the rods. As the preparation of several high-quality crystals was possible even with this shortened reaction path, this judgement is well justified.

Single-crystals of $\text{La}_{1-x}\text{Sr}_{1+x}\text{MnO}_4$ and $\text{La}_{0.5}\text{Sr}_{1.5}\text{Ru}_y\text{Mn}_{1-y}\text{O}_4$ have been grown in collaboration with A. Revcolevschi at the Laboratoire de Physico-Chimie de l'Etat Solide, Université Paris-Sud XI. At this place, two infrared image furnaces are available, a CSI FZ-T-4000-H-II-PP from CRYSTAL SYSTEM INC. and a NEC

¹the preparation is possible as well with Pr_6O_{11}

SC-N15HF from NEC CORPORATION, from which the latter was employed. The NEC furnace consists of two elliptical, gold plated aluminum mirrors which cover a much greater solid angle than the four mirrors in the CSI furnace. These mirrors focus the radiation of the two 1500 W halogen lamps onto the crystal. The crystal itself is located in the inside of a silica tube, which allows the use of a process gas, like oxygen or argon with pressures up to 10 bar and at the same time protects the mirror from evaporated material.²

Two crucial points have been identified for a successfully growing of single-crystal manganites.

- When the feed and seed rod are initially brought together and the melting zone is formed, a lot of crystallites grow side by side. When the molten zone advances, some of these crystallites grow at the expense of others and finally, to obtain a proper single-crystal, only a single orientation is allowed to survive. For manganite samples crystals with two or more domains which are grown side by side over the entire length of the crystal [41] are frequently observed. To accelerate the selection of only one domain, one has to reduce the diameter of the crystal until only a single domain is present. Then the diameter is increased to the normal value. This necking technique was employed during the growth experiments in the NEC furnace and a reduction down to only 1 mm diameter was possible.
- The second point regards the identification of the existence of only a single domain. Fortunately the layered manganites form cracks between the different domains, that are observable during the growth. If no such cracks could be observed any more, chances for a single domain crystal are pretty high. The CSI furnaces at Cologne and Orsay have video cameras for the observation of the growth installed, which allow an additional recording. At the NEC furnace, being a rather old model, an optical telescope is installed instead. The continuous observation of the growth process is at best exhausting and no quick overview is possible, but the image quality is far better than that on the camera equipped models³. It is the believe of the thesis author, that the good image quality of the telescope is definitely an improvement and a great help in observing the cracks associated with the different domains.

Figure 3.3 shows a sketch of the necking process. In a first step, the pulling

²The NEC furnace is said, to have a better defined focus zone. One observation made during the experiments supports this claim. In the Cologne CSI image furnace, model FZ-T-10000-H-VI-VP rods with 8 mm diameter were regularly used without problems and thus prepared in advance to the stay in Paris. Here, they did not melt satisfyingly in the NEC furnace. At rather high power the solid interior cones of feed and seed rod occasionally touch, while increasing the power leads to a low viscosity melting zone, which easily drops off. A shift to 6 mm diameter rods, which are usually employed at the NEC furnace solves this problem.

³The video system at the CSI-models uses NTSC television technique with a resolution of only 544×480 pixel, which is the origin of the low image quality.

speed of the lower shaft is increased. As now the feed rod does not supply new material to the zone at the same rate as is withdrawn by the crystal, its diameter is reduced. The adjustment of the crystal diameter by the relative speed of upper and lower shaft is favorable over a manual raising and lowering of the shafts, as this abrupt motion may lead to a break of the molten zone. If the diameter is at its desired size, the pulling speed of the lower is adjusted to maintain it. During this phase, the zone is extremely fragile, thus the growth as to be monitored and all parameters have to be adjusted continuously.

The different thermal expansion between different domain leads to cracks at the domain boundaries. If one of the domains grows at the cost of another one, a pair of these cracks move into each other and finally joins when the domain is fully eliminated. This allows to monitor the number of domains that are still present. If the last pair of cracks has joined, eventually only a single domain is left and the diameter of the crystal is increased to its nominal value by adjustment of the pulling speed of the upper and lower shaft.

Other growth parameters used in the synthesis of the $\text{La}_{1-x}\text{Sr}_{1+x}\text{MnO}_4$ samples were an oxygen atmosphere with a pressure of 2.5 bar, a growth speed of 6 mm/h and a relative rotation of 25 turns per minute between upper and lower shaft.

Figure 3.2 shows a resulting single-crystal of $\text{La}_{0.5}\text{Sr}_{1.5}\text{MnO}_4$. It is about 65 mm long and has a diameter of 5 mm. The smallest diameter is only 1.7 mm. It is a typical representative for the $\text{La}_{1-x}\text{Sr}_{1+x}\text{MnO}_4$ manganites grown at the LPCES. After a growth run of the non-ruthenium doped samples, the silica tube showed very light contaminations with a brownish film. This is presumable evaporated material from the feed and seed rod and consists of pyrolusite (MnO_2).

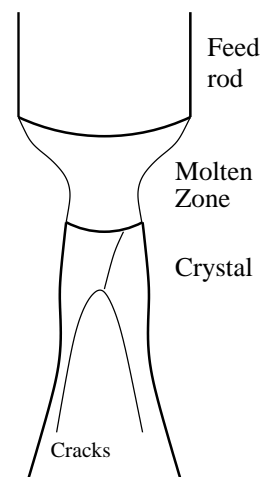


Figure 3.3: Single crystal growth with necking technique.

Preparation of Ruthenium co-doped samples Ruthenium co-doped samples of $\text{La}_{1-x}\text{Sr}_{1+x}\text{Ru}_y\text{Mn}_{1-y}\text{O}_4$ have been prepared by stoichiometric substitution of manganese by ruthenium, eg. no excess RuO_4 has been added to account for extended ruthenium evaporation. With increased ruthenium content, the brownish contamination inside the silica tube gets darker and finally turns into a black and generally increases in magnitude. This indicates the stronger evaporation on ruthenium during the growth. The crystals are also much more fragile and with increasing ruthenium content are prone to cleavage along the ab -plane. Above $y=10\%$ they spontaneously degrade to thin disk-like crystals.

The preparation of powder samples of $\text{La}_1\text{Sr}_1\text{MnO}_4$ was carried out as outlined above. The single-crystal growth attempt was hampered by the high lanthanum content which resulted in the precursors being highly hygroscopic. Rods which were pressed and fired swell to about double the size during the night to a loose agglomerate which immediately decays upon contact. A direct transfer from the

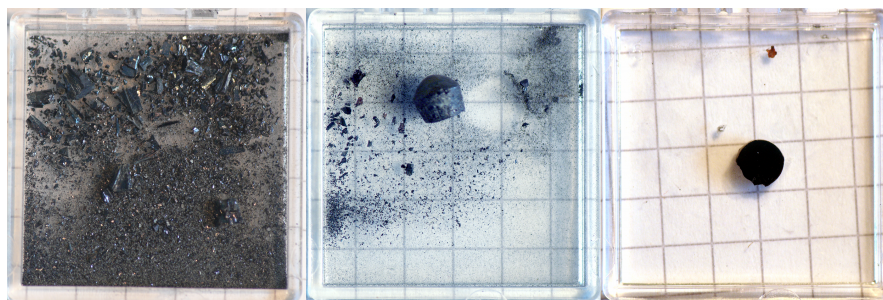


Figure 3.4: Decomposition of $\text{Pr}_{0.5}\text{Ca}_{1.5}\text{MnO}_4$ crystals. On the left, one piece of the crystal grown by A. Agung Nugroho and stored for 18 month under ambient conditions is shown, it completely disaggregated into powder and fine splinter. In the middle, the end-piece of a crystal stored twelve month under natural conditions is displayed, here first signs of decomposition are visible. On the right, a piece of the same crystal stored in a glove box with an argon atmosphere is shown. No indication of disaggregation is observable.

prereaction furnace into the image furnace did not yield satisfying results as well. Here the rod splinters as soon as it reaches the focus, most probable due to the explosively evaporation of water remains. Because of this, only two single-crystalline samples could be grown from very thoroughly dried rods.

Preparation of praseodymium-calcium manganites Poly-crystalline samples of $\text{Pr}_{1-x}\text{Ca}_{1+x}\text{MnO}_4$ have been prepared for $x=0.5$, $x=0.66$ and $x=0.75$ with almost the same procedure as described above. Appropriate amounts of praseodymium oxide (both Pr_2O_3 and Pr_6O_{11} were used and give equal results), calcium carbonate and manganese dioxide were mixed in an agate mortar, calcinated at 1000°C , finally sintered at 1400°C for 50 h in air. Single-crystals of $\text{Pr}_{0.5}\text{Ca}_{1.5}\text{MnO}_4$ have been grown in the Cologne CSI image furnace with 4×1000 W lamps, oxygen atmosphere with a pressure of 3 bar and a flow of $0.8 \text{ l}/\text{min}$, $3 \text{ mm}/\text{h}$ growth speed. The rods for single-crystal growth were made from fully reacted powder and sintered for 12 h in air. Powder diffraction of a crushed piece of the single-crystal shows no indication of impurity phases and gives the lattice constants $a=5.3736(11) \text{ \AA}$, $b=5.4077 \text{ \AA}$ and $c=11.8271(27) \text{ \AA}$. In total two good single-crystals could be grown, the first one by Agung A. Nugroho and another one by the thesis author.

The first crystal decomposed after approximately 6 month, which created the need for the second crystal. As the decomposition was suspected to be caused by the contact with humidity, most of the second crystal was stored in a glove box with an argon atmosphere, only the end-part was left in air for reference purposes. This shows at present, one year after the growth, first signs of decomposition while the parts stored in an argon atmosphere do not, see figure 3.4. The long time before decomposition implies that the crystals might be easily handled in air for measurements but should be stored under non-humid conditions in the long term.

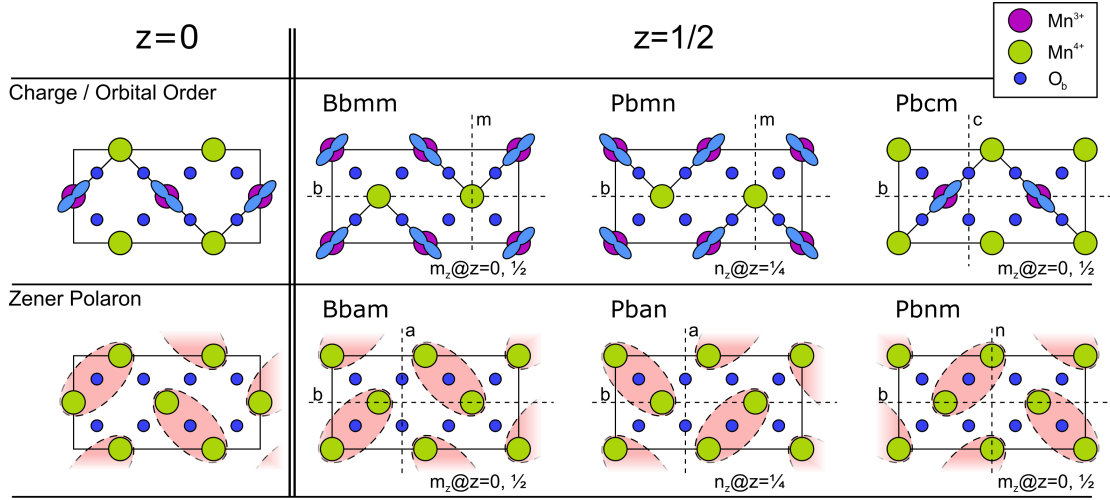


Figure 3.5: Possible space groups for site- and bond-centered charge ordering in half-doped layered manganites. Upper and lower row show the arrangement for site-centered and bond-centered charge ordering, respectively. The leftmost column sketches the MnO_2 layer at $z=0$. For the site-centered charge order, orbital and solid lines indicate the zig-zag arrangement, while the dimers in the bond-centered charge order are emphasized by red ellipses. The next columns show the different arrangements for the $z=1/2$ layer, i. e. the coupling in the c -direction, each with the three generating symmetry elements and the corresponding space group. For both, site- and bond-centered charge order, a fourth arrangement exists, which is equivalent to the rightmost column and omitted here.

3.2 Crystal structure of charge-ordered $\text{La}_{0.5}\text{Sr}_{1.5}\text{MnO}_4$

As discussed in the introduction, two models for the charge order are proposed for the manganites. A site-centered one, having a charge disproportion to Mn^{3+} and Mn^{4+} sites and a thereupon based order of the Mn^{3+} t_{2g} orbital (COO-model or sometimes CE-model) and a bond-centered one, leading to Mn-Mn dimers (Zener-Polaron-model). For $\text{La}_{0.5}\text{Sr}_{1.5}\text{MnO}_4$ both models lead to an orthorhombic space group with lattice constants $\sqrt{2}\mathbf{a} \times 2\sqrt{2}\mathbf{a} \times c$ in terms of the $I4/mmm$ cell, the 5×10 -cell, see section 2.4. Figure 3.5 shows the six possible space groups for a planar arrangement, i. e. no out-of plane component for the manganese and the basal oxygen ions is present. The B-centered space groups $Bbmm$ and $Bbam$ show the optimal stacking of zig-zag elements and dimers, respectively, as in these structures the those elements show no crossing in adjacent layers.

An indirect proof for the site-centered charge ordering in $\text{La}_{0.5}\text{Sr}_{1.5}\text{MnO}_4$ is given by Senff *et al.* [42]. Here, the magnon dispersion is measured by inelastic neutron scattering and fitted to theoretical models for the COO and Zener polaron model. The slope of the dispersion in different directions allows them to rule out the Zener polaron model.

	$R_{w,all}$	GoF_{all}	N_{all}	$N_{>3\sigma}$	$\Delta I > 25\sigma$
<i>Bbmm</i>	4.56	4.52	830	551	16
<i>Pbmn</i>	8.20	8.52	758	508	154
<i>Pbcm</i>	9.70	6.26	746	434	177
<i>Bbam</i>	4.64	4.60	829	550	17
<i>Pban</i>	6.61	6.62	815	521	35
<i>Pbnm</i>	4.83	4.76	845	551	23

Table 3.1: Results of the D10 neutron data refinement to the six possible space groups. The top three space groups correspond to a site-centered charge ordering, while the bottom three space groups correspond to a bond-centered charge ordering. $R_{w,all}$ and GoF_{all} have been calculated by JANA2000, the number of reflections N_{all} and $N_{>3\sigma}$ are the merged ones which were compatible with the respective space group. The last column states the number of reflections, where $(I_{obs} - I_{calc}) > 25\sigma$ which have been omitted from the refinement.

3.2.1 Charge and Orbital ordering

Nevertheless, a direct observation of the realized model was highly desirable. Thus a detailed neutron single-crystal diffraction experiment was carried out at the D10 diffractometer at the ILL research reactor.⁴ The crystal was cooled to 130 K, well in the charge ordered phase, but above the Néel temperature, in order to avoid complications by magnetic contributions to the scattered intensities. The 2D-detector of the D10 diffractometer allows an accurate determination of the background and discrimination of possible contaminations from the sample environment like powder lines from cryostat shields.

All six stacking patterns for both charge order scenarios were fitted to the data with the JANA2000 program. The reflection data was averaged according to the space group by the input routine of JANA2000. All refinements were based on F^2 , performed in the 5×10 cell and twinning was taken into account. Reflections having $(I_{obs} - I_{calc}) > 25\sigma$ were automatically omitted from the refinement. Table 3.1 gives the results.

A quick look on these results immediately show, that only the B-centered space groups *Bbmm* and *Bbam*, i. e. those, where the main structure elements show no crossing in adjacent layers, are probable candidates. In both cases, there is still a significant number of reflections exhibiting strong deviations between calculated and observed intensities, but these effects arise from an insufficient extinction correction. The two further COO-groups *Pbmn* and *Pbcm* could not describe a rather large number of reflections and their agreement factors are definitively out of reach for a satisfying solution. For the Zener-Polaron, the picture is a bit less clear, but nevertheless *Pban* and *Pbnm* show less agreement than *Bbam* does.

A thorough investigation of the two remaining space groups was then performed

⁴The experiment was performed by M. Braden, P. Reutler, O. Friedt and M. Fernandez-Diaz.

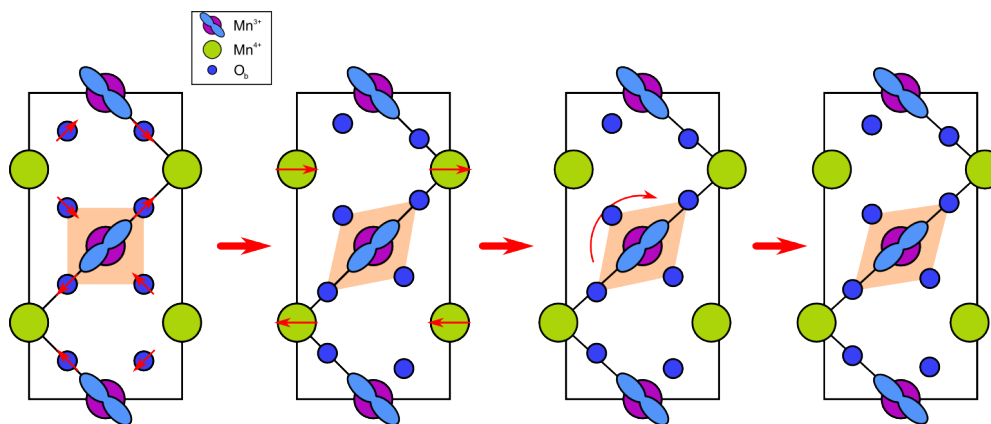


Figure 3.6: Sketch of the distortions appearing at the charge and orbital ordering transition.

with the PROMETHEUS [43] program package. Because things like multiple scattering, not perfectly corrected extinction and absorption or other systematic errors tend to get compensated by the thermal parameters, these were strongly restricted. In the case of the site-centered charge ordering model, the thermal ellipsoids for both manganese ions, both lanthanum/strontium positions, both apical and both basal oxygen ions, respectively were chosen identical as were the U_{11} and U_{22} parameters for each of the four different ellipsoids. This leaves only 9 thermal parameters to be varied as in space group $I4/mmm$, instead of 26^5 . Similar restrictions were introduced for the $Bbam$ refinement. Additionally a refinement in the $Bb2_1m$ space group was performed, a common sub-group of $Bbmm$ and $Bbam$ where both models could be described simultaneously.

The agreement factors of these refinements are:

	Site-centered	Bond-centered	$Bb2_1m$
R_w , including all reflections	5.243 %	6.038 %	5.224 %
R_w , only unrejected reflections	4.188 %	5.279 %	4.129 %
weighted Goodness of Fit	7.04 %	11.17 %	6.87 %

Despite the larger degrees of freedom, the refinement in the $Bb2_1m$ space group does not yield a significantly enhanced result, while the refinement in the $Bbam$ space group is definitively worse. Thus one may conclude, that at 130 K, the site-centered charge ordering with accompanying orbital order of the t_{2g} orbital is realized in $\text{La}_{0.5}\text{Sr}_{1.5}\text{MnO}_4$.

Figure 3.6 sketches the distortions appearing at this transition. First, the Mn^{3+} t_{2g} orbital order and the thereby distorted charge density leads to an increase of the manganese-oxygen bond length in direction of the orbital and to a decrease

⁵The by symmetry allowed position parameters plus the three diagonal elements of the thermal displacement tensor per site plus the U_{12} for the basal oxygen ions. A maximum of 31 parameters is allowed in the $Bbmm$ symmetry.

Space Group	<i>Bbmm</i>			
<i>a</i>	(Å)	5.452		
<i>b</i>	(Å)	10.904		
<i>c</i>	(Å)	12.408		
Rot(O_b1)	(deg)	0.69(3)		
Rot(O_b2)	(deg)	0.75(3)		
<hr/>				
Mn(1)	(0,0,0)		La/Sr(1)	(0,0,z)
	BVS	3.497(4)		<i>z</i>
	$U_{11}=U_{22}$	0.0015(3)		$U_{11}=U_{22}$
	U_{33}	-0.0004(4)		U_{33}
Mn(2)	(x,1/4,0)		La/Sr(2)	(x,1/4,z)
	<i>x</i>	0.50598(8)		<i>x</i>
	$\Delta(1/2, 1/4, 0)$	0.033(1) Å		<i>z</i>
	BVS	3.717(6)		$\Delta(1/2, 1/4, z)$
	$U_{ii} = \text{Mn(1)} U_{ii}$			$U_{ii} = \text{La/Sr(1)} U_{ii}$
O _{basal} (1)	(x, y, 0)		O _{apex} (1)	(0,0,z)
	<i>x</i>	0.2611(1)		<i>z</i>
	<i>y</i>	0.12748(6)		$U_{11}=U_{22}$
	$\Delta(1/4, 1/8, 0)$	0.0664(6) Å		U_{33}
	$U_{11}=U_{22}$	0.0051(2)	O _{apex} (2)	(x,1/4,z)
	U_{33}	0.0031(2)		<i>x</i>
	U_{12}	0.0005(2)		<i>z</i>
O _{basal} (2)	(x, y, 0)			$\Delta(1/2, 1/4, z)$
	<i>x</i>	-0.2432(2)		$U_{ii} = \text{O}_{\text{apex}}(1) U_{ii}$
	<i>y</i>	0.1248(1)		
	$\Delta(-1/4, 1/8, 0)$	0.0377(5) Å		
	$U_{ii} = \text{O}_{\text{basal}}(1) U_{ii}$			
	$U_{12} = -\text{O}_{\text{basal}}(1) U_{12}$			

Table 3.2: Results of the crystal structure refinement of the charge and orbitally ordered phase of $\text{La}_{0.5}\text{Sr}_{1.5}\text{MnO}_4$ from neutron diffraction at 130 K.

perpendicular to it. This results in a distortion of the Mn^{4+} -octahedron in a way that the basal plane forms an isosceles trapezoid and eventually leads to a shift of the Mn^{4+} ion along the **a**-direction. The direction of these shifts alternate which cause a small rotation of the Mn^{3+} octahedron around the **c**-axis. Thus, the two inequivalent manganese positions are characterized by two fundamentally different oxygen environments. The octahedron of the Mn^{3+} environment is elongated along one diagonal in the basal plane, which coincides with the direction of the

t_{2g} orbital, while the second octahedron forms a symmetrical trapezoid within the basal plane and hosts the Mn^{4+} ion.

Table 3.2 gives the results of the structure refinement of the D10 data in the $Bbmm$ space group. Additionally to the fractional positions, the absolute shifts from the $I4/mmm$ positions in Å, the rotation of the Mn^{3+} octahedron calculated from the two basal oxygen positions and the bond valence sums for the two inequivalent manganese ions are given.

The deviations from the high temperature $I4/mmm$ positions are quite small, but well established above the uncertainty. For the calculation of the bond valence sum, $\sum \exp(R-R_0/b)$, R_0 and b were taken from [44] as 1.76 Å and 0.37 Å, respectively. This yield the values of 3.50 and 3.72 for the Mn^{3+} and Mn^{4+} site. Opposed to the theoretical complete splitting of the valence into Mn^{3+} and Mn^{4+} ions, only a difference of $0.2 e^-$ is observed which indeed was observed e. g. by resonant x-ray diffraction [37, 45]. Additionally the mean value does not sum up to $3.5 e^-$, which might be attributed to strains in the structure, which strongly influence the bond valence sum. Although there is no structural distortion in $\text{La}_{0.5}\text{Sr}_{1.5}\text{MnO}_4$ above T_{COO} the bond lengths do not perfectly match thereby compressing the RuO_6 octahedra.

LSDA calculation from the derived structure

Local Density Approximation (LDA) calculations can give a deep insight in the electronic ground state and could e. g. reveal the orbital polarization. As the nuclear structure is a crucial input to LDA calculations the availability of the experimental determined structure of the charge and orbital ordered phase of $\text{La}_{0.5}\text{Sr}_{1.5}\text{MnO}_4$ calls for such a calculation with the obtained data. Thus spin-resolved LDA calculations have been performed and analyzed by Dr. Hua Wu and will be presented in this section.

From the different possible ground states, an insulating and antiferromagnetic one proved to be the most stable solution. This is specially remarkable, as LDA and not LDA+U calculations were performed, which conventionally favor metallic ground states and thus the Hubbard U has to be introduced to obtain an insulating one. Furthermore the calculations give only a minor charge separation of the two manganese positions in perfect agreement with the value observed from the bond valence sum. Nevertheless the sites will anymore labelled as Mn^{3+} and Mn^{4+} , but one should keep in mind that the charge modulation is much smaller.

The density of states, as presented in figure 3.7 in the upper left panel, clarifies the orbital occupation for the two manganese sites. The lower diagram shows an equal contribution of both the $x^2 - y^2$ and the $3z^2 - r^2$ orbital to the density of states of the Mn^{4+} site below the Fermi energy, hence no orbital polarization is present. This situation changes for the Mn^{3+} site. Here only the $3x^2 - r^2$ (or $3y^2 - r^2$) orbital contributes significantly to the occupied density of states resulting in a complete orbital polarization. Moreover the LDA findings show that the orbital is a $3x^2 - r^2$ or $3y^2 - r^2$ one, i. e. die dumbbell axis lie in the **ab**-plane and not along

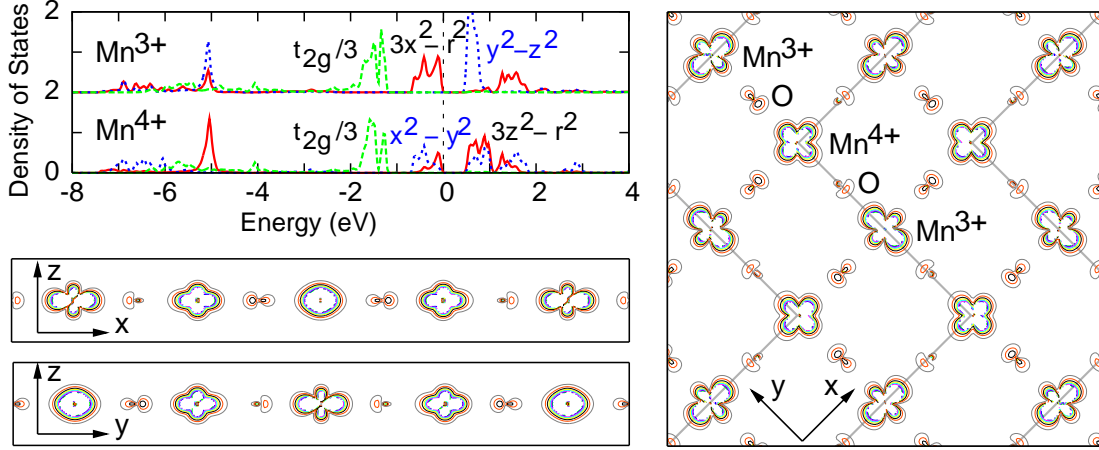


Figure 3.7: Results of the LSDA calculations from Hua Wu based on the atom position from neutron structure refinement. The upper left panel shows the density of states for both Mn^{3+} and Mn^{4+} ions broken down into the single orbitals. The right and left bottom panel show a real space sketch of the e_g electron density within an energy range $-2\text{eV} \leq E \leq 0\text{eV}$ relative to the Fermi energy within and perpendicular to the MnO_2 plane, respectively.

the \mathbf{c} -axis as it would be the case for a $3z^2 - r^2$ orbital.

The two panels on the right and at the left bottom show real space contour plots of the e_g -electron density within the \mathbf{ab} plane and perpendicular to it in direction of the tetragonal axes, respectively. First of all, the orbital arrangement as predicted in the charge and orbital order model is immediately visible likewise the alignment of the dumbbell orbital in the \mathbf{ab} -plane. Furthermore a finite magnetization is present at the oxygen positions, a situation also seen e. g. in $\text{Ca}_{1.5}\text{Sr}_{0.5}\text{RuO}_4$ [46]. Not depicted in the sketch but evident from the raw data is the magnetic order: polarized in the same direction within the zig-zag chains while adjacent chains show a reverse polarization.

The LDA results could clarify the orbital polarization and thereby confirm the charge and orbital order model, especially the detailed orbital polarization which is not directly assessable by neutron scattering. On the other hand the correctness of the structure by neutron scattering is strongly supported, e. g. by the fact that a pure LDA calculation could reproduce the correct insulating ground state.

Summary

The structure determination presented in the previous chapter is not the only indication of a charge and orbital order in the $\text{La}_{0.5}\text{Sr}_{1.5}\text{MnO}_4$ compound. Many other experimental techniques have been employed to investigate this charge ordered half-doped layered manganite.

Senff *et al.* performed an extensive study of the spin waves of $\text{La}_{0.5}\text{Sr}_{1.5}\text{MnO}_4$. They found a soft branch running perpendicular to the large in plane axis and a

much stiffer branch parallel to it and show that only the assumption of a charge- and orbital-order allows to describe the observed data. If a Zener-Polaron order would be realized the soft and stiff branch would be interchanged.

Merz *et al.* [47, 48] performed oxygen 1s and manganese 2p near edge x-ray absorption spectroscopy and found an occupation of the $3x^2 - r^2/3y^2 - r^2$ as predicted by the Goodenough model. Murakami *et al.* [49] performed x-ray resonant scattering and found a charge- and orbital ordering, a result which was indeed questioned by García *et al.* [50] however their analysis yielded two distinct manganese sites a situation found in the CE-type phase but incompatible with a Zener-Polaron order. Later investigations by soft resonant x-ray diffraction performed by Wilkins *et al.* [51, 52], Dhési *et al.* [53] and Staub *et al.* [54] and soft x-ray linear dichroism performed by Huang *et al.* [55] are all in agreement with the proposed charge and orbital order.

These numerous results obtained by different techniques all agree with the finding of our neutron single-crystal diffraction study presented in the previous chapter, namely the validity of the original Goodenough proposal of a combined charge and orbital order. Not a single experiment indicates the Zener-Polaron to be the valid model for layered $\text{La}_{0.5}\text{Sr}_{1.5}\text{MnO}_4$.

3.2.2 Charge and Orbital ordering in the magnetically ordered phase

The determination of the structure of the charge-ordered phase was carried on slightly above the magnetically ordered phase, in order to avoid complications due to the extra magnetic intensities in the neutron diffraction experiment. In order to examine the magnetic structure as well, a second neutron diffraction experiment has been performed at 3 K on a $\text{La}_{0.5}\text{Sr}_{1.5}\text{MnO}_4$ crystal prepared in the course of this thesis on the HeiDi diffractometer at the research neutron source FRM II, Munich. A piece of the sample OJS35EK6 (4 mm height \times \varnothing 5 mm) was mounted on an aluminium pin attached to the cold end of a closed cycle refrigerator, capable of reaching 2.3 K.

The cryostat was mounted on an eulerian cradle and restrained the maximal position of the χ -circle to within about ± 90 deg. The wavelength of the incident beam was chosen to be 0.873 Å by diffraction from a Cu-(220) monochromator, filtered by a 500 μm erbium foil in order to suppress $\lambda/2$ contaminations. Diaphragms in front and after the sample were carefully adjusted in order to reduce the background scattering.

The reciprocal space was exhaustively searched for magnetic reflections. Up to a scattering angle of 50° every possible spot in a primitive orthorhombic lattice, i. e. without accounting for any extinction rules, of the size $10.9 \text{ \AA} \times 10.9 \text{ \AA} \times 24.9 \text{ \AA}$ was recorded. As the magnetic form factor vanishes at higher angles and therefore no magnetic signal is expected, only principal structure reflections and ones that are predicted as strong by the charge and orbital ordered structural model

		D10	Heidi
R_w		4.19	3.82
GoF_w		7.04	8.95
BVS Mn(1)		3.497(4)	3.42(4)
BVS Mn(2)		3.717(6)	3.85(4)
Rot($O_b(1)$)		0.69(3)	0.8(3)
Rot($O_b(2)$)		0.75(3)	1.1(3)
Mn(1)	U_{iso}	0.0008(6)	0.0015(2)
Mn(2)	x	0.50598(8)	0.5084(6)
	U_{iso}	0.0008(6)	0.0015(2)
Ob(1)	x	0.2611(1)	0.2665(11)
	y	0.12748(6)	0.1296(5)
	U_{iso}	0.0044(3)	0.0036(1)
Ob(2)	x	-0.2432(2)	-0.2407(11)
	y	0.1248(1)	0.1250(6)
	U_{iso}	0.0044(3)	0.0036(1)
Oa(1)	z	0.16106(8)	0.1610(6)
	U_{iso}	0.0078(4)	0.0071(2)
Oa(2)	x	0.5059(1)	0.5087(6)
	z	0.16102(7)	0.1606(7)
	U_{iso}	0.0078(4)	0.0071(2)
La/Sr(1)	z	0.35818(5)	0.3579(5)
	U_{iso}	0.0017(3)	0.0016(2)
La/Sr(2)	x	0.5049(2)	0.5072(4)
	z	0.35826(9)	0.3585(5)
	U_{iso}	0.0017(3)	0.0016(2)

Table 3.3: Comparison of the refinement results from the D10 experiment at 130 K and the Heidi experiment at 3 K. The Heidi data suffers from an uncertainty one order of magnitude larger in the positional parameters than in the D10 data, which directly propagates to the interesting BVS parameters.

were collected above 50° . Additional to the conventional ω -scans, Q-scans in the reciprocal space along the l -directions were carried out at selected points. Data reduction was done with a PYTHON program, which resembles the features of the pron2k program but individual integration limits for a reflections persists between invocations. Furthermore it allows to sort and filter the reflections to get a deep insight in the dataset. From the 1575 (946) collected reflections 454 (451) were $I4/mmm$ principal reflections, 498 (322) $Bbmm$ super-lattice reflections and 623 (173) reflections which could not be indexed within the $Bbmm$ space group

and are possibly purely magnetic. Numbers in parentheses denote the number of reflections larger than 3σ .

The careful analysis of the recorded intensities show, that the data from the Heidi-experiment do not give as good results as the D10 data. The uncertainties resulting from the fit of the Heidi data are one order of magnitude larger than the corresponding values in the D10 experiment. Thus a conclusion, whether the structure does strongly change from 130 K to 3 K could not be drawn. Nevertheless the data are presented in table 3.3 and are, at least compatible with the charge and orbital order model.

3.2.3 Crystal structure from X-ray single diffraction

A different way to investigate the crystal structure in the magnetically ordered phase is the use of x-ray instead of neutron radiation. While neutrons probe both the core nucleus potential and the magnetic moment of the electron shell, X-rays only interact with the electron shell and are thus insensitive to the magnetic order. The scattering magnitude is proportional to the square of the electron number and thereby light atoms, such as the interesting oxygen ions give a lower contribution to the scattering signal. In summary their positions and thermal parameters could be determined with much less precision, especially in the presence of heavy ions like lanthanum. On the other side, experiment time on the home laboratory diffractometer, a Bruker X8 Apex equipped with a CCD area detector is much more easily available than beam-time on a neutron diffractometer and the CCD area detector allows to record an enormous number of reflections in a short time. The detector does not only record single reflections, but a large section of the reciprocal space which offers the possibility to re-evaluate the data with different cell-choices or integration parameters or to calculate precession images in order to find unknown superstructure reflections.

The crystal could be cooled by a stream of evaporated liquid nitrogen which allows to reach temperatures as low as 90 K. The cold gas stream is covered by a laminar stream of dry air in order to prevent the formation of frost.⁶Spheres from two different crystals have been measured at the Apex x-ray diffractometer, from a crystal which was prepared by P. Reutler and the crystal OJS35EK6 which was prepared in the course of this thesis. A piece of the first crystal was used for the D10 experiment while a piece of the second one for the Heidi experiment. One set of spheres from the crystal of P. Reutler was prepared from a piece which was immediately available, another set from exactly the sample which was measured at D10 as described in section 3.2. Splinters from all three sources were ball-milled to spheres with a diameter of 100 μm . The spheres were glued with instant adhesive on a glass capillary which was in turn mounted on a brass pin. The

⁶At the lowest temperatures, this occasionally does not work well and could sometimes be attributed to not sufficient dry air in the laminar shield stream. In this case, frost may not only form at the crystal position, but also at the outside of the nitrogen exit nozzle. Above approximately 120 K the situation gradually improves.

	<i>Bbmm</i>		<i>Bbam</i>	
	R _w	GoF	R _w	GoF
OS 120 K	3.87	1.52	3.95	1.58
OS 90 K	3.57	1.45	3.71	1.54
D10 120 K 1	6.33	1.51	6.61	1.60
D10 120 K 2	4.38	1.51	4.72	1.67
D10 90 K	4.89	1.40	5.14	1.46
PR 120 K	3.62	1.52	3.96	1.71

Table 3.4: Agreement factors for the refinement of the low temperature x-ray diffraction data in the cite- and bond-centered charge ordering scenario with space groups *Bbmm* and *Bbam*, respectively. R_w and the Goodness of Fit (GoF) are calculated from all reflections. The refinements in the *Bbmm* consistently give better results. The identifiers of the refinements are explained in the caption of table 3.5

strategy was optimized for achieving a redundancy in the order of 10 within a given experimental time of about 5 days. The measurement times per frame range from 10 s for low scattering angles up to 120 s for the maximum scattering angles which was chosen to be about 120°.

Integration of the resulting images were performed with the SAINT [56] program of the Bruker program suite. SAINT allows the integration of diffraction data from multiple twin domains, which may in turn be corrected for absorption by TWINABS, but for La_{0.5}Sr_{1.5}MnO₄ better results were obtained by performing the integration and absorption correction in the larger 10×10 supercell in which both twins could be described at the same time. The reflections could be later reduced to the smaller cell by the JANA2000 import routine, which at the same time separates the contributions of the twin domains. The absorption correction and scaling of different runs was performed by the SADABS [57] program in the same way as described by Cwik [3].

The resulting reflection file, which is still based on the large 10×10 cell was imported into JANA2000 with a transformation to the smaller 5×10 cell. JANA2000 could automatically handle the assignment of the reflections to the proper twin, if an appropriate twin law is entered.⁷ The refinements were based on F^2 , including the unobserved ($I < 3\sigma$) reflections and the parameters varied include the positional parameters depending on the site symmetry, the diagonal components of the thermal parameters, the scale, an isotropic extinction parameter and two twin fractions from which one handles the $\lambda/2$ contamination. Both models for site- and bond-centered charge ordering were fitted to the data, table 3.4 shows

⁷In this case, the transformation law is $(h/2kl)$. If h is odd, this reflection could not be transformed unless k is even at the same time. Then the reflection is exclusively due to the second twin, e.g the reflection $(321)_{10 \times 10}$ could not be imported for the first twin, but by transformation via $(2\bar{3}1)_{10 \times 10}$ to $(1\bar{3}1)_{5 \times 10}$ for the second one. Note how h and k are interchanged. As the import routine cares about the entered twin matrices, the correction for $\lambda/2$ contamination by a twin matrix $2 * 1$ (twos on the diagonal) has the side effect of allowing reflections to be imported, which are not occurring in the 5×10 lattice and are only due to $\lambda/2$ contamination. As the refinement including these reflections is worse, the twin matrix coping with the $\lambda/2$ contamination has been entered *after* the reflection import.

the agreement factors for both of them. Here, the site-centered charge ordering model gives always the better description of the data, which strongly supports the findings of the single-crystal neutron diffraction experiment at the D10.

The complete results of all refinements are presented in table 3.5. While the answer to the question, which charge order model is realized could be given unambiguously, the uncertainties in the x-ray data does only allow to determine the trend of what happens at the Néel temperature. Especially the distortions of the oxygen environment are larger than from the neutron refinement, which directly passes to the bond valence sums. This has been observed elsewhere [58] but no satisfying explanation could be found. In addition, the uncertainties are about a factor of ten larger for the measurements at 120 K and about a factor of four larger for those at 90 K. Especially the difference in precision between the two temperatures is astonishing, as no fundamental difference in data collection or analysis is present. The experiment time, data completeness and collected region in the reciprocal space certainly differ slightly between the datasets but no distinctiveness of the 90 K datasets is obvious.

Nevertheless it seems clear, that the charge splitting of the Mn^{3+} and Mn^{4+} sites increases at the Néel transition (a difference of 0.220(7), 0.229(26) and 0.17(4) is observed above and 0.423(18) and 0.357(17) below T_N). This is also supported by the larger displacement of the Mn^{4+} site along the \mathbf{a} -direction at 90 K, as this displacement is a direct consequence of the orbital ordering and the thereby caused shift of the basal oxygen atoms. Thus a larger charge and orbital ordering has to lead to a larger displacement of the Mn^{4+} site. For the rotation of the Mn^{3+}O_6 octahedron on the other hand the different results scatter too much to identify a small change.

In summary it can be said that neutron and x-ray results definitively could confirm the site-centered charge and orbital order and rule out the Zener-polaron model. From 120 K to 90 K the charge ordering slightly strengthens but no variation of the rotation of the Mn^{3+}O_6 octahedron could be observed.

3.2.4 Magnetic order at low temperatures

Below 110 K $\text{La}_{0.5}\text{Sr}_{1.5}\text{MnO}_4$ shows antiferromagnetic order. Measurements of the magnetic susceptibility [40], neutron [59] and resonant x-ray diffraction [54] find a predominant alignment of the spins within the \mathbf{ab} -plane while the measurement

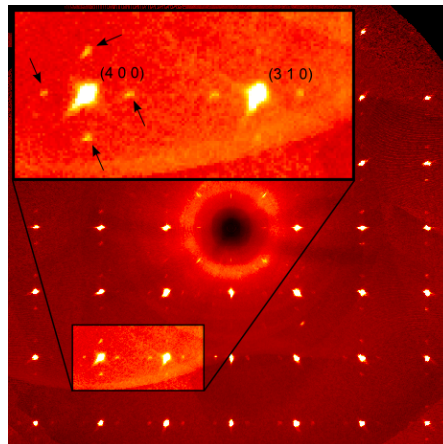


Figure 3.8: $(hk0)$ precession image of $\text{La}_{0.5}\text{Sr}_{1.5}\text{MnO}_4$ at 120 K calculated from the collected frames. The magnified section shows the $(400)_t$ and $(310)_t$ fundamental and the surrounding quarter-indexed satellite reflections. Note that satellite reflections in up-down and left-right direction belong to the different twin domains.

	OS 120 K	OS 90 K	D10 120 K 1	D10 120 K 2	D10 90 K	PR 120 K	D10-exp
a	5.458 (Å)	5.453	5.458	5.458	5.458	5.458	5.452
b	10.923 (Å)	10.905	10.923	10.923	10.923	10.923	10.904
c	12.409 (Å)	12.398	12.409	12.409	12.409	12.409	12.408
$N_{\text{raw,all}}$	36831	50914	37295	43090	46727	43799	1666
$N_{\text{raw,obs}}$	8892	12948	7253	6336	10204	6717	1263
$N_{\text{avg,all}}$	3387	3943	7009	4865	5049	3333	833
$N_{\text{avg,obs}}$	1135	1454	1772	978	1550	742	523
$R_{\text{w,all}}$	3.87 (%)	3.57	6.33	4.38	4.89	3.62	4.19
GoF_w	1.52 (%)	1.45	1.51	1.51	1.40	1.52	7.04
BVS Mn(1)	3.500(18) (e)	3.428(12)	3.54(3)	3.53(3)	3.414(12)	3.49(3)	3.497(4)
BVS Mn(2)	3.729(19) (e)	3.851(13)	3.69(3)	3.60(3)	3.771(12)	3.66(3)	3.717(6)
Δ BVS	0.23(3) (e)	0.423(18)	0.05(4)	0.07(4)	0.357(17)	0.17(4)	0.220(7)
Rot($\text{O}_b(1)$)	0.46(21) (°)	0.89(9)	0.53(25)	0.5(5)	0.85(12)	0.62(38)	0.69(3)
Rot($\text{O}_b(2)$)	1.72(20) (°)	1.25(9)	0.45(26)	0.5(4)	0.96(13)	0.45(40)	0.75(3)
Mn(1)	(0, 0, 0)						
	U_{11}	-0.0002(3)	0.0007(7)	-0.0007(1)	0.0076(5)	-0.0026(2)	0.0015(3)
	U_{22}	0.0005(6)	0.005(1)	0.0086(2)	0.0001(5)	0.0120(3)	0.0015(3)
	U_{33}	0.0040(7)	0.0036(8)	0.00432(4)	0.0038(3)	0.00508(7)	-0.0004(4)
Mn(2)	($x, 1/4, 0$)						
	x	0.50905(8)	0.50360(9)	0.5034(2)	0.50781(9)	0.5050(2)	0.50598(8)
	U_{11}	0.0033(5)	0.0012(2)	-0.0007(1)	0.0044(3)	-0.0026(2)	0.0015(3)
	U_{22}	0.0011(6)	0.0048(4)	0.005(1)	0.0086(2)	0.0120(3)	0.0015(3)
	U_{33}	0.0038(7)	0.0038(5)	0.0038(8)	0.00432(4)	0.00508(7)	-0.0004(4)

Continued on the next page

	OS 120 K	OS 90 K	D10 120 K 1	D10 120 K 2	D10 90 K	PR 120 K	D10-exp
$O_b(1)$	$(x,y,0)$						
	x	0.2625(8)	0.2570(8)	0.256(1)	0.2638(4)	0.260(1)	0.2611(1)
	y	0.1291(3)	0.1261(6)	0.126(1)	0.1280(3)	0.127(1)	0.12748(6)
	U_{11}	0.008(1)	0.0109(6)	0.0064(6)	0.0047(5)	0.0047(9)	0.0051(2)
	U_{22}	0.004(1)	-0.0017(4)	0.0081(6)	0.0059(5)	0.010(1)	0.0051(2)
	U_{33}	0.0061(7)	0.0048(2)	0.0069(2)	0.0063(2)	0.0077(3)	0.0031(2)
	U_{12}	—	0.0005(1)	0.0005(2)	-0.0002(2)	0.0003(3)	0.0005(2)
$O_b(2)$	$(x,y,0)$						
	x	-0.2366(8)	-0.2453(8)	-0.245(1)	-0.2420(4)	-0.244(1)	-0.2432(2)
	y	0.1256(3)	0.1245(7)	0.125(1)	0.1250(3)	0.124(1)	0.1248(1)
	U_{11}	0.0010(9)	0.0109(6)	0.0064(6)	0.0047(5)	0.0047(9)	0.0051(2)
	U_{22}	0.005(1)	-0.0017(4)	0.0081(6)	0.0059(5)	0.010(1)	0.0051(2)
	U_{33}	0.0065(7)	0.0048(2)	0.0069(2)	0.0063(2)	0.0077(3)	0.0031(2)
	U_{12}	—	-0.0005(1)	-0.0005(2)	0.0002(2)	-0.0003(3)	-0.0005(2)
$O_a(1)$	$(0,0,z)$						
	z	0.1610(5)	0.1609(6)	0.1615(4)	0.1620(3)	0.1616(6)	0.16106(8)
	U_{11}	0.005(2)	0.012(3)	0.017(3)	0.007(2)	0.027(4)	0.0089(2)
	U_{22}	0.015(3)	0.011(5)	0.006(2)	0.012(3)	0.010(4)	0.0089(2)
	U_{33}	0.011(3)	0.007(2)	0.025(1)	0.018(1)	0.020(3)	0.0055(2)
$O_a(2)$	$(x,1/4,z)$						
	x	0.5085(3)	0.5093(2)	0.5028(5)	0.5067(2)	0.5044(5)	0.5059(1)
	z	0.1601(5)	0.1605(4)	0.1612(2)	0.1602(2)	0.1609(4)	0.16102(7)
	U_{11}	0.010(2)	0.0110(2)	0.011(2)	0.008(1)	0.004(2)	0.0089(2)
	U_{22}	0.016(3)	0.0110(2)	0.013(2)	0.014(2)	0.014(4)	0.0089(2)
	U_{33}	0.005(2)	0.0078(2)	0.0022(5)	0.0016(5)	0.004(1)	0.0055(2)

Continued on the next page

	OS 120 K	OS 90 K	D10 120 K 1	D10 120 K 2	D10 90 K	PR 120 K	D10-exp
$\text{La}/\text{Sr}(1)$	$(0,0,z)$						
	z	0.35832(6)	0.35851(7)	0.35849(5)	0.35839(3)	0.35840(8)	0.35818(5)
	U_{11}	0.0067(3)	0.0010(2)	0.0052(3)	0.0033(2)	0.0066(3)	0.0021(1)
	U_{22}	0.0029(3)	0.0050(5)	0.0040(4)	0.0046(3)	0.0042(5)	0.0021(1)
	U_{33}	0.0039(3)	0.0031(3)	0.0041(2)	0.0038(1)	0.0048(4)	0.0009(2)
$\text{La}/\text{Sr}(2)$	$(x, 1/4, z)$						
	x	0.50735(4)	0.50298(3)	0.50294(6)	0.50632(3)	0.50470(7)	0.5049(2)
	z	0.35837(6)	0.35834(4)	0.35850(4)	0.35838(3)	0.35845(8)	0.35826(9)
	U_{11}	0.0039(2)	0.0041(1)	0.0046(3)	0.0029(1)	0.0052(3)	0.0021(1)
	U_{22}	0.0028(3)	0.0031(1)	0.0039(4)	0.0043(2)	0.0036(4)	0.0021(1)
	U_{33}	0.0043(3)	0.0040(2)	0.0042(2)	0.0038(1)	0.0044(4)	0.0009(2)

Table 3.5: Structural parameters from the x-ray diffraction refinement of different $\text{La}_{0.5}\text{Sr}_{1.5}\text{MnO}_4$ samples measured on the Bruker X8 Apex diffractometer. Samples were prepared from three different sources. Two of them originate from the same single crystal of P. Reutler. One of them was taken from a piece which was used to observe diffuse scattering (labelled PR) and the second from exactly the piece which was measured at the D10 (labelled D10). The third sample (labelled OS) was taken from the single crystal OJS35EK6 which has been prepared in the course of this these and from which the sample for the Heidi experiment was taken. As reference, the results from the D10 experiment are given in the last column. Measurements have been performed at 120 K and 90 K, the base temperature of the Cryoflex. In addition to the atomic position and thermal displacements, the lattice constants used in the refinement, the number of measured and inequivalent reflections, split to all and $> 3\sigma$, the weighted agreement factor and the goodness of fit, the Bond Valence Sums for the two manganese positions including their difference and the rotations of the MnO_6 octahedron calculated from both basal oxygen positions are shown.

of the spin-wave dispersion from Senff *et al.* [42] yield the relevant coupling constants. These show that the predominant coupling is a ferromagnetic one along the chains. Therefore, below the Néel temperature, a ferromagnetic order within the chains is established and subsequently neighboring chains order antiferromagnetically. The direction of the spins within the plane is on the other hand unclear. While Sternlieb *et al.* suggest a direction of $(210)_t$ for the spins corresponding to an angle of 26.4° with the $(100)_t$ direction, Staub *et al.* found only a deviation of $10\pm 5^\circ$ from the $(100)_t$ direction. Thus a determination of the magnetic structure is of great interest, especially now, that the nuclear crystal structure could be determined. Two measurements were performed to get a deeper insight in the magnetic structure at low temperatures. First a neutron powder diffraction at the G4.1 high flux diffractometer at the Orphée reactor in Saclay at different temperatures was performed. The second measurement was the single-crystal measurement at the Heidi diffractometer described in section 3.2.2 which unfortunately yields a limited quality of the obtained results. While a refinement of the nuclear structure could be performed, the magnetic intensities could not be evaluated to obtain a sensible result. Most likely this is caused by a far from perfect integration of the broad magnetic signal by the diffractometer. Thus only the measurement of the G4.1 experiment will be discussed here.

Figure 3.9 shows the measurement at 1.5 K on the G4.1 diffractometer. In addition to the measured data and the corresponding fit, the reflection intensities derived from the single-crystal measurement at the Heidi diffractometer are drawn, corrected for the Lorentz factors due to the different geometries. The data were fitted with the FULLPROF program utilizing two phases a nuclear and a purely magnetic one. The nuclear part was described in the 5×10 cell using the structure obtained from the D10 refinement. A fit of the position parameters leads to very large, non-physical displacements of the atoms and has thus been discarded. The profile parameters and the lattice constants on the other hand have been fitted with the b lattice parameter constrained to be the double of a .⁸

The magnetic part was is a first step described according to the model of Sternlieb *et al.* in the $10\times 10_b$ cell as a second purely magnetic phase.⁹ $P1$ was chosen as the symmetry of the magnetic phase in order to allow all 32 manganese atoms to be entered manually. The spins were constrained to lie within the **ab** plane and within a zig-zag element all Mn^{3+} and Mn^{4+} point in the same direction. Spins in adjacent zig-zag chains then point in opposite direction. The stacking in the **c**-direction is performed by consecutively applying the pseudo centering operation $(1/4\ 0\ 1/4)$. The resulting fit could describe most of the magnetic peaks with a reasonable accuracy. Peaks which are observed but show a vanishing calculated

⁸FULLPROF calculates the d value from the expression $Ah^2 + Bk^2 + Dl^2 + Dkl + Ejl + Fhk$, with A to F derived from the lattice constants. Thus the shift encoded in the codeword of a has to be four times that of b instead of the intuitive assumed value of one half.

⁹FULLPROF allows multiple phases only for powder refinements. Refinements of single-crystal data have to be performed with a combined nuclear and magnetic phase and in the case of $\text{La}_{0.5}\text{Sr}_{1.5}\text{MnO}_4$ with the propagation vector formalism.

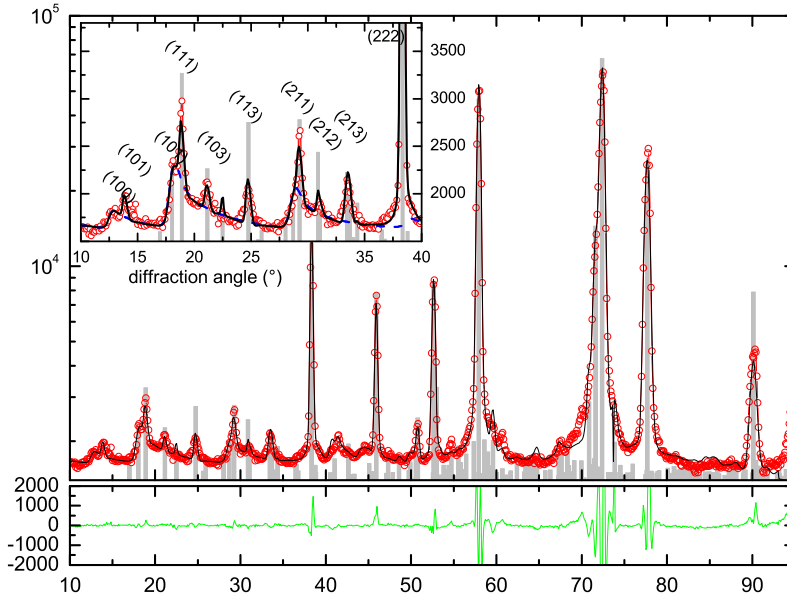


Figure 3.9: Low temperature neutron powder diffraction pattern of $\text{La}_{0.5}\text{Sr}_{1.5}\text{MnO}_4$ taken at the G4.1 high flux diffractometer. The diffractogram was recorded at a temperature of 1.5 K with a wavelength of 2.424 Å. Red points show the G4.1 data, while the gray bars show the peak heights calculated from the Heidi single-crystal diffraction data. The black line is a fit with the structural parameters taken from the D10 experiment and a magnetic order as described in the text. The dashed blue line correspond to the two dimensional order alone. The inset shows a magnified view of the low angle part where mostly magnetic scattering is observed. The reflections are labelled according to the $10 \times 10_b$ cell. The small lower panel shows the differences between observed and calculated intensities.

intensity include (100), (110) and (210), eg. those having no l component. Very interestingly the profile of these peaks shows an extreme asymmetry and resembles some sort of exponential decay on the high angle side.

As this could be attributed to a two dimensional order, in a second step, a further magnetic phase was introduced, which models a two dimensional order of only one single MnO_2 layer. This was achieved by an approach described by Ufer *et al.* [60] where the lattice constant perpendicular to the 2D order is enlarged¹⁰ and only a single layer of the unit cell is occupied. This enlargement results in a large density of reflections in l -direction and due to the finite width of the individual peaks to a smearing into scattering rods as expected for a two dimensional order. In addition FULLPROF allows for a special type of broadening which on the one hand smoothes the remaining wiggles and on the other treats reflections (00 l) in a special way in order to conserve them. With this model, the data could be described reasonable well, e.g in the low angular region only the (113) $_{10 \times 10_b}$ reflection shows a calculated intensity but is not observed. This and some other

¹⁰in this case to ten times the conventional length

minor deviations might be addressed by a more sophisticated model which has indeed been tried, but the quality of the data does not easily allow to distinguish among them.

Nevertheless this fit clearly shows the simultaneous 2d and 3d nature of the magnetic ordering, even at 1.5 K well in the magnetic ordered state. The magnetic moments derived from the fit are $2.52(30) \mu_B$ for the Mn^{3+} site and $2.33(24) \mu_B$ for the Mn^{4+} site while the angle between the spins and the \mathbf{a} -axis, i. e. the stacking direction of the zig-zag chains, is about 17° . A reliable estimate of the uncertainty is rather difficult. FULLPROF returned a large relative uncertainty of 100% which basically renders the value useless.¹¹ In order to investigate this issue, χ^2 as function of the rotation angle has been determined. This was done by fixing the angle to the desired value and refining the remaining parameters for the magnetic phase. The resulting curve is shown in figure 3.10. The origin of the large error is immediately obvious, namely a rather flat valley around 0° with an extremely small local maximum at the center. The minimization algorithm of FULLPROF now moves within this double well potential and at some point stays in one of the minima around -17° or 17° . The derivation of χ^2 with respect to the spin direction at that point enters reciprocally in the computation of the uncertainty. As the valley is quite flat, the derivative is small and thus the error gets large. A different way to estimate the uncertainty is via a fit of a symmetric fourth order polynomial and determine its minima. This gives certainly the same rotation angle of $\pm 17^\circ$ but now with a small uncertainty of 3° (14%). A better estimate might lay in the middle of these two values, e.g. $\phi = 17(10)^\circ$.

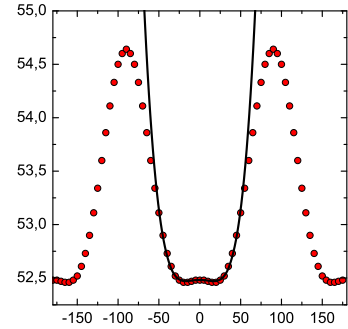


Figure 3.10: Variation of χ^2 as function of the spin direction from a series of FULLPROF runs. No parameters were allowed to vary. The flat valley around hosts in fact a very tiny double-well potential.

Summary

The preceding section presented the investigations performed on the half-doped layered manganite $\text{La}_{0.5}\text{Sr}_{1.5}\text{MnO}_4$. Numerous structure refinements could show that this system features the charge and orbital order originally proposed by Goodenough and no indication was found that the Zener-Polaron might still be a relevant model. These diffraction based experiments finally complete the picture already drawn by the many other experimental techniques applied to this system.

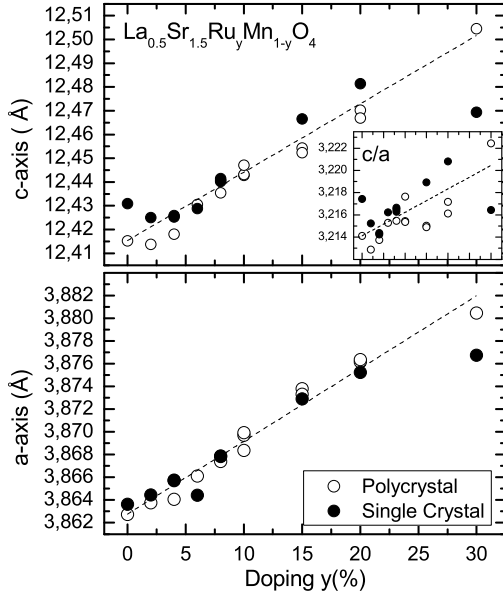


Figure 3.11: Room temperature lattice constants of ruthenium co-doped $\text{La}_{0.5}\text{Sr}_{1.5}\text{MnO}_4$ as function of doping derived from X-ray powder diffraction. The diffractograms show no indication for an impurity phase nor for a structural phase transition, e.g. to a 5.4×5.4 cell. Both lattice constants increase upon ruthenium doping, but the increase of the c lattice constant is stronger, as could be seen by the c/a ratio shown in the inset. For the single crystal measurements, small non-surface pieces of the crystal were grounded.

3.3 Ruthenium co-doping

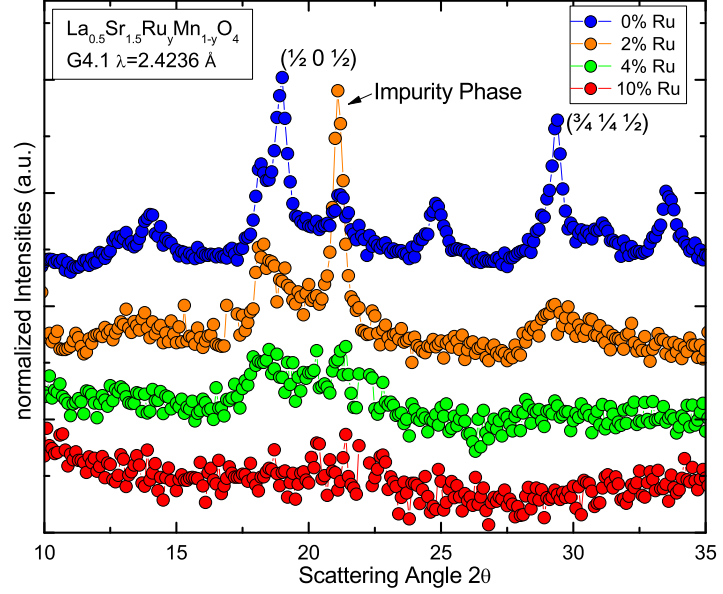
The results of Tokunaga *et al.* [62], namely the drop of the resistivity of $\text{La}_{0.5}\text{Sr}_{1.5}\text{MnO}_4$ only at the extremely high magnetic field of 25 T, suggest a very stable antiferromagnetic order. Because of the high field, needed to drive the system to a metallic behavior, thermodynamical and transport measurements on the colossal magnetoresistivity and the interplay of ferro- and antiferromagnetism in the home laboratory, where such high fields are not available are not feasible for the layered compounds. As they are otherwise extremely well suited for structural studies, because of the absence of complicated twinning as in the perovskite manganites a weakening of the order in the layered manganites and a thereby reduced critical field would be of great interest in order to combine the results of structural studies with high field experiments.

For the three dimensional manganites a partial replacement of the manganese ion with other transition metals has been investigated for goal. Raveau *et al.* [63] and Shames *et al.* [64] report that the inclusion of ruthenium in the CMR materials weakens the antiferromagnetic order and finally leads to a ferromagnetic ground state. Also the co-doping of layered manganites with rhenium and ruthenium [65, 66] has been reported but has not been done at half doping in case of rhenium and with rather high doping level in case of ruthenium.

Thus a series of powder samples was prepared for both $x=0$ and $x=1/2$ and additionally some ruthenium co-doped single-crystals of the $x=1/2$ series were grown with special attention to low co-doped samples. Room temperature X-ray diffraction shows no indications of an impurity phase or a phase transition. The room temperature lattice constants derived from the diffractograms are shown in fig-

¹¹However FULLPROF multiplies the statistical error with the goodness of fit thereby strongly enhancing the errors in our case. [61]

Figure 3.12: Low temperature diffractograms of ruthenium co-doped $\text{La}_{0.5}\text{Sr}_{1.5}\text{Mn}_{1-y}\text{O}_4$ for $y=0\%$, 2% , 4% and 10% . Samples were measured on the high flux neutron diffractometer G4.1, LLB Saclay at stabilized temperature of 10 K. The data were scaled to same principal peak intensities and shifted for clarity.



ure 3.11. Both lattice constants show an increase with doping of $1.66(5)\%$ / Ru and $2.3(2)\%$ / Ru for the \mathbf{a} and \mathbf{c} -axis, respectively. Only the single-crystal for $y=30\%$ shows a strong deviation, while the powder sample of the same nominal composition fits the linear dependence. This is presumably due to the high evaporation of ruthenium during the single-crystal growth. This is supported by the fact, that this single-crystal has decayed to small and very thin platelets within a few days, while the other ruthenium doped single-crystals are more stable.

3.3.1 Neutron powder diffraction

On these samples a series of neutron scattering experiments have been carried out. Two powder samples of $x=0$ with a ruthenium concentration $y=5\%$ and $y=10\%$ and four with $x=1/2$ and ruthenium concentrations $y=(0, 2, 4, 10\%)$ have been measured on the G4.1 high flux powder diffractometer at the LLB, Saclay. This is located at a cold neutron guide for decreased background of parasitic γ -radiation from the reactor core and employs a 80° wide position sensitive detector in order to yield a high count rate and thereby allows to study structural and magnetic phase transitions as function of temperature. We used a wavelength of 2.4236 \AA and placed about 1.5 cm^3 of the sample in a vanadium container which in turn was mounted inside a helium bath cryostat, which allows to vary the temperature between 1.5 K to 290 K. The sample was cooled down to the lowest desired temperature and diffractograms were taken at several temperature steps when the temperature has sufficiently stabilized.

The results of a neutron powder diffraction measurement are presented in figure 3.12. Shown is the low angular region, where no nuclear scattering is expected. Here the un-doped sample shows well-defined magnetic peaks, which are already discussed in section 3.2.4. The $y=2\%$ and 4% show the same anisotropic peak at

$(\frac{1}{2} 0 \frac{1}{2})$ and $(\frac{3}{4} \frac{1}{4} \frac{1}{2})$ which were confirmed to be signature of a two dimensional order in the pure compound. The three-dimensional magnetic order on the other hand is totally suppressed even with a low value of only 2% of ruthenium. As could be clearly seen from the diffractograms, the two dimensional signal diminishes upon ruthenium doping and in the $y=10\%$ sample, no magnetic signal could be observed at all.

Thus ruthenium is rather effective in suppressing the magnetic order, as a concentration of only 2% is sufficient to eliminate the three dimensional order while the two dimensional order persists at least in the 4% sample. The limited accessible \mathbf{Q} space with the wavelength of 2.4236 Å does unfortunately not allow to follow the effect of the ruthenium doping on the charge and orbital order, especially as the visible peaks are rather weak. This could be overcome by the elastic TAS scattering due to the much increased signal/noise ratio presented in the next section.

3.3.2 Elastic TAS measurements at the IN12

A single-crystal neutron scattering experiment has been carried out at the IN12 cold triple axis spectrometer at the ILL, Grenoble. We conducted only elastic measurements where the analyzer greatly increased the signal-to-noise ratio. Incident and final wavevector are fixed to $\mathbf{Q}=1.97 \text{ \AA}^{-1}$ in order to reach a sufficient part of the reciprocal space and to reduce the $\lambda/2$ contamination to a minimum. A pyrolytic graphite filter was employed for an even further $\lambda/2$ -reduction.

Figure 3.13 shows the magnetic diffuse scattering from the $y=2\%$ and $y=8\%$ $\text{La}_{0.5}\text{Sr}_{1.5}\text{Ru}_y\text{Mn}_{1-y}\text{O}_4$ sample. Shown are scans in the tetragonal $(1 \bar{1} 0)$ direction running over $(1 0 0)$ and $(\frac{3}{4} \frac{1}{4} 0)$. These positions correspond to a ferromagnetic signal due to short ferromagnetic ordered zig-zag chain units and the long range CE-type order, respectively. The plot for $y=2\%$ on the left resembles what has been seen in the pure $x=\frac{1}{2}$ sample¹². At high temperatures a broad ferromagnetic signal is present, which disappears upon cooling and for which the CE-type signal emerges which is remarkable sharp. Only the transition temperature has dropped slightly compared to the non ruthenium doped sample. The apparent extension of the ferromagnetic signal down to low temperatures is most probable an artefact caused by the subtraction of the $\lambda/2$ contamination. This situation changes for the $y=8\%$ sample on the right. The ferromagnetic part extends down to lowest temperatures and the CE-type signal is quite broad, showing a hammock type peak shape between $(1 0 0)$ and $(\frac{3}{4} \frac{1}{4} 0)$ which already has been seen in similar experiment with a pure $x=0.4$ sample. This peak shape follows in the $x=0.4$ sample from the unbalanced doping which prevents the formation of a perfect zig-zag chain ordering and finally results in an increased magnetic signal in the $(1 \bar{1} 0)$ direction. The Néel temperature is reduced to approximately 70 K and the overall signal intensity is quite weak.

¹²compare this to Senff [67], figures 4.10 and 4.22

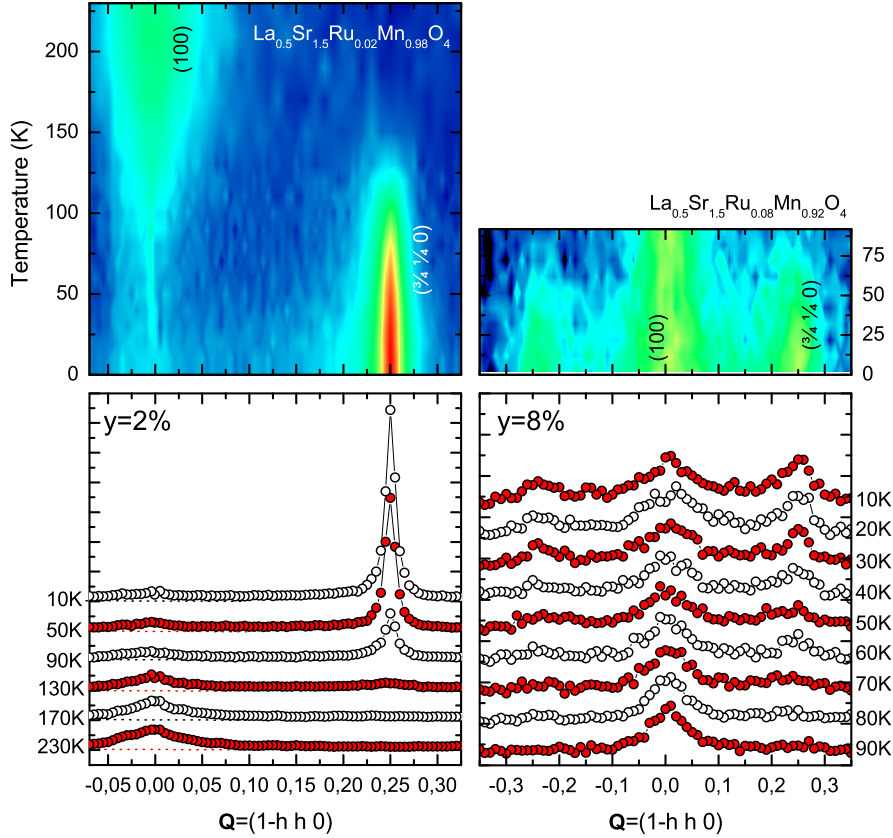


Figure 3.13: Comparison of the diffuse magnetic scattering of two $\text{La}_{0.5}\text{Sr}_{1.5}\text{Ru}_y\text{Mn}_{1-y}\text{O}_4$ samples. The scans run in the $(1\bar{1}0)$ direction and cross the ferromagnetic signal at (100) and the CE-type magnetic signal at $(\frac{3}{4} \frac{1}{4} 0)$. The bottom panels show some of the raw scans used for the intensity maps shown on top. The panels on the left show the data for $y=2\%$ while those for $y=8\%$ are displayed on the right. From the raw data, the narrow signal at (100) due to $\lambda/2$ contaminations have been subtracted.

Figure 3.14 displays the temperature evolution of the magnetic and structural superstructure peaks for both the $y=2\%$ and $y=8\%$ sample. In order to compare the strength of the superstructure peaks the peak area normalized to the $(110)_t$ peak is plotted. Thus the magnitudes of equivalent peaks could be compared between these two samples. Exceptions are the $(\frac{1}{2} 0 0)$ peaks. These have been scaled to the $(\frac{3}{4} \frac{1}{4} 0)$ signal in order to illustrate the same course. Fits to the data yield in transition temperatures of $T_N=121(4)$ K and $T_{CO}=219(5)$ K for the $y=2\%$ sample and $T_N=111(19)$ K and $T_{CO}=156(46)$ K for the $y=8\%$ sample, respectively. Like in the pure compound, the signal of Mn^{3+} and Mn^{4+} ions probed by the $(0.75 \ 0.25 \ 0)$ and $(0.5 \ 0 \ 0)$ reflections show exactly the same course. While the transition temperatures for the 2% sample lie close to those of the pure compound, the order is highly suppressed in the higher doped sample. Additionally the relative intensity of all superstructure peaks strongly decreases, e. g. for the

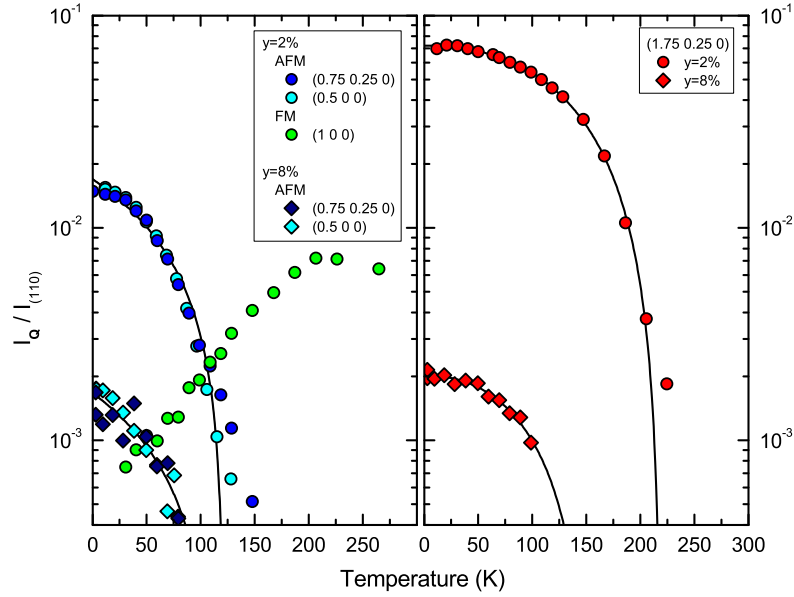


Figure 3.14: Temperature dependence of the superstructure peaks in $\text{La}_{0.5}\text{Sr}_{1.5}\text{MnO}_4$ ruthenium co-doped with 2% and 8% determined by elastic neutron scattering. The peaks were fitted by a gaussian whose peak area (intensity times width) was normalized to the $(110)_t$ peak. The left panel shows the evolution of the magnetic peaks, while the superstructure peaks corresponding to the charge and orbital order are shown to the right.

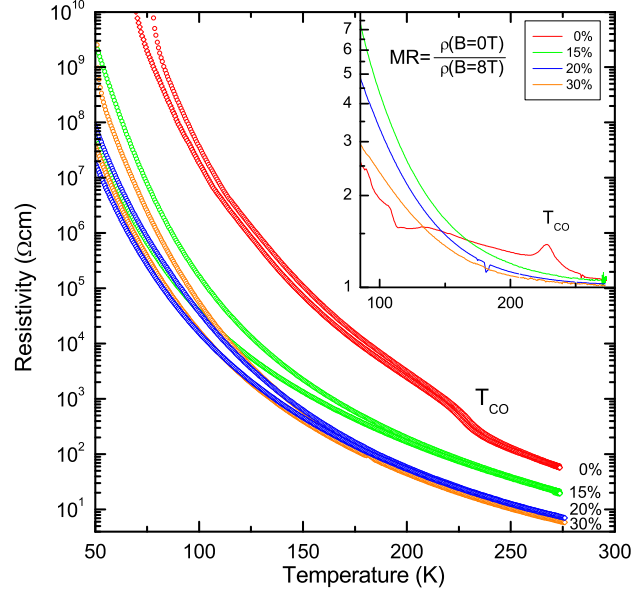
structural superstructure by a factor of approximately 35. As the magnitude of displacements enter linearly¹³ in the structure factor of superstructure peaks this implies a reduction of the displacements by roughly a factor of six in the 8% sample. The neutron scattering shows the strong efficiency of ruthenium to suppress the magnetic and at the same time the structural order in $\text{La}_{0.5}\text{Sr}_{1.5}\text{MnO}_4$. At a level of 8% the system is already quite strongly disordered. Thus the results of the resistivity measurements shown in figure 3.15 are not astonishing. The resistivity of $\text{La}_{0.5}\text{Sr}_{1.5}\text{Ru}_y\text{Mn}_{1-y}\text{O}_4$ samples with ruthenium concentrations of 0%, 15%, 20%, 30% have been measured in magnetic fields of 0 T and 8 T. The pure compound shows strong anomalies in the magnetoresistivity curves, both the charge ordering as well as the onset of the magnetic order can be seen. These effects vanish for the ruthenium doped samples, here the magnetoresistivity curves simply smoothly rise. As the neutron scattering shows a strong suppression of the order already at 8%, a total disappearance of the order at 15% is more than certain.

¹³If r_j denotes the position of the j th atom in the non-displaced structure and ϵ_j its displacement, the structure factor F_{hkl} reads as

$$F_{hkl} = \sum b_j e^{ik(r_j + \epsilon_j)} = \sum b_j e^{ikr_j} \underbrace{e^{ik\epsilon_j}}_{\approx 1 + ik\epsilon_j} = \sum b_j e^{ikr_j} + i \sum b_j k \epsilon_j e^{ikr_j}$$

The first sum vanishes as hkl is assumed to be a superstructure peak.

Figure 3.15: Resistivity in the ab-plane of ruthenium co-doped $\text{La}_{0.5}\text{Sr}_{1.5}\text{MnO}_4$ as function of temperature for magnetic fields of $B=0\text{ T}$ and 8 T . The inset shows the magnetoresistivity curves, $\text{MR}=\frac{\rho(B=0\text{ T})-\rho(B=8\text{ T})}{\rho(B=0\text{ T})}$. Data were taken from ref. [68]. Only the pure and highly doped samples were under investigation in this work, no data is available for the 2% to 8% samples.



Summary

The substitution of the manganese ions with ruthenium in the half-doped $\text{La}_{0.5}\text{Sr}_{1.5}\text{MnO}_4$ clearly results in a reduction of the charge and orbital order and the magnetic order. At $y=8\%$ the charge order temperature is reduced from 225 K to approximately 125 K and strength of the signal is reduced as well. The resistivity is indeed reduced by the ruthenium substitution, but no metallic phase is observed, even at a replacement of 30% of the manganese ions by ruthenium. This might be up to an increased stability of the charge order in the 2D manganites or to the reduced dimensionality of the system itself. The latter concept arises from the fact, that the percolation limit in two dimensions is higher than in three. If a microscopic phase separation between metallic and insulating phases is present more metallic phase has to be present in the 2D case to observe macroscopic conductance. A conclusion if the an increased stability, the reduced dimension or a completely different reason is responsible for the system staying an insulator could not be drawn from the available data.

Ruthenium co-doping of $\text{La}_1\text{Sr}_1\text{MnO}_4$

While the work on manganites was mainly focused on the half-doped ones, some activities in the ruthenium doping of $\text{La}_1\text{Sr}_1\text{MnO}_4$ were conducted and the results will be discussed here. Samples with 5% and 10% ruthenium doping were prepared by the standard solid state reaction and phase purity was checked by x-ray diffraction.

Figure 3.16 shows the lattice constants of the samples with 5% and 10% ruthenium and compares that with the pure $\text{La}_1\text{Sr}_1\text{MnO}_4$ and the hole doped $\text{La}_{7/8}\text{Sr}_{9/8}\text{MnO}_4$. The data for the non-ruthenium doped samples were taken from [6]. The solid symbols indicate data which were obtained by x-ray pow-

der diffraction while the data marked with open symbols were measured on the high flux neutron diffractometer G4.1. This instrument is optimized for high flux and high detection efficiency for rapid data collection at medium resolution by using a large multidetector and a long wavelength, which reduces its precision in lattice constant measurements.

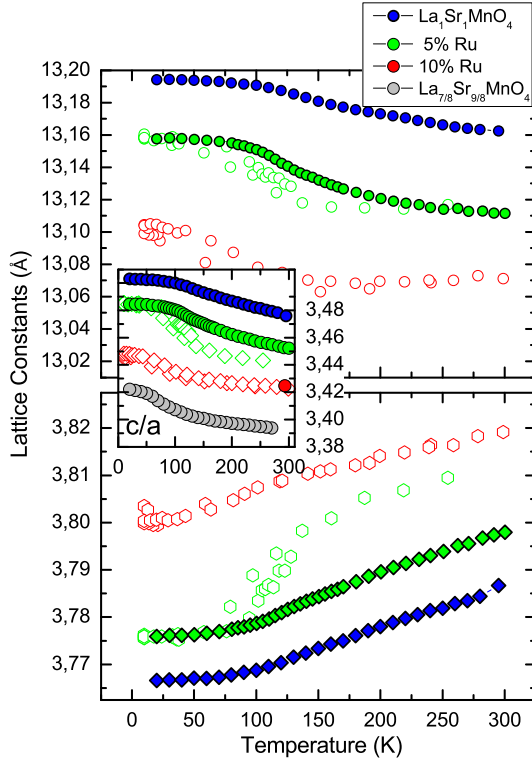


Figure 3.16: Temperature dependency of the lattice constants of $\text{La}_1\text{Sr}_1\text{Ru}_y\text{Mn}_{1-y}\text{O}_4$ for $y=0\%$, $y=5\%$ and $y=10\%$. The data marked with solid symbols was determined by x-ray powder diffraction while data with open symbols originate from the G4.1 measurement. The data for non ruthenium doped samples were taken from [6].

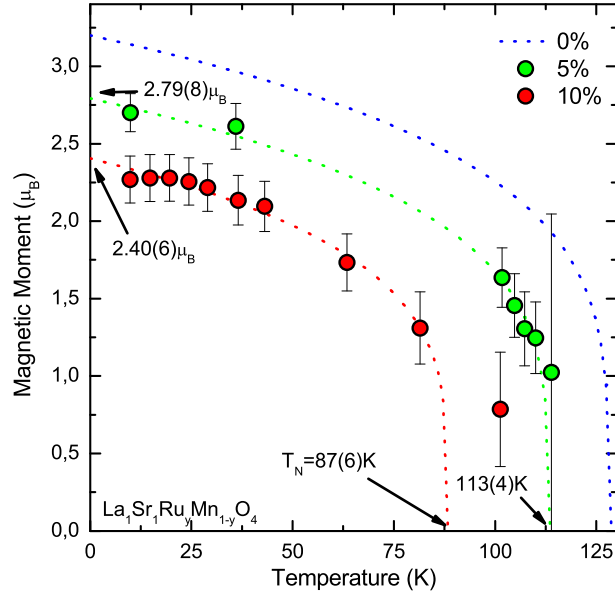
orbital occupation is reduced. Furthermore the orbitals in the vicinity could flip in the ab -plane and form an orbital polaron [69]. Thus one doped hole could compensate the effect of more than one $d_{3z^2-r^2}$ orbital explaining the large effect of the doping on the c/a ratio. The decrease of the c/a ratio upon a temperature increase results from a thermally induced population of the in-plane $d_{x^2-y^2}$ orbital.

In order to obtain more information on the magnetism, two samples with ruthenium concentrations of $y=5\%$ and $y=10\%$ were measured at the high flux neutron diffractometer G4.1 at the LLB, Saclay, France. The samples were cooled to 10 K and measured upon heating at several discrete and well stabilized temperature steps. Data were recorded with a large position sensitive detector in the range

Furthermore the measurements were performed at low scattering angles in order to record possible low-indexed superstructure peaks, therefore only few fundamental structure peaks were recorded by the stationary and fixed-angle multidetector, causing the larger scatter of the data compared to the x-ray measurements. The overall course of the two a and c lattice constants are the same while the absolute values changes. The a lattice constant increases upon doping, while the c lattice constant decreases. This flattening of the structure is equally seen in the c/a ratio, which is shown in the inset. Also here, the course of the c/a ratios are basically the same, indicating that no fundamental change in the system takes place. For comparison the c/a ratio for $\text{La}_{7/8}\text{Sr}_{9/8}\text{MnO}_4$ is shown indicating that the ruthenium doping is not more effective than the conventional hole doping.

D. Senff [6] could show in his diploma thesis, that the c/a ratio is an indicator for the occupation of the $d_{3z^2-r^2}$ orbital. With increased doping, the e_g electrons are removed and thus the orbital

Figure 3.17: Magnetic moment of $\text{La}_1\text{Sr}_1\text{Ru}_y\text{Mn}_{1-y}\text{O}_4$ as function of temperature from refinements of neutron powder diffractograms. The $y=5\%$ and 10% samples were measured on the G4.1 diffractometer, LLB Saclay and show both the same magnetic order as $\text{La}_1\text{Sr}_1\text{MnO}_4$. The data are fitted by a function of the form $M \cdot (1 - (T/T_c)^n)$. For the undoped compound, $M(T=0)$ and T_c are taken from [40] the corresponding curve is included as reference. The exponent n was constrained to the same value for all three curves.



$8^\circ \leq 2\theta \leq 88^\circ$ and the resulting diffractograms were fitted with the FULLPROF program. No indication that the magnetic structure deviates from the one found by P. Reutler for the undoped compound. Figure 3.17 displays the refined magnetic moments of the two samples. As expected the effective moment and the transition temperature decreases with increasing ruthenium content.

Summary

The effect of the ruthenium co-doping of $\text{La}_1\text{Sr}_1\text{MnO}_4$ has to be compared with that of the variation of the lanthanum/strontium ratio in the system $\text{La}_{1-x}\text{Sr}_{1+x}\text{MnO}_4$. In the pure compound, only Mn^{3+} is present which possesses one electron in the e_g orbitals. Here the $3z^2-r^2$ orbital which extends in the c -direction is predominantly occupied and thus leads to an elongation of the structure along c . Upon hole-doping, these orbitals are on the one hand simply depopulated, on the other hand neighboring $3z^2-r^2$ may flip into the plane forming an orbital polaron. This explains the strong reduction of the c/a ratio upon strontium doping, the room temperature value is reduced from 3.476 to 3.394 or 24.2% for a hole doping of 12.5%. Normalized to 1% doping this results in an efficiency of $24.3/125=0.194$.

For the comparison with the ruthenium co-doping one has to consider the valence state of the ruthenium ion which is presumably tetravalent¹⁴, having three electrons in the 4d shell. Thus the inclusion of ruthenium leaves more electrons left for the manganese, leading effectively to an electron doping and thus increased occupation of the manganese e_g orbitals. To obtain solely the effect of the ruthenium inclusion, electron doped manganites with $x=-0.05$ and $x=-0.1$ were prepared, see figure 3.18. The electron doping has unambiguously a much weaker effect on the

¹⁴The most stable oxidation state of ruthenium is 4+

lattice than the hole doping which strengthens the assertion of the orbital induced lattice elongation. In this picture, the removing of an orbital including the formation of an orbital polaron has clearly a stronger effect on the lattice than a simple double occupation.

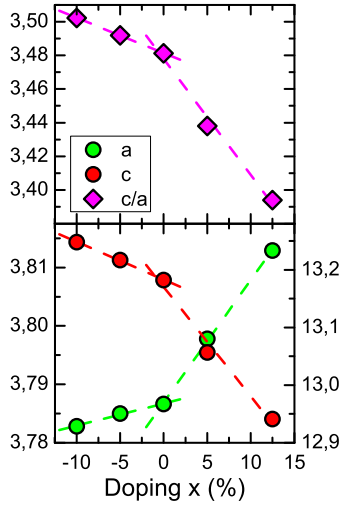


Figure 3.18: Lattice constants and c/a ratio of electron doped manganites.

Using these data, one can calculate the effect of the ruthenium inclusion on the lattice. For $y=5\%$ the c/a ratio decreases from 3.486 in $\text{La}_{1.05}\text{Sr}_{0.95}\text{MnO}_4$ to 3.453 in $\text{La}_1\text{Sr}_1\text{Ru}_{0.05}\text{Mn}_{0.95}\text{O}_4$ or by 9.6%. For $y=10\%$ the decrease is from 3.496 to 3.425 or by 20.8%. These numbers result in efficiencies of 0.192 and 0.208, respectively which are very close to the 0.194 derived for the lanthanum/strontium doping.

This shows that the inclusion of ruthenium has basically the same effect as introducing an equal number of holes. That implies that orbitals in the vicinity of the ruthenium site form an orbital polaron and the ruthenium inclusion has neither a stronger nor a weaker effect on the orbital polarization than a hole, i. e. a Mn^{4+} ion. In this sense, ruthenium co-doping and hole doping are equivalent.

3.4 Properties of $\text{Pr}_{0.5}\text{Ca}_{1.5}\text{MnO}_4$

In contrast to the well studied layered perovskite system $\text{La}_{1-x}\text{Sr}_{1+x}\text{MnO}_4$, much less information is available for related compounds with different A-site atoms like $\text{Pr}_{1-x}\text{Ca}_{1+x}\text{MnO}_4$. This is remarkable, as several compositions of the 3D-perovskite manganites are handled in detail in the literature, namely compounds with lanthanum, praseodymium or neodymium as trivalent and calcium or strontium as divalent cations.¹⁵ Even in the sparse literature dealing with layered manganites other than the $\text{La}_{1-x}\text{Sr}_{1+x}\text{MnO}_4$ series, the description of the charge order at $x=1/2$ is not consistent. While Ibarra *et al.* [70] found an incommensurate ordering with a propagation vector of 0.43 in \mathbf{b} -direction, Chao *et al.* [71] and Chi *et al.* [72] found a commensurate structure. From the latter two, Chao *et al.* did not even consider the orthorhombicity, while Chi *et al.* found a doubling of unit cell in b direction.

We therefore investigated $\text{Pr}_{1-x}\text{Ca}_{1+x}\text{MnO}_4$ as a second example of a complex ordered layered manganite, in order to test whether the found charge and orbital order in $\text{La}_{0.5}\text{Sr}_{1.5}\text{MnO}_4$ is a generic feature, at least for the layered manganites or if the Zener polaron still might be a relevant model.

¹⁵The ISI Web of Knowledge lists 402, 105, 71, 72, 85 and 145 papers for half-doped 3D-manganites with LaCa, PrCa, NdCa, LaSr, PrSr and NdSr, respectively, 164 papers for $\text{La}_{0.5}\text{Sr}_{1.5}\text{MnO}_4$ but only 3 for $\text{Pr}_{0.5}\text{Ca}_{1.5}\text{MnO}_4$.

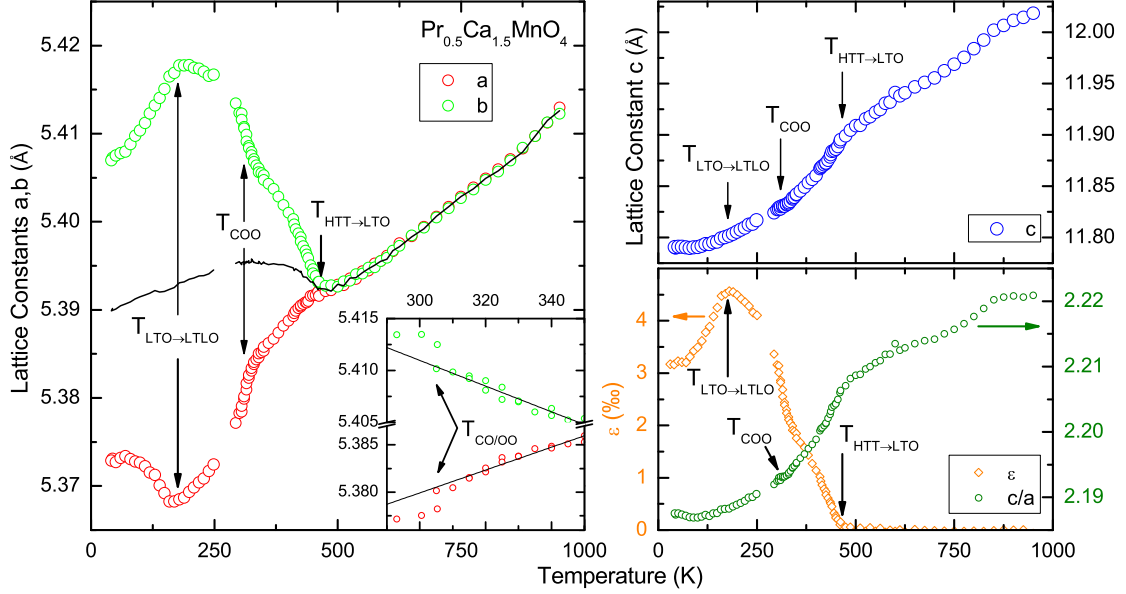


Figure 3.19: Temperature dependent lattice constants of $\text{Pr}_{0.5}\text{Ca}_{1.5}\text{MnO}_4$ from 20 K up to 1000 K. Coming from high temperatures, the system undergoes a structural transition from a tetragonal symmetry to an orthorhombic one at 466(2) K. Just above room temperature, an anomaly in the a and b lattice constants is observed, as shown in the inset. At 176(2) K, the difference between a and b starts to shrink, but the cell does not become tetragonal down to lowest temperatures.

3.4.1 Basic Properties

Figure 3.19 shows the results of a x-ray powder diffraction measurement from 30 K up to 1000 K. At high temperatures, the cell was found to be tetragonal. Upon cooling it exhibits a transition to an orthorhombic phase, as seen in the split of the a and b lattice constants. This is different to $\text{La}_{0.5}\text{Sr}_{1.5}\text{MnO}_4$ which stays tetragonal down to the charge charge ordering and does not even show an orthorhombic splitting in the charge and orbital ordered phase despite its orthorhombic symmetry $Bbmm$. A fit to the orthorhombic splitting yields a transition temperature of $T_{\text{HTT} \rightarrow \text{LTO}} = 466(2)$ K for the transition from the high temperature tetragonal (HTT) to the low temperature orthorhombic (LTO) structure. Close to room temperature, a very weak anomaly can be observed in both a and b but not in c lattice constants where the orthorhombic splitting is increased. This anomaly coincides with the metal-insulator transition observed in the resistivity and is an indication of a charge and orbital order. At 176(2) K the orthorhombicity shows a maximum and is then reduced but stays finite down to lowest temperatures. This is presumably a structural phase transition from the LTO to a LTLO (low temperature less orthorhombic) phase.

Figure 3.20 displays the results of the magnetization and resistivity measurements. The resistivity shows a strong increase at 308 K, which has to be attributed, as in other half-doped manganites, to the charge and orbital ordering.

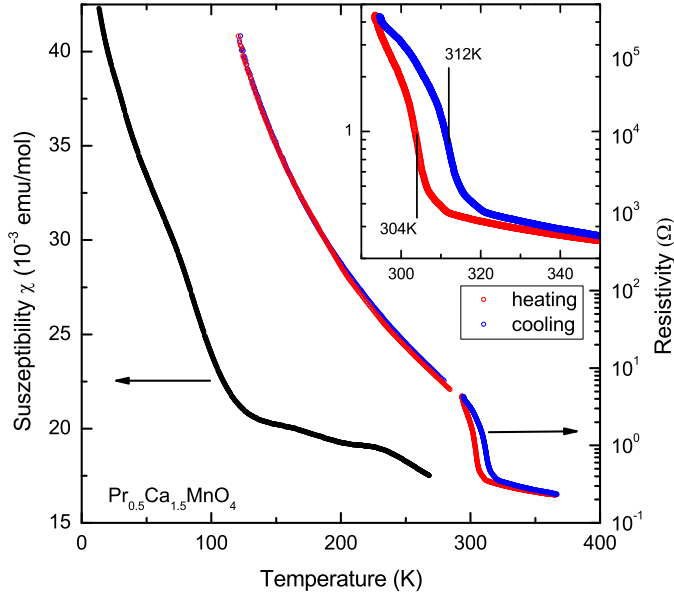


Figure 3.20: Temperature dependence of susceptibility and resistivity of $\text{Pr}_{0.5}\text{Ca}_{1.5}\text{MnO}_4$ measured both within the **ab**-plane. Susceptibility was measured in zero field cooled mode at a magnetic field of $B=0.1$ T. The deviation of the resistivity curves upon heating and cooling is most probable due to the thermal inertia of the furnace near room temperature. The inset shows the charge order transition in more detail.

Compared to $\text{La}_{0.5}\text{Sr}_{1.5}\text{MnO}_4$ the charge order transition occurs at a much higher temperature, which points to a more robust order in the (Pr,Ca) compound. The magnetization shows a transition at roughly 130 K, which is comparable to the Néel temperature $T_N=110$ K of $\text{La}_{0.5}\text{Sr}_{1.5}\text{MnO}_4$.

Figure 3.21 shows the results of an elastic neutron scattering experiment on the IN3 spectrometer. The IN3 is a triple axis spectrometer located on a thermal guide in the guidehall of the ILL reactor, Grenoble. As the IN12, this instrument has been used exclusively for elastic measurements, where the additional analyzer greatly suppresses the background which allows to observe weak signals. With this spectrometer the temperature dependence of several superstructure peaks was observed. One challenging detail in the experiment was the strong temperature dependence of the orthorhombic splitting. The centering of the crystal had to be adjusted after each temperature change and due to the twinning a perfect centering is principally not achievable for all reflections.

The two left panels show the $(2.25\ 0.25\ 0)$ reflection scanned in $(1\ 1\ 0)$ and $(1\ \bar{1}\ 0)$ direction as depicted in the inset. Three different components are visible which show a distinct temperature dependence. Those marked with a green point strongly decrease as the temperature is risen and disappears at roughly 150 K while that marked with a red circle show only a weak temperature dependence. The component disappearing at 150 K is certainly not of magnetic origin because the magnetic form factor has totally vanished at this large wave vector. It rather originates from different twin domains that yield well separated reflections because $\text{Pr}_{0.5}\text{Ca}_{1.5}\text{MnO}_4$ exhibits a large orthorhombic splitting of the in-plane lattice constants already in the high-temperature phase opposed to $\text{La}_{0.5}\text{Sr}_{1.5}\text{MnO}_4$, where the in-plane lattice constants are of equal size and thus reflections of different twin domains always perfectly overlap. The different temperature dependencies of the observed intensities are an artefact of the overlap of the individual twin com-

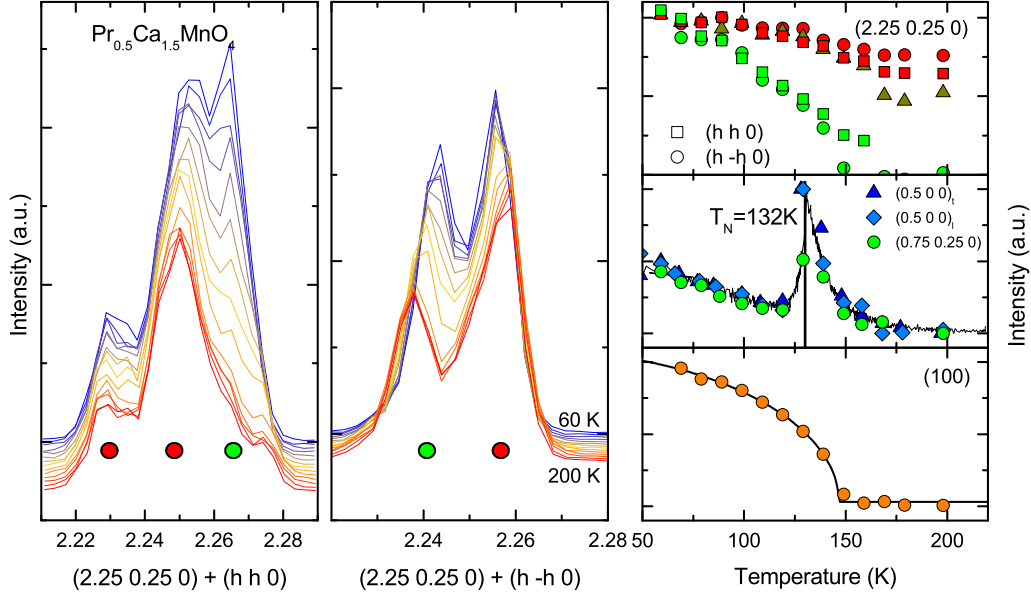


Figure 3.21: left) Superstructure peak at $Q=(2.25\ 0.25\ 0)$ scanned in $(1\ 1\ 0)$ and $(0\ \bar{1}\ 0)$ direction. Contributions from different domains are observable. The inset shows the scan path in the reciprocal space. **right)** Intensity temperature dependence for various superstructure peaks. In the upper panel, the intensity of the two distinct components observed at $Q=(2.25\ 0.25\ 0)$ is displayed. The middle panel shows the temperature dependence of the signals at $(0.5\ 0\ 0)$ and $(0.75\ 0.25\ 0)$, due to the antiferromagnetic order of Mn^{4+} and Mn^{3+} respectively. The solid line was obtained by counting on the $(0.75\ 0.25\ 0)$ position during heating. The lower panel shows the (100) peak. This diminishes at roughly 146 K and is presumably due to a structural transition to the *Pccn* group. **Note:** All reciprocal lattice vectors are given in terms of the tetragonal $3.8 \times 3.8 \times 11.8$ cell. The signals were corrected for $\lambda/2$ -contaminations where applicable.

ponents with the resolution ellipsoid. Due to the orthorhombic splitting, these components are separated in the reciprocal space and are only partially hit by the scan path. With changing orthorhombicity the separation varies and the overlap with the resolution ellipsoid decreases, resulting in an apparently different temperature dependence.

On the right of figure 3.21, the intensities derived from gaussian fits to the individual peaks are shown as function of temperature. In the top panel, the evolution of the intensities from the $(2.25\ 0.25\ 0)$ reflection, also displayed in the two left panels, is shown. The component marked with the green circle decreases rather quickly and vanishes at roughly 150 K, while the component marked with the red circle diminishes only slowly. As described above, this can be explained by the incomplete overlap of some twin reflections with the resolution ellipsoid.

The middle panel shows the temperature dependence of two magnetic peaks, the $(0.5\ 0\ 0)$ scanned in transverse and longitudinal direction and the $(0.75\ 0.25\ 0)$ scanned in $(1\ 1\ 0)$ direction. Additionally the count rate recorded at the $(0.75\ 0.25\ 0)$ peak position during heating is given. These peaks start to rise

and at approximately 132 K abruptly drop to about 20% of their maximal intensity from which they only partially recover. The strong decrease of the intensity at can be explained by an initial two-dimensional magnetic order at high temperatures which is transformed to a three-dimensional one at $T_N=132$ K. In this case, scattering at higher temperatures originates from lattice rods extending in the l -direction and not from reciprocal lattice points. Upon further temperature decrease these rods transform to sharp lattice points with a half-indexed l -component, e. g. (0.75 0.25 0.5), which explains the strong and sudden decrease in magnetic intensity. While a magnetic peak at the position (0.75 0.25 0) was already observed in $\text{La}_{0.5}\text{Sr}_{1.5}\text{MnO}_4$ see [59, 73] and section 3.2.4, the observed shape is unique to $\text{Pr}_{0.5}\text{Ca}_{1.5}\text{MnO}_4$.

Also noteworthy is the (1 0 0) peak from the lower panel. This peak is unique to the (Pr,Ca)-compound, as it is not present in $\text{La}_{0.5}\text{Sr}_{1.5}\text{MnO}_4$ at low temperatures. In the latter, it shows up as a broad feature, well *above* the Néel-transition and even above the charge and orbital ordering. Upon cooling, spectral weight is shifted to the (0.75 0.25 0) position, but until the Néel-temperature, the whole signal stays broad and shows a distinct asymmetry. See [67] pp. 66 et sqq. for a detailed discussion. This situation is different in $\text{Pr}_{0.5}\text{Ca}_{1.5}\text{MnO}_4$. Above 160 K, no signal is observed at the (1 0 0) and (0.75 0.25 0) positions. Upon a decrease of the temperature, both signals appear with a sharp shape and show no asymmetry. Thus the (1 0 0) signal must have a different origin as the one in $\text{La}_{0.5}\text{Sr}_{1.5}\text{MnO}_4$. Moreover it does not show the 2D to 3D transition as seen in the magnetic peaks (0.75 0.25 0) and (0.5 0 0) and it does not fit to the magnetic order proposed for a charge and orbitally ordered layered manganite. Thus a magnetic origin of the signal is unlikely, suggesting a structural transition as its source. The decrease of the orthorhombicity in the same temperature region together with a comparison with the cuprates [74–77] suggest a transition from a LTO to a LTLO phase, with space groups $Bmcb$ and $Pccn$, respectively. In both of these groups, the Miller indices transform to (1 1 0) and the reflection is extinct in $Bmcb$ but allowed in $Pccn$. Note, that an additional charge order transition is present below 308 K, i. e. above the LTO to LTLO transition. Thus the actual space group is the superposition of $Bmcb$ and $Pccn$ with the charge modulation.

To summarize, the data show the following picture:

- $\text{Pr}_{0.5}\text{Ca}_{1.5}\text{MnO}_4$ possess a tetragonal high-temperature structure above 467 K and is orthorhombic below.
- At 308 K, lattice distortion and resistivity indicate a charge and orbital order transition.
- The reduction of the orthorhombicity and the occurrence of a signal in elastic neutron scattering at (1 0 0) below 170 K point to a structural transition in this temperature regime. The comparison with the situation in the cuprates vote for $Bmcb$ and $Pccn$ as the respective space groups.

Mn	(0,0,0)		O _{apex}	(0,0,z)	
	U ₁₁ =U ₂₂	0.00482(10)		z	0.16608(17)
	U ₃₃	0.00780(17)		U ₁₁ =U ₂₂	0.0387(8)
				U ₃₃	0.0059(6)
Pr/Ca	(0,0,z)		O _{basal}	(1/2,0,0)	
	z	0.357445(18)		U ₁₁	0.0079(7)
	U ₁₁ =U ₂₂	0.01014(8)		U ₂₂	0.0140(8)
	U ₃₃	0.00587(11)		U ₃₃	0.0329(10)

Table 3.6: Results of refinement of the 350 K measurement of $\text{Pr}_{0.5}\text{Ca}_{1.5}\text{MnO}_4$ to the (inappropriate) space group $I4/mmm$.

- The magnetic order shows a transformation from a preceding two dimensional order to a three dimensional one as seen in the peak shapes of (0.75 0.25 0) and (0.5 0 0).

3.4.2 High temperature structure

In order to determine the charge ordered structure at lower temperatures, an understanding of the high-temperature structure, from which the charge-ordering emerges, is essential. To determine the crystal structure, x-ray single-crystal diffraction on the Bruker X8 Apex at an elevated temperature of 350 K, i. e. well above the charge ordering but in the orthorhombic phase, has been performed. No evidence for a different cell than the $5.40 \times 5.39 \times 11.9 \text{ \AA}^3$ determined by powder diffraction can be found, especially no doubling in **c**-direction. A total of 9301 reflections was collected, which can be averaged in the mmm Laue class to 1577 symmetrically independent reflections. From these 1577 reflections, 813 were larger than 3σ .

As a first evaluation, the data were further reduced according to the $I4/mmm$ space group, which describes the single-layered principal structure. Table 3.6 shows the result of this refinement. While the temperature dependent powder diffraction definitely rules out the $I4/mmm$ tetragonal symmetry, nevertheless some important knowledge can be extracted from the thermal parameters. On the one hand, U₁₁ is 1.7 and 6.6 times larger than U₃₃ for praseodymium/calcium and the apical oxygen, respectively. On the other hand, the U₃₃ parameter of the basal oxygen is extraordinarily high. This points to a tilt of the MnO₆ octahedron around an in-plane axis, which would move the basal oxygen out of the basal plane and both the apical oxygen and praseodymium/calcium away from the **c**-axis and thereby having the observed effect on the thermal parameters.

The study of the group-subgroup relations from figure 3.22 restricts the possible space groups to $Bmcb$, $Pbca$ or $P2_1/c$. The space group $Acam$ does only include

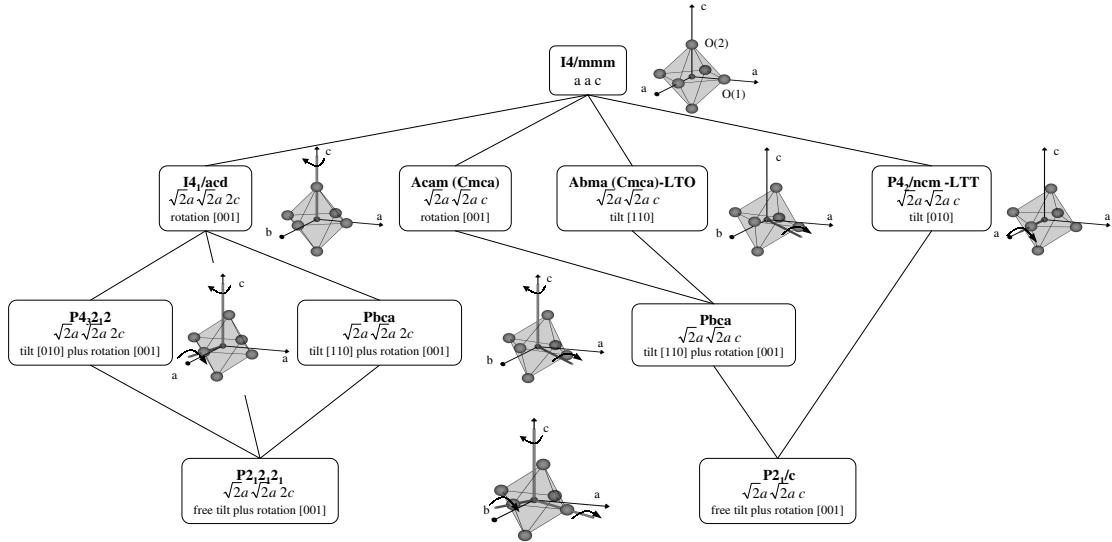


Figure 3.22: Schematic diagram of the possible space groups for single-layered perovskites taken from [78]. For each space group, the cell parameters in terms of the undistorted $I4/mmm$ structure and the distortion type are given. The term “rotation” denotes a rotation around the c -axis while “tilt” one around an in-plane axis, the lattice directions are given with respect to the $I4/mmm$ structure. Lines represent group-subgroup relations. Note that the $Abma$ space group contains an e double glide-plane and is conventionally written as $Cmce$ (no. 64 in [79], see p. 6). Here, we use the setting where $a < b < c$ holds, this results in the nomenclature $Bmcb$.

a rotation, no tilt, while $P4_2/ncm$ is tetragonal and thus not compatible with the lattice. The knowledge of the orthorhombic lattice is crucial in this case, as the latter group is one of the best results when searching for possible space groups bases on systematic extinctions. This is caused by the twinning of the crystal, which resembles a four-fold rotation symmetry resulting in a diffraction pattern which appears to be tetragonal.

A refinement of the data was performed in the two inappropriate tetragonal space groups $I4/mmm$ and $P4_1/ncm$, the orthorhombic group $Bmcb$ and the subgroups of $Bmcb$ down to $P2_1/c$. The transition from $I4/mmm$ to $Bmcb$ consists of a tilt of the MnO_6 octahedron around the $[100]_o$ axis, all basal oxygens are displaced the same absolute distance in c -direction, two neighboring up, the other two down, while the in-plane position is not changed. The apical oxygen and the cations move in the y -direction.

The subgroups of $Bmcb$ are

- $Pccn$ The tilt occurs around an arbitrary in-plane axis. The basal oxygens are still fixed at their quarter x and y positions but the z -components of neighboring ones are different while those along a diagonal still exhibit a shift of the same magnitude. This is the space group of the LTLO phase observed in the cuprates.

	$R_{w,\text{all}}$	GoF_{all}	N_{all}	$N_{>3\sigma}$	$R_{w,\text{full}}$
$I4/mmm$	3.13	3.76	242	240	23.43
$P4_2/ncm$	3.71	2.79	775	478	8.19
$Bmcb$	3.72	2.15	1050	808	8.03
$Pcab$	4.02	1.99	1451	811	8.04
$Pccn$	3.95	2.02	1355	811	8.03
$Pmcb$	4.13	1.97	1550	812	8.01
$Pman$	4.15	1.98	1533	813	8.03
$P2_1/c$	5.02	1.52	3859	1924	7.91

Table 3.7: Results of the refinement of the high-temperature data ($T=350\text{ K}$) to different space groups. $R_{w,\text{all}}$ and GoF_{all} have been calculated by JANA2000, the number of reflections N_{all} and $N_{>3\sigma}$ are the merged ones, which were compatible with the respective space group. The $R_{w,\text{full}}$ on the other hand has been calculated from all reflections without averaging in order to overcome the bias of $R_{w,\text{all}}$ due to the averaging process.

- $Pmcb$ The basal oxygens share the same absolute value for the z-displacement like in the $Bmcb$ space group. Additionally they can be displaced in the xy-plane in a way, that the octahedron edges stay parallel to the cell axes. This resembles a breathing mode type of distortion and therefore may show charge ordering.
- $Pman$ The atoms in the layers at $z=0$ and $z=1/2$ are not connected by a symmetry operation and are thus completely inequivalent. The tilt axis is $[100]$ like in the case of $Bmcb$.
- $Pcab \equiv Pbca$ Tilt pattern as in $Bmcb$ superimposed by a rotation around $[001]$. Only one inequivalent basal oxygen position exists (All other positions are determined by the symmetry elements).
- $P2_1/c$ Tilt around an arbitrary in-plane axis superimposed by a rotation around $[001]$. Two inequivalent basal oxygen positions exist.

Table 3.7 shows the results of refinements in all these space groups. Given are the weighted R-factor over all reflections, the Goodness of Fit, the number of averaged reflections without systematic extinctions and the fraction of reflections greater 3σ from JANA2000. The import and averaging steps introduce a strong bias to the agreement factors, as the averaging process is obviously different for tetragonal, orthorhombic and monoclinic space groups and JANA2000 only considers reflections, which are compatible with the systematic extinctions for the calculation of the agreement factors. This is most eminent for the $I4/mmm$ space group, where all the super-lattice reflections are omitted and the averaging step merges the more than 9000 reflections to only 242 inequivalent ones. The following fit then results in the lowest $R_{w,\text{all}}$ of all space groups although this space group is

Pr/Ca	(x,0,z)		
	x	-0.00454(13)	0.50874(13)
	y	0.00106(61)	0.49921(62)
	z	0.357379(84)	0.357463(86)
	Δ_{Bmcb} (Å)	0.0057(33)	0.0043(34)
	$\Delta_{1,2}$ (Å)	0.023(32)	
O _{apex}	(x,0,z)		
	x	0.03662(83)	0.47974(81)
	y	-0.0001(28)	0.4992(28)
	z	0.16628(42)	0.16584(47)
	Δ_{Bmcb} (Å)	0.0005(151)	0.0043(151)
	$\Delta_{1,2}$ (Å)	0.088(46)	
O _{basal}	(1/2,1/2,z)		
	x	0.2505(85)	0.2506(81)
	y	0.2511(71)	0.7488(67)
	z	-0.00865(65)	-0.00940(49)
	Δ_{Bmcb} (Å)	0.0065(397)	0.0072(378)
	$\Delta_{1,2}$ (Å)	0.0089(915)	

Table 3.8: Refined positions and of the high-temperature data (T=350 K) for the $P2_1/c$ space group. Two inequivalent positions exist for each type of atoms. The ideal $Bmcb$ position of the first one is given by the symbol next to the atom type. The difference to the ideal $Bmcb$ position is denoted by Δ_{Bmcb} , the summed distance to the mean $Bmcb$ position is given by $\Delta_{1,2}$.

definitely not feasible. Thus a R_w factor has been calculated for each space group from all reflections without averaging, including extinct ones and is given in the table as $R_{w,\text{full}}$. In the case of an extinct reflection, the calculated form factor has been set to $F_c=0$.

$$R_{w,\text{full}} = \frac{\sum_i \frac{1}{\sigma_i^2} \cdot (F_{c,i}^2 - I_{o,i})^2}{\sum_i \frac{1}{\sigma_i^2} \cdot I_{o,i}^2} \quad (3.1)$$

The R_w is much worse, because it accounts for all reflections, even those which are systematically extinct and thus were not incorporated in the refinement process. Additionally, the reflections are not merged, which also increases its value.

The $I4/mmm$ space group now shows a R-value of 23.4% and is by far the worst one. Also the tetragonal $P4_2/nm$ space group is significantly poorer than the orthorhombic ones. From the remaining space groups, the most constrained one, $Bmcb$ shows essentially the same value, as $Pcab$, $Pccn$, $Pmcb$ and $Pman$

which rules out the latter four as they give no improvement despite having more free parameters.

The space group $P2_1/c^\dagger$ indeed yields a better $R_{w,\text{full}}$, but a careful examination of the refined positions shows no significant displacement which would justify the severe reduction of symmetry, see table 3.8. Thus the increase in the agreement factors is most probable due to minor variations in the many additional parameters.

In summary, the symmetry of the high-temperature orthorhombic phase can be revealed. This phase is defined by tilted octahedra around the $[100]_o$ axis and no indication of a further rotation around the c -axis is observed. Because of the twinning, an assignment whether the tilt-axis is parallel to either the long or the short in-plane axis can not be made from the diffraction data. The resolution of the calculated precession maps is fixed by the evaluation software to 512×512 pixels, regardless of the coverage of the reciprocal space. The difference of the spot positions for the two scenarios is therefore at most less than one pixel and depends only on the orthorhombic splitting and not on the maximal extent of the map in the reciprocal space. That accuracy does not allow to reliably measure the length of a superstructure reflection.

The literature data, summarized at the end of table 3.9, strongly suggests, that the tilt axis is along the shorter in-plane lattice constant and consequently the space group is $Bmcb$. This result is supported by a report on the structure of the related compound $\text{Eu}_{0.5}\text{Ca}_{1.5}\text{MnO}_4$, where Okuyama *et al.* found the same space group [83]. On the other hand, the possibility of the larger in-plane lattice constant being the rotation axis can not definitively ruled out from the data. In this case the space group would read as $Aema$.¹⁶

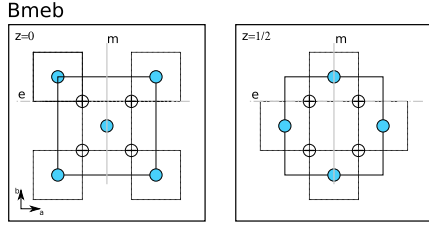
The complete results of the refinement are presented in table 3.9. The averaged tilt angle of O_{apex} and O_{basal} results as $4.51(0.03)^\circ$ which is comparable to e. g. 3.7° for La_2CuO_4 or 5.9° for LaSrScO_4 . The small differences between the tilts obtained from basal and apical oxygen atoms are negligible, e. g. LaSrScO_4 shows a much larger deviation with $\phi_b=4.2^\circ$ and $\phi_a=7.6^\circ$.

3.4.3 Charge and Orbital ordered Phase

To determine the charge ordered structure, a room temperature neutron diffraction was performed at the Heidi diffractometer, FRM2 and additionally x-ray diffraction experiments were conducted at room temperature, 160 K and 100 K. The analysis of diffraction data has been focused on four different space groups. The fundamental question is, whether the charge and orbital order or the Zener polaron order is realized in the compound. Both orders will double the cell but it is not clear ab initio if this doubling occurs in direction or perpendicular to the tilt axis of the $Bmcb$ principal structure. This results the four space groups

[†]The group with the most degrees of freedom.

¹⁶or the lattice constants are not strictly ordered $b < a < c$ and the space group stays $Bmcb$

Space Group	<i>Bmcb</i>			
<i>a</i>	(Å)	5.3833(21)		
<i>b</i>	(Å)	5.4054(26)		
<i>c</i>	(Å)	11.8422(68)		
ϕ_{basal}	(°)	4.46(5)		
ϕ_{apical}	(°)	4.55(4)		

<u>Mn</u>	(0,0,0)		<u>O_{apex}</u>	(0,y,z)
	U ₁₁	0.00483(6)		y
	U ₂₂	0.00483(6)		z
	U ₃₃	0.00779(10)		U ₁₁
				U ₂₂
				U ₃₃
<u>Pr/Ca</u>	(0,y,z)			
	y	0.006803(30)	<u>O_{basal}</u>	(1/4,1/4,z)
	z	0.357456(11)		z
	U ₁₁	0.00947(5)		U ₁₁
	U ₂₂	0.00947(5)		U ₂₂
	U ₃₃	0.00586(7)		U ₃₃
				U ₁₂

Table 3.9: Crystal structure of the $\text{Pr}_{0.5}\text{Ca}_{1.5}\text{MnO}_4$ high temperature orthorhombic phase at $T=350$ K. Lattice constants are taken from the x-ray powder diffraction experiment as the integration of the single crystal diffraction images yield the same value for the *a* and *b* lattice constant. Furthermore the twinning prohibits a distinction from the single crystal data whether the tilting occurs around the short or long axis or equivalent, if the lattice A-centered (*Aema*) or B-centered (*Bmcb*), assuming that $a < b < c$. In order to assign a space group, the ICSD-database was checked for structures of the same type. In the vast majority of cases, the tilt axis was the shorter one, i. e. the cell is B-centered, like in the prototype structure La_2CuO_4 [76], but also in LnSrScO_4 with (Ln=La, Ce, Pr, Nd and Sm) [80], Sr_2SnO_4 [81] or PrCaCrO_4 [82].

The figure on the top-right sketches the symmetry of the *Bmcb* space group. The basal planes at $z=0$ and $z=1/2$ are shown. Blue symbols mark manganese, the open symbols basal oxygen positions. Oxygen displacement in positive *c*-direction are marked with a plus sign, those in negative *c*-direction with a minus sign. The *b* glide plane is situated at $z=1/4$ and $3/4$.

Pnma (CO/OO, cell doubling perpendicular to the tilt axis), *B2/b* (CO/OO, cell doubling parallel to the tilt axis), *Bbe2* (Zener, cell doubling perpendicular to the tilt axis) and *Pnca* (Zener, cell doubling parallel to the tilt axis), see the sketch in figure 3.23. Like in the discussion of the charge and orbital order in $\text{La}_{0.5}\text{Sr}_{1.5}\text{MnO}_4$ space groups where zig-zag chains cross upon projection on the *ab*-plane could be considered. But as these types of structure yield worse results

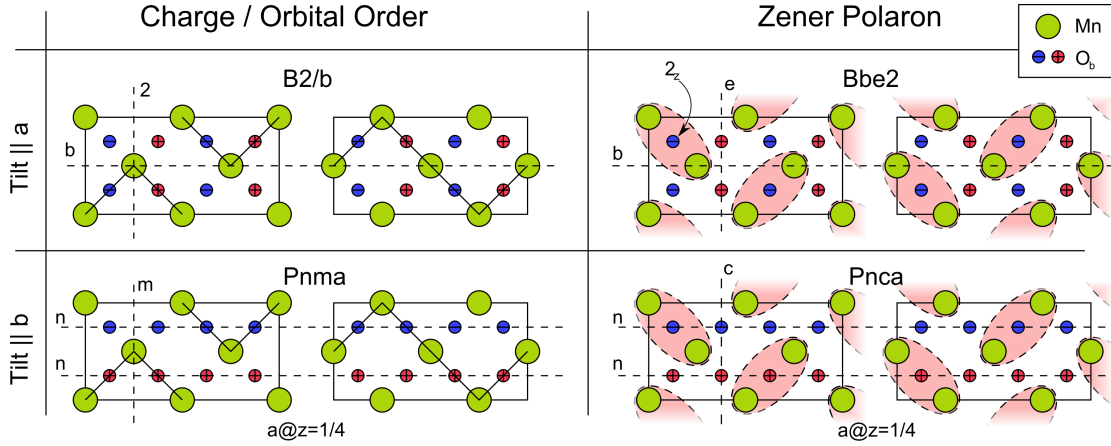


Figure 3.23: Possible atom arrangements and corresponding space groups for the charge ordered phase of $\text{Pr}_{0.5}\text{Ca}_{1.5}\text{MnO}_4$. Shown are the basal planes at $z=0$ and $z=1/2$ for possible structures for the charge/orbital and the Zener polaron order and cell doubling parallel or perpendicular to the tilt axis. Only structures, where the zig-zag chains in adjacent layers do not cross upon projection are considered. Large green circles specify manganese ions, blue and red ones oxygen ions below and above the basal plane, respectively. For the charge/orbital order the zig-zag chains and for the Zener polaron order the dimers are depicted. Generating symmetry elements are indicated by dashed lines.

in the $\text{La}_{0.5}\text{Sr}_{1.5}\text{MnO}_4$ case and are crystallographic counterintuitive no effort was put in this direction. Moreover, only the $Bmcb$ was considered as principal structure, despite the evidence for a further structural phase transition at 170 K that resembles the LTO to LTLO ($Bmcb$ to $Pccn$) phase transition of the cuprates. If one takes $Pccn$ as the host structure, the superposition with the charge order pattern yield very low symmetry space groups, e. g. $Pnma$ would transform to $P2_1/n$ with 39 position parameters instead of 19. The already challenging refinement would be nearly impossible with these degrees of freedom.

The four diffraction datasets have been fitted to the four accounted space groups resulting in total sixteen structure refinements. Like in the high-temperature structure case a different number of reflections are compatible with each space group. Table 3.10 exemplifies the fact for the x-ray diffraction measurement at 160 K. Presented are the number of reflections violating the extinction laws, the maximal and mean value of I/σ for these reflections and the agreement factors $R_{w,all}$, GoF_{all} and $R_{w,full}$. While the first two are calculated by JANA2000 from the averaged set of reflections compatible with the extinction laws, $R_{w,full}$ is instead calculated from all measured reflections, without an averaging step and including those reflections violating the extinction laws. If only the agreement factors provided by JANA2000 would be taken into account the most probable space group is $Bbe2$. But 1078 reflections with an intensity larger then 3σ are not compatible with the space group. The largest violation is from the non B-centered ($2\bar{8}5$) reflection with $I/\sigma=21.7$. The $R_{w,full}$ agreement factor on the other hand

SG	$N > 3\sigma$	N_{total}	I/σ_{max}	I/σ_{mean}	$R_{w,\text{all}}$	GoF_{all}	$R_{w,\text{full}}$
<i>B2/b</i>	1049	30222	21.7	0.20	9.61	1.82	19.13
<i>Pnma</i>	24	2979	5.3	-0.09	9.21	1.99	17.99
<i>Bbe2</i>	1078	31075	21.7	0.20	7.63	1.68	19.05
<i>Pnca</i>	197	4536	15.6	0.16	11.42	2.55	25.87

Table 3.10: Systematic extinctions and agreement factors for the x-ray diffraction measurement at 160 K. Shown for each space group are the number N_{total} of all reflections incompatible with the space group and with an intensity larger than 3σ ($N > 3\sigma$), respectively; The maximal (I/σ_{max}) and mean (I/σ_{mean}) value of the I/σ ratios of reflections incompatible with the space group and the agreement factors $R_{w,\text{all}}$, GoF_{all} and $R_{w,\text{full}}$.

votes for the *Pnma* space group which indeed possess the lowest number of reflections violating its extinction rules as well as the lowest mean I/σ . The largest violation is due to the $(00\bar{3})$ reflection and is most probable be a $\lambda/2$ artefact.

From the crystallographic point of view, the analysis of the systematic extinctions from the 160 K x-ray measurement allow one unambiguously to assign the space group *Pnma* to the charge ordered structure of $\text{Pr}_{0.5}\text{Ca}_{1.5}\text{MnO}_4$. This corresponds to the charge and orbital order found in the $\text{La}_{0.5}\text{Sr}_{1.5}\text{MnO}_4$ compound. Furthermore, Okuyama *et al.* [83] found this space group in their analysis of $\text{Eu}_{0.5}\text{Ca}_{1.5}\text{MnO}_4$. As mentioned above, the high-temperature symmetry of this compound (*Bmeb*) is the same as for $\text{Pr}_{0.5}\text{Ca}_{1.5}\text{MnO}_4$, thus the behavior of the two compounds is consistent.¹⁷

The space group test exemplified for the 160 K x-ray measurement has been performed with the same result for all remaining experiments.¹⁸ Table 3.11 summarizes the values of $R_{w,\text{full}}$ for all measurements and space groups where the *Pnma* space group always yields the lowest value. Thus no doubt is left that this space group describes the charge ordered phase of $\text{Pr}_{0.5}\text{Ca}_{1.5}\text{MnO}_4$ which thereby represents another example of a charge and orbital ordered manganite.

The results of the refinements to the space group *Pnma* are finally presented in table 3.12. These results clearly show the superposition of the tilted high-temperature structure with the charge and orbital ordering as observed in $\text{La}_{0.5}\text{Sr}_{1.5}\text{MnO}_4$. The x components of apical oxygen and Pr/Ca ions and the z component of the basal oxygen basically resembles those of the high-temperature tilt-only phase, while e.g. the displacement of the Mn(2) ion matches very well between the related compounds.¹⁹ This shows the good qualitative agreement between $\text{La}_{0.5}\text{Sr}_{1.5}\text{MnO}_4$ and $\text{Pr}_{0.5}\text{Ca}_{1.5}\text{MnO}_4$ including its different high-temperature structure. On the quantitative side, the bond valence sum yields

¹⁷The independent observation of the same sequence of space groups in a related compound is of course no *proof* that the findings are correct but at makes them at least highly plausible.

¹⁸Because of the lower number of reflections measured the values for the neutron experiment are far less impressive, e. g. for *Bbe2* only a single violating reflection lie above the 3σ threshold.

¹⁹0.50598(8) in LSMO vs. 0.50784(9) in PCMO

	Neutrons		X-Rays	
	293 K	293 K	160 K	100 K
$B2/b$	12.93	16.07	19.13	18.33
$Pnma$	12.90	15.55	17.99	17.08
$Bbe2$	12.80	16.10	19.05	18.32
$Pnca$	12.97	24.66	25.87	26.00

Table 3.11: $R_{w,full}$ calculated for the refinements of neutron and x-ray data to the possible low temperature structures. While this agreement factor is intrinsically rather high, clearly the $Pnma$ space group describes the data best.

lower values for the charge separation albeit the precision is not very high. The charge difference in $\text{Pr}_{0.5}\text{Ca}_{1.5}\text{MnO}_4$ is 0.10(2) at 100 K and 0.357(17) at 90 K in case of $\text{La}_{0.5}\text{Sr}_{1.5}\text{MnO}_4$. This value suggest a weaker order for the Pr/Ca compound which is not implausible, as the diffraction result of Okuyama *et al.* for the $\text{Eu}_{0.5}\text{Ca}_{1.5}\text{MnO}_4$ compound yield a charge disproportion of only 0.05(2) indicating an even weaker order. The bond valences for Mn(1) and Mn(2) in this case are 3.789(11) and 3.843(14), respectively.

Summary

In this section, $\text{Pr}_{0.5}\text{Ca}_{1.5}\text{MnO}_4$ could be established as a second layered charge- and orbital-ordered manganite. Unlike the “clean” system $\text{La}_{0.5}\text{Sr}_{1.5}\text{MnO}_4$ it features a tilting of the MnO_6 octahedra and is thus an important step to link the results obtained from the layered manganites to the 3D ones.

The compound shows a structural transition at 467 K from a tetragonal phase, presumable $I4/mmm$, to the orthorhombic LTO phase, space group $Bmcb$, where the MnO_6 octahedra are rotated around the $[100]_o$ axis. Just above room temperature, at 308 K a small change in the structure and simultaneously a large rise in the resistivity is observed, which is attributed to the onset of a charge ordering. Diffraction experiments with neutron and x-ray radiation confirm the same charge- and orbital-order as seen in $\text{La}_{0.5}\text{Sr}_{1.5}\text{MnO}_4$ superimposed with the LTO pattern. The Zener-Polaron model yield worse results and could be therefore ruled out for this compound as well. The magnetic structure shows pronounced transition from a two-dimensional ordering to a three-

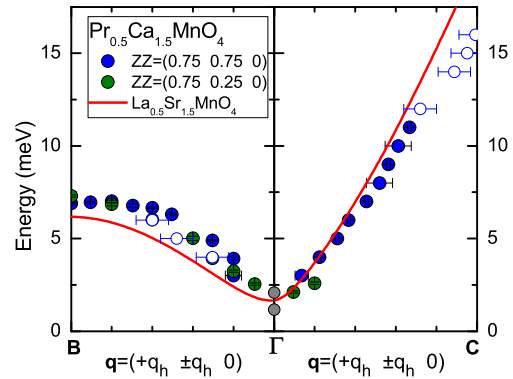


Figure 3.24: Magnon dispersion of $\text{Pr}_{0.5}\text{Ca}_{1.5}\text{MnO}_4$ measured by H. Ulbrich [84]. The solid line is a fit to the magnon dispersion of $\text{La}_{0.5}\text{Sr}_{1.5}\text{MnO}_4$ but anyhow matches the data reasonable well.

dimensional one.

In the meanwhile a similar investigation of $\text{Eu}_{0.5}\text{Ca}_{1.5}\text{MnO}_4$ was published by Okuyama *et al.* who basically found the same results as presented here for $\text{Pr}_{0.5}\text{Ca}_{1.5}\text{MnO}_4$. Especially both compounds possess the same *Bmeb* high-temperature and the same *Pnma* charge- and orbital-ordered structure. Furthermore H. Ulbrich [84] could confirm the charge- and orbital order in $\text{Pr}_{0.5}\text{Ca}_{1.5}\text{MnO}_4$ by the determination of the spin-wave dispersion shown in figure 3.24. This shows basically the same course as in $\text{La}_{0.5}\text{Sr}_{1.5}\text{MnO}_4$ and even the fit of the latter data matches the dispersion of $\text{Pr}_{0.5}\text{Ca}_{1.5}\text{MnO}_4$ reasonable well.

3.5 Conclusions

The charge ordered phase of the two half-doped layered manganites $\text{La}_{0.5}\text{Sr}_{1.5}\text{MnO}_4$ and $\text{Pr}_{0.5}\text{Ca}_{1.5}\text{MnO}_4$ has been investigated by x-ray and neutron single-crystal diffraction. The charge ordering in the lanthanum/strontium compound emerges from the highly symmetric *I4/mmm* phase with perfect aligned MnO_6 octahedra and could therefore regarded as a very pure model system. The praseodymium/calcium compound on the other side exhibits tilted octahedra and resembles to a certain extend the situation found in the three-dimensional manganites. These investigations could definitively rule out the Zener-Polaron model for the charge ordered phase. Instead the charge- and orbital-ordered model suggested by Goodenough more than fifty years ago was found.

Furthermore the effect of ruthenium co-doping in $\text{La}_{1-x}\text{Sr}_{1+x}\text{MnO}_4$ with $x=1/2$ was investigated and a strong reduction of the structural and magnetic order was found. At a ruthenium content of $y=8\%$ still some signal is found by elastic neutron scattering but magnetoresistivity measurements did not find any signature of a charge ordering at 15% ruthenium content. While the charge order is suppressed very efficiently no metallic behavior is observed up to a substitution of 30% .

		Neutrons		X-Rays	
		293 K	293 K	160 K	100 K
a	(Å)	5.3953	5.3953	5.3923	5.3915
b	(Å)	10.7906	10.7906	10.7846	10.783
c	(Å)	11.8243	11.8243	11.7992	11.7908
$N_{\text{raw,all}}$	—	1134	88270	65878	55870
$N_{\text{raw,obs}}$	—	890	16437	16354	15592
$N_{\text{avg,all}}$	—	580	7405	7478	7479
$N_{\text{avg,obs}}$	—	449	1732	2435	2637
$R_{\text{w,all}}$	(%)	4.71	7.67	9.61	9.77
GoF_{w}	(%)	3.71	2.16	2.08	2.11
BVS Mn(1)	(e)	3.50(5)	3.75(3)	3.790(11)	3.752(10)
BVS Mn(2)	(e)	3.57(3)	3.82(2)	3.803(13)	3.854(12)
Δ BVS	(e)	0.07(6)	0.07(4)	0.01(2)	0.10(2)
Mn(1)	(0, 0, 0)				
	U_{11}	0.012(3)	0.0119(3)	0.0014(3)	0.0014(3)
	U_{22}	0.011(4)	0.0027(2)	0.0112(3)	0.0102(4)
	U_{33}	0.013(2)	0.0081(3)	0.0058(3)	0.0056(3)
	U_{13}	0.002(3)	−0.0025(1)	0.0015(1)	0.00114(9)
− $O_b(1)$	(Å)	1.928(9)	1.936(3)	1.970(2)	1.977(2)
− $O_b(2)$	(Å)	1.874(9)	1.885(4)	1.868(3)	1.869(2)
− $O_a(1)$	(Å)	1.976(3)	1.966(3)	1.961(3)	1.965(3)
Mn(2)	(x, 1/4, z)				
	x	0.504(1)	0.5038(1)	0.50784(9)	0.50871(8)
	U_{11}	0.015(3)	0.0083(3)	0.0016(2)	0.0015(2)
	U_{22}	0.010(4)	0.0021(2)	0.0029(3)	0.0020(2)
	U_{33}	0.011(2)	0.0097(3)	0.0066(2)	0.0057(3)
	U_{13}	0.002(3)	−0.0016(1)	0.0020(1)	0.00150(9)
− $O_b(1)$	(Å)	1.908(9)	1.902(4)	1.881(2)	1.877(2)
− $O_b(2)$	(Å)	1.933(9)	1.923(4)	1.926(3)	1.922(2)
− $O_a(2a)$	(Å)	1.947(9)	1.979(9)	1.982(4)	1.974(3)
− $O_a(2b)$	(Å)	1.961(9)	1.982(9)	1.990(5)	1.985(3)
$O_b(1)$	(x, y, z)				
	x	0.2535(7)	0.2577(5)	0.2650(4)	0.2657(4)
	y	0.126(1)	0.1244(4)	0.1253(2)	0.1259(2)
	z	0.009(1)	0.0102(5)	0.0102(2)	0.0107(2)
	U_{11}	0.0195(4)	0.0169(7)	0.0113(4)	0.0092(4)
	U_{22}	0.0160(3)	0.0095(5)	0.0081(4)	0.0076(4)
	U_{33}	0.0214(3)	0.0178(4)	0.0121(4)	0.0128(4)
	U_{13}	−0.001(3)	0.004(1)	−0.0047(6)	−0.0032(6)

Continued on the next page

		Neutrons		X-Rays	
		293 K	293 K	160 K	100 K
$O_b(2)$	(x,y,z)				
	x	0.2405(7)	0.2459(5)	0.2406(4)	0.2401(4)
	y	-0.125(1)	-0.1236(4)	-0.1239(3)	-0.1242(3)
	z	0.010(1)	0.0100(5)	0.0120(2)	0.0123(2)
	U ₁₁	0.0195(4)	0.0169(7)	0.0113(4)	0.0092(4)
	U ₂₂	0.0160(3)	0.0095(5)	0.0081(4)	0.0076(4)
	U ₃₃	0.0214(3)	0.0178(4)	0.0121(4)	0.0128(4)
	U ₁₂	0.0032(8)	0.0038(4)	0.0032(3)	0.0024(3)
	U ₁₃	0.001(2)	0.006(1)	-0.0039(6)	-0.0023(6)
$O_a(1)$	(x,0,z)				
	x	-0.031(1)	-0.0303(3)	-0.0374(4)	-0.0362(4)
	z	0.1665(3)	0.1657(2)	0.1653(2)	0.1658(2)
	U ₁₁	0.031(3)	0.0201(7)	0.0214(8)	0.0126(7)
	U ₂₂	0.030(3)	0.023(1)	0.021(1)	0.029(1)
	U ₃₃	0.010(1)	0.0101(8)	0.0022(7)	0.0025(7)
	U ₁₃	0.001(1)	-0.0037(7)	-0.0027(8)	-0.0030(7)
$O_a(2a)$	(x,1/4,z)				
	x	0.536(3)	0.5345(6)	0.5380(5)	0.5410(4)
	z	0.164(1)	0.1668(9)	0.1674(3)	0.1667(3)
	U ₁₁	0.024(3)	0.0245(8)	0.0095(6)	0.0071(6)
	U ₂₂	0.029(3)	0.037(2)	0.031(1)	0.032(1)
	U ₃₃	0.012(1)	0.0041(7)	0.0058(7)	0.0050(7)
	U ₁₃	0.003(3)	0.000(3)	-0.001(1)	-0.0014(9)
$O_a(2b)$	(x,1/4,z)				
	x	0.476(3)	0.4709(6)	0.4727(4)	0.4710(4)
	z	-0.165(2)	-0.1669(9)	-0.1679(4)	-0.1674(4)
	U ₁₁	0.024(3)	0.0245(8)	0.0095(6)	0.0071(6)
	U ₂₂	0.029(3)	0.037(2)	0.031(1)	0.032(1)
	U ₃₃	0.012(1)	0.0041(7)	0.0058(7)	0.0050(7)
	U ₁₃	0.002(3)	-0.004(2)	-0.0037(9)	-0.0035(9)
$Pr/Ca(1)$	(x,0,z)				
	x	0.009(1)	0.00999(4)	0.00682(4)	0.00747(4)
	z	0.3572(4)	0.35751(3)	0.35747(4)	0.35752(4)
	U ₁₁	0.026(2)	0.0101(1)	0.0091(2)	0.0071(2)
	U ₂₂	0.019(3)	0.0114(2)	0.0069(1)	0.0059(1)
	U ₃₃	0.012(1)	0.0064(2)	0.0036(1)	0.0035(1)
	U ₁₃	0.004(2)	-0.00187(7)	0.00248(6)	0.00262(6)

Continued on the next page

		Neutrons		X-Rays	
		293 K	293 K	160 K	100 K
Pr/Ca(2a)	(x,1/4,z)				
	x	0.492(2)	0.49719(9)	0.49545(6)	0.49545(6)
	z	0.358(2)	0.3568(2)	0.35708(8)	0.35702(7)
	U ₁₁	0.015(2)	0.0095(2)	0.0060(1)	0.0046(1)
	U ₂₂	0.018(3)	0.0089(2)	0.0066(1)	0.0057(1)
	U ₃₃	0.011(1)	0.0073(2)	0.0051(1)	0.0044(1)
	U ₁₃	0.003(3)	-0.0027(1)	0.00129(9)	0.00153(8)
Pr/Ca(2a)	(x,1/4,z)				
	x	0.511(2)	0.50842(9)	0.51750(7)	0.51860(7)
	z	-0.358(2)	-0.3569(2)	-0.35659(7)	-0.35645(7)
	U ₁₁	0.015(2)	0.0095(2)	0.0060(1)	0.0046(1)
	U ₂₂	0.018(3)	0.0089(2)	0.0066(1)	0.0057(1)
	U ₃₃	0.011(1)	0.0073(2)	0.0051(1)	0.0044(1)
	U ₁₃	0.004(3)	0.0016(1)	0.00208(6)	0.0017(1)

Table 3.12: Structural parameters from the neutron and x-ray diffraction refinement of Pr_{0.5}Ca_{1.5}MnO₄ measured on the Heidi diffractometer, FRM2 and Bruker X8 Apex diffractometer. Measurements have been performed at room temperature, 160 K and 100 K. In addition to the atomic position and thermal displacements, the lattice constants used in the refinement, the number of measured and inequivalent reflections, split to all and $> 3\sigma$, the weighted agreement factor and the goodness of fit the Bond Valence Sums for the two manganese positions including their difference shown and the manganese-oxygen environments are shown.

4 Structural aspects of layered Ruthenates

The physics of ruthenates shows an intriguingly rich set of phenomena from superconductivity to metamagnetism and quantum-criticality. The large interest, especially in the layered representatives certainly started by the discovery of superconductivity in Sr_2RuO_4 by Maeno *et al.* [85]. It is the first and up to now exclusive superconductor which is isostructural to the cuprates but containing no copper. Opposed to the cuprates, superconductivity is limited to very low temperatures, occurring only in the pure compound and it is immediately destroyed by impurities. Furthermore, the coupling is rather unconventional, Sr_2RuO_4 is discussed to be a spin-triplet superconductor [86], which makes this compound very interesting in itself. Several ways away from the pure Sr_2RuO_4 are open, each allowing the observation of more interesting phenomena.

Among them, the more crystallographic approach of varying the number of RuO_2 layers, i. e. treating different members of the Ruddlesden-Popper series leads to $\text{Sr}_3\text{Ru}_2\text{O}_7$ [87]. This compound shows quantum-critical behavior with the magnetic field acting as the control parameter [88]. Another road to new phenomena is the partial substitution of ruthenium by e. g. rhodium, iridium or titan [89–91]. The latter stabilizes magnetic fluctuations already observed in pure Sr_2RuO_4 at finite energies resulting in a static spin density wave [92–94].

Furthermore the substitution of the strontium is clearly an obvious possibility. While some charge doping by inclusion of lanthanum was investigated [95], the most investigated doping series is clearly the substitution of strontium by the isovalent but smaller calcium [96]. Although the valence of the ruthenium ion is not changed by this procedure, a rich phase diagram is obtained. As stated above, Sr_2RuO_4 shows metallic behavior and superconductivity, Ca_2RuO_4 on the other hand is an antiferromagnetic Mott insulator. Between $x=0$ and $x=0.2$ the evolution of three distinct structural could be observed and at a doping level of $x>0.2$ a metamagnetic transition takes place [97, 98].

As the $\text{Ca}_{2-x}\text{Sr}_x\text{RuO}_4$ system turned out to be very fruitful, a similar investigation was performed on the double-layered ruthenates $(\text{Ca}_{1-x}\text{Sr}_x)_3\text{Ru}_2\text{O}_7$. Also here, large variations are observed despite the isovalent doping. While $\text{Sr}_3\text{Ru}_2\text{O}_7$ is a ferromagnetic metal showing a quantum-critical behavior as function of a magnetic field as the external control parameter, $\text{Ca}_3\text{Ru}_2\text{O}_7$ is an antiferromagnetic Mott insulator. Moreover, it shows a metal-insulator transition which takes place below the Néel temperature, in an intermediate regime the system is an antiferromagnetic metal.

This chapter will present the results obtained on two fields of activity. First the phase diagram of the system $\text{Ca}_{2-x}\text{Sr}_x\text{RuO}_4$ is extended. As an important step to this goal, various sample of $\text{Ca}_{2-x}\text{Sr}_x\text{RuO}_4$ had to be prepared, a work which is described in the first section. That is followed by a discussion of the metal-insulator transition at high calcium concentration and its coupling to the structural transition. And the examination of the onset of the rotational distortion near pure Sr_2RuO_4 . In the second part of this chapter, the nuclear and magnetic structure of $\text{Ca}_3\text{Ru}_2\text{O}_7$ will be discussed.

4.1 Transitions in $\text{Ca}_{2-x}\text{Sr}_x\text{RuO}_4$

Excellent work was already done to determine the structural phase of $\text{Ca}_{2-x}\text{Sr}_x\text{RuO}_4$ by O. Friedt and P. Steffens [99, 100]. This section is based on their works and extends it at those points where samples were not available to these authors. In the diploma thesis preceding this work the synthesis of ruthenates was started and extended in this work, which enabled further investigations of the phase diagram.

4.1.1 Sample Preparation

Poly-crystalline samples of $\text{Ca}_{2-x}\text{Sr}_x\text{RuO}_4$ have been prepared by a standard solid-state reaction similar to that used to prepare manganites samples. Opposed to them, an accurate control of the sintering parameters turned out to be crucial for single-phase results.

Stoichiometric amounts of CaCO_3 , SrCO_3 were mixed together with RuO_2 in stoichiometric and off-stoichiometric amounts, grounded in an agate mortar and finally pressed to pellets of 15 mm diameter. These were heated under a static atmosphere consisting of a mixture of argon with 1 % to 5 % of oxygen in a platinum crucible. The used furnace together with its gas handling system is described in [101]. After the heat treatment, the surface of the pellets was lighter than the inside. Thus it was carefully scraped off and X-ray diffraction of this fraction showed an increased amount of impurity phases like 113-Phase or CaO compared to the inner part. This indicates an increased ruthenium evaporation from the surface due to the high temperatures as already observed by S. Nakatsuji [102]. In order to obtain high purity samples, effort was made to find the lowest possible reaction temperature for different stoichiometries in order to reduce the evaporation to a minimum while at the same time ensure a proper formation of the desired 214 phase.

In contrast to the manganites, which very easily form phase-pure samples in a wide region of preparation parameters, 214-ruthenates only form single-phase samples with very well-defined reaction parameters. Figure 4.1 shows the effect of the sintering temperature for $\text{Ca}_{1.95}\text{Sr}_{0.05}\text{RuO}_4$ and $\text{Ca}_{1.875}\text{Sr}_{0.125}\text{RuO}_4$. A decrease of the sintering temperature of only 15 K, i. e. less than 1.1 % is sufficient

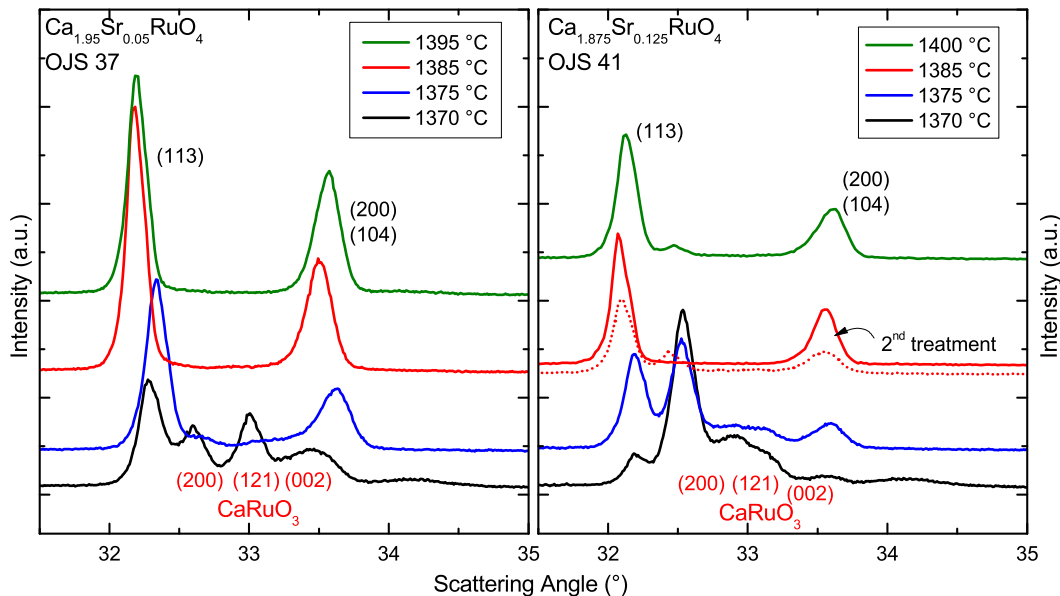


Figure 4.1: Effect of the sinter temperature on the phase purity of $\text{Ca}_{2-x}\text{Sr}_x\text{RuO}_4$ with $x=5\%$ and 12.5% . Details of the Cu K_α x-ray diffractogram at room temperature where the 214 and 113 phase both possess peaks. For $x=5\%$, the impurity phase of CaRuO_3 is clearly visible for the sample sintered at 1370°C . A rise of only 5°C in sintering temperature is sufficient to drastically suppress it, see the red curve. 15°C above, no impurity phase is present anymore. For the $x=12.5\%$ sample sintered at 1370°C , $(\text{Ca,Sr})\text{RuO}_3$ is clearly the majority phase and even present at 1400°C . It only vanishes after a second treatment with the same parameters. All samples were taken from the same master blend of corresponding stoichiometry, pressed to pellets and heated for 12 h in argon with 5% O_2 . No other parameter were changed for different samples.

to greatly increase the amount of impurity phases. As due to the increased ruthenium evaporation at higher sintering temperatures a reduction of the latter is favorable the preparation of samples intended for further measurements has been done at 1395°C . Furthermore the surface of the pellets has been scraped off and only the inner part was used for measurements.¹ Samples were prepared from several regions of the phase diagram. A large number of samples in the calcium-rich region from $x=0.0$ to $x=0.2$ was used to follow the phase-boundaries of the structural, magnetic and metal-insulator transitions. Above a strontium concentration of $x>0.20$ the system shows metamagnetic behavior. Here a sample of $x=0.22$ was already prepared in the authors diploma thesis and measured at the GEM diffractometer at the ISIS facility [103]. The extension to even higher doping levels like $x=0.25$, $x=0.30$ and $x=0.35$ was intended but despite a large effort, no single-phase sample could be obtained. The more strontium rich samples in the range from $x=1.0$ to $x=2.0$ did not show these difficulties. Sample preparation

¹A processing of the pellets intended for magnetization and resistivity measurements is clearly not feasible. These were instead sintered from prereacted powder at only 1200°C .

was possible again and four different compositions were produced to investigate the onset of the rotational distortion by high-resolution neutron diffraction.

4.1.2 L-Pbca to S-Pbca Transition

Ca_2RuO_4 shows several phase transitions as function of temperature [104]. Cooling down the sample from the high temperature regime, a first order structural phase transition is observed at 350 K. The a and b lattice constants strongly increase while the c lattice constant decreases. The space group $Pbca$ is preserved at this transition and a prefix of L- and S- for the long and short c lattice constant, respectively is used for the differentiation between these two phases. Coincidental with the structural phase transition a metal-insulator transition is observed, thus the L- $Pbca$ phase is metallic, while the S- $Pbca$ phase shows insulating behavior. At a lower temperature of 150 K, i. e. in the S- $Pbca$ phase, Ca_2RuO_4 shows antiferromagnetic order.² These three transitions occur in the whole range from $x=0$ to $x=0.2$. Friedt [78] speculates about a subtle change in the metal-insulator transition at $x=0.1$, namely the change of the coincidence with the structural phase transition to a coincidence with the magnetic one. On the other hand, Moore *et al.* [105] could show, that the surface of $\text{Ca}_{1.9}\text{Sr}_{0.1}\text{RuO}_4$ exhibits a metal-insulator transition at a lower temperature than in the bulk and relate this finding to the different structure of the surface. This would suggest a quite strong coupling between structure and the metal-insulator transition.

As outlined above, a series of closely spaced samples in the range of $x=0.01$ to $x=0.15$ has been prepared for a detailed investigation of this proposal, in particular ten samples from $x=0.01$ to $x=0.1$ with a spacing $\Delta x=0.01$ complemented by $x=0.125$ and $x=0.15$. For these samples, the temperature dependence of the lattice constants was recorded by x-ray powder diffraction, the metal-insulator transition by resistivity measurements down to liquid helium temperatures and the magnetic transition by squid-measurements. All these measurements are exemplified below for the $x=0.08$ sample.

Analysis of the X-Ray data In order to obtain reliable results for the phase fractions from the x-ray diffraction data in the region of phase coexistence a special mode of the FULLPROF program was employed. Rietveld fits gave only poor agreement between measured data and calculated model even with only a single phase. A conventional LeBail fit is not suitable for this problem, as it handles the intensities for every peak separately, thus it does not provide a scale factor from which the phase fractions could be calculated. Furthermore a large number of closely spaced peaks are allowed in the $Pbca$ space group, thus in the region of coexistence of the L- $Pbca$ and S- $Pbca$ phase, nearly every strong peak of one phase

²In fact the situation is even more complex. Below 150 K a minor contribution of a B-type antiferromagnetic order is observed while below 112 K the major A-type antiferromagnetic phase adds. In the strontium doped samples, the A-type phase is not observed anymore.

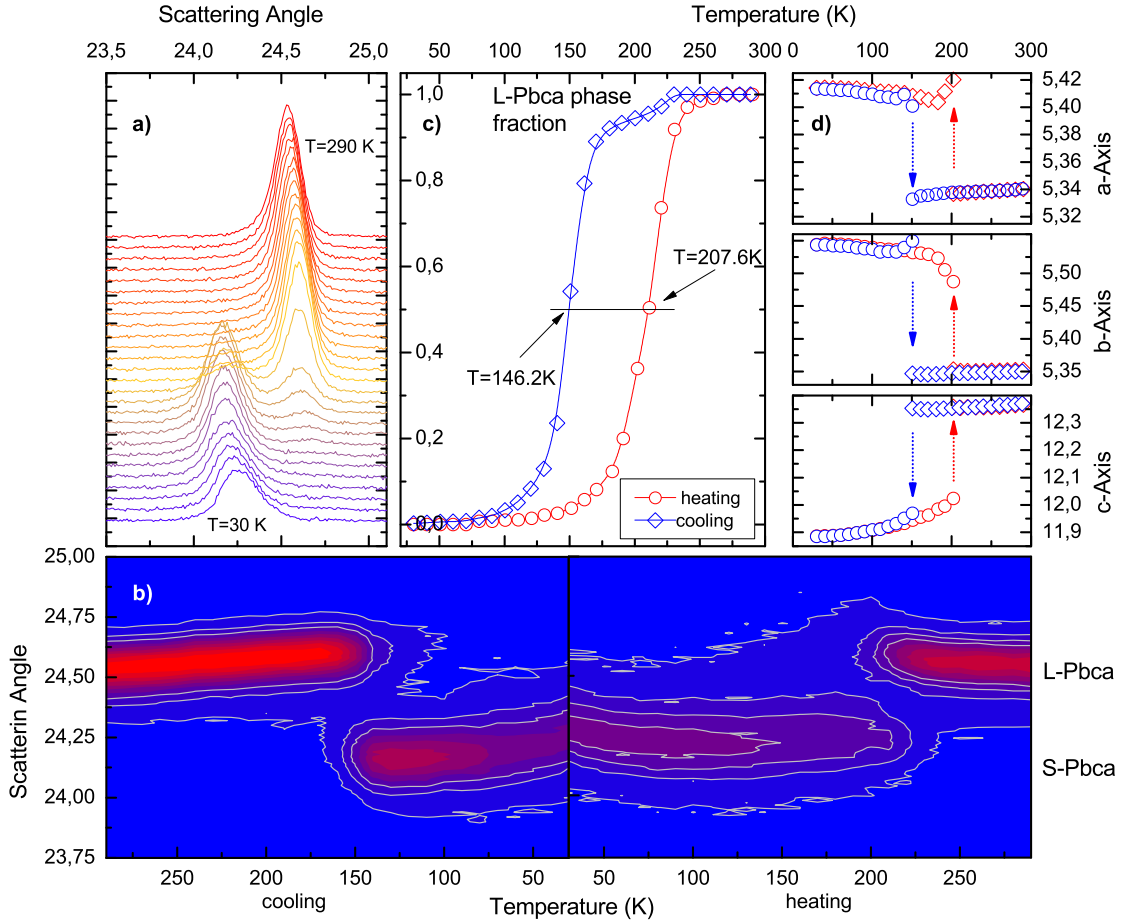


Figure 4.2: Structural transition at low doping and temperature exemplified on the $Ca_{1.92}Sr_{0.08}RuO_4$ sample. **a)** Waterfall plot of x-ray diffractograms from the (111) reflection upon cooling. Note how both structural phases are present in the intermediate region, i. e. roughly at 140 K. **b)** Contour plot of the (111) intensity. The left part shows the same data as in a) while the right part shows the data upon heating. The hysteresis is about 60 K. **c)** *L-Pbca* phase fractions derived from fits to the diffractograms. These data were used in determine the phase boundaries in the phase diagram. **d)** Lattice constants derived from the same fits. The phase transition has a large effect on all three curves.

overlaps with one from the other phase. As no structural model is used, no ab-initio information on the strength of the peaks is available and the adjustment of the intensities in the LeBail-Fit is quite fragile. This could render even the reliable determination of lattice constants impossible. To circumvent this problem, one has to constrain the relative intensities of the peaks for each phase to the expected ones. The best result was obtained by extracting the intensities of *L-Pbca* and *S-Pbca* phase conventional LeBail fits to a low- and high-temperature diffractogram, respectively. In these temperature regimes, only a single phase is present, which allows for a reliable extraction of all peak intensities. These first fits yield two

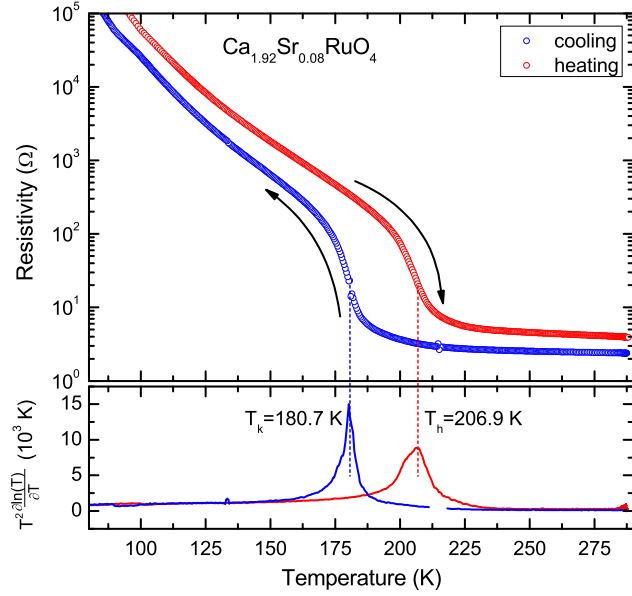


Figure 4.3: Metal insulator transition at low doping exemplified by the resistivity and its logarithmic derivative of $\text{Ca}_{1.92}\text{Sr}_{0.08}\text{RuO}_4$. The sample was cooled down to helium temperatures and warmed up afterwards. Systematic errors in the resistivity measurement were reduced by using a four terminal method and periodically reversing the current and average over one period which reduces errors due to the thermoelectrical potential. The offset between cooling and heating runs is caused by the formation of cracks in the sintered pellet.

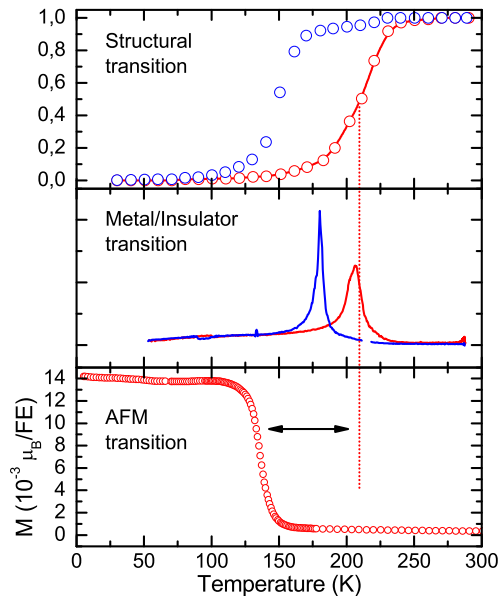
hkl-files with intensities for each reflection for both phases, which were in turn used as input for the following FULLPROF runs. Setting the IRF parameter to 4 in these runs causes FULLPROF to read the structure factors from the supplied hkl-files instead of calculating them from a structural model or adjusting them independently. Scale factors allows for varying phase fractions while the relative intensities are preserved. This procedure requires, that the relative intensities do not change too much as function of temperature, which seems to be valid as the fits describe the data in the whole temperature range very well. Because the the prototype hkl-files were determined from the high and low-temperature diffractograms of one experimental run, the the scale-factors for *L-Pbca* and *S-Pbca* phases of all diffractograms vary roughly between zero and unity. This allows to calculate the phase fraction as $\frac{S_{L-Pbca}}{S_{L-Pbca} + S_{S-Pbca}}$. For the determination of the transition temperature, this value has been fitted by an appropriate combination of an error function and an arcustangens³.

Results of the measurements Figure 4.2 shows the results of temperature dependent x-ray diffraction for the $x=0.08$ sample. Panels a) and b) show an interval of the raw diffractograms, with the (1 1 1) reflection⁴. Approaching from high temperatures, the peak shifts towards higher angles, which corresponds to a reduction of the corresponding layer distance. At about 150 K, a second peak appears at lower angles, while at the same time, the first loses in intensity. This is clearly the signature of a first order phase transition, with a region, where both phases coexist. Panel c) of figure 4.2 shows the fraction of the *L-Pbca* phase derived from

³The error-function is the normalized indefinite integral of a gaussian while the arctan is the integral of a lorentz-function. Thus, this combination gives the integral of a pseudo-voigt.

⁴Cu $K\alpha_{1,2}$ -radiation

Figure 4.4: Structural, metal/insulator and magnetic transition in $\text{Ca}_{1.92}\text{Sr}_{0.08}\text{RuO}_4$. The upper panel show the phase fraction of the *L-Pbca* phase, the mid panel the logarithmic derivation of the resistivity and the lower panel the magnetization from a SQUID measurement. The structural and metal/insulator transition were both measured upon heating and cooling while the magnetization was only measured during heating. While the first two transition coincide both in the heating and cooling curves, the antiferromagnetic transition set in 70 K below.



the FULLPROF fits measured for a full temperature cycle. The large hysteresis of ~ 60 K confirms the first order nature of the phase transition. The transition temperatures were determined from the inflection point of the fit, i. e. at $y=0.5$. Panel d) of figure 4.2 displays the temperature dependence of the lattice constants. While the *L-Pbca* phase shows a normal thermal expansion, the *S-Pbca* exhibits an anomalous behavior of the **a**- and **b**-axis. But note, that the effect due to the phase transition from *L*- to *S-Pbca* is much larger than the thermal expansion in contrast to the findings for Ca_2RuO_4 .

Figure 4.3 shows the metal-insulator transition of the same sample. These data were measured on a pressed and sintered pellet with 15 mm diameter. These pellets are rather fragile, even immediately after their preparation. The extreme stress due to the strong effect in the lattice constants during a thermal cycle weakens the pellet even more. This creates small cracks, which lead to an increase of the resistivity after the thermal cycle as could be seen from the offset between cooling and heating curves. Sometimes, the pellet even breaks during a temperature sweep, which then was repeated with a new pellet. For a more consistent determination of the metal-insulator transition temperature among the different samples, the logarithmic derivation⁵ of the resistivity was fitted by a gaussian. The logarithmic derivation, together with an indication of the transition temperature is given in the lower panel.

Figure 4.4 show all three transitions for $\text{Ca}_{1.92}\text{Sr}_{0.08}\text{RuO}_4$, namely the structural transition from *L-Pbca* to *S-Pbca*, the metal insulator transition and the antiferromagnetic transition. Obviously the structural and metal-insulator transition match very well, while the magnetic transition sets in at an about 70 K lower

⁵ If the resistivity shows an activated behavior $\rho \sim e^{\frac{E_g}{k_B T}}$, the logarithmic derivation $-T^2 \frac{\partial \ln \rho}{\partial T}$ is equivalent to the value E_g/k_B [K] of the gap.

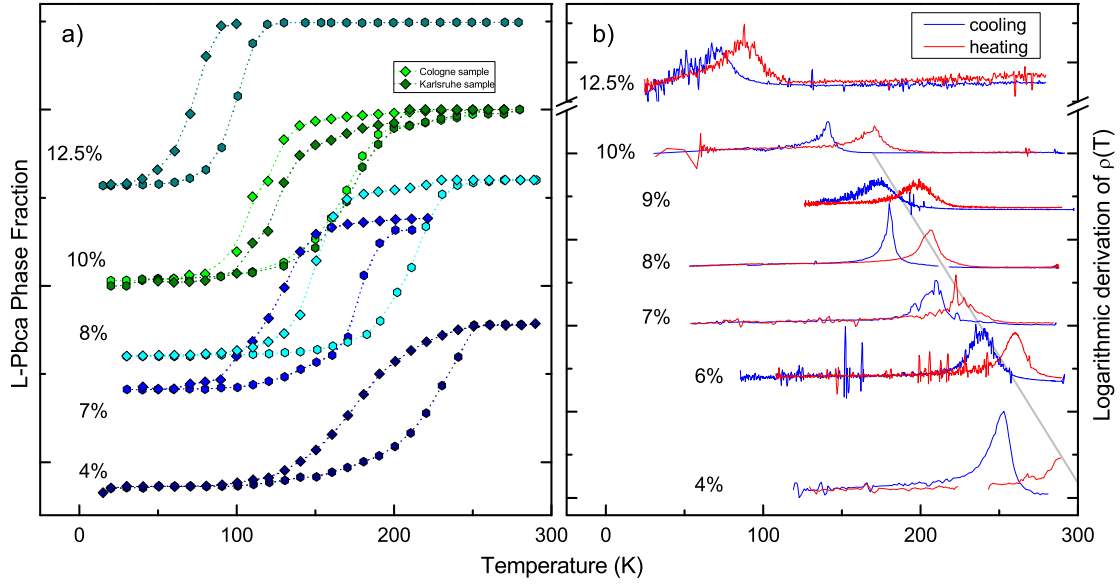


Figure 4.5: a) Fractions of the L-*Pbca* phase for different Sr concentrations determined by x-ray diffraction. Two samples with $x=10\%$ were investigated, one from P. Adelman, Karlsruhe and one which was prepared in the course of this thesis. A sample with $x=15\%$ was measured as well but did not show any indication of the structural transition down to 20 K. b) Logarithmic derivatives of the resistivity from heating and cooling runs. The metal-insulator transition manifests itself through a peak. With increasing strontium content, the transition shifts to lower temperatures.

temperature. Note that the latter transition was only recorded during heating.

In order to get detailed information on the phase boundary, the investigations described in detail above for the $x=0.08$ sample have been carried out for all available samples. Figure 4.5 displays the phase fractions indicating the structural phase transition and the logarithmic derivations of the resistivities indicating the metal-insulator transition. The curves have been shifted according to the doping level. The results of these investigations are summarized in table 4.1 and are incorporated in the revised phase diagram in section 4.1.4. These data clearly show that the metal-insulator transition is coupled with the structural transition all the time and no shift to the magnetic transition takes place.

4.1.3 Rotational Distortion

In the vicinity of pure Sr_2RuO_4 compound, another structural peculiarity is observed. For the pure Sr_2RuO_4 the $I4/mmm$ space group has been established with a very high level of confidence. X-ray and neutron diffraction measurements do not show any evidence for super-structure reflections and a rotation of the RuO_6 octahedra could be definitively ruled out from measurements of the phonon branches [107, 108] which show a slight softening of the relevant modes which stay however finite. On the other hand $\text{Ca}_{0.5}\text{Sr}_{1.5}\text{RuO}_4$ shows a rotation of the

x	Sample	T_S		T_{MI}		T_N
		cooling	heating	cooling	heating	heating
0.03	PA542	241.2 [†]	288.5 [†]	—	—	142 [‡]
0.04	OJS56	—	—	251.9	—	—
0.05	OJS37	229.7 [†]	260.5 [†]	259.3	287.2	143 [‡]
0.06	OJS38	150.4 [†]	217.8 [†]	238.6	259.7	138 [‡]
0.07	OJS39	123.5	193	208.1	223.6	—
0.08	OJS32	146.2	207.6	180.2	206.0	137
0.09	OJS40	—	—	174.2	198.8	—
0.10	OJS36	129.0	169.7	140.9	170.0	133
0.125	OJS41	71.4	89.5	69.4	90.4	—
0.15	OJS42	—	15 [°]	—	—	—

Table 4.1: Transition temperatures of low doped $\text{Ca}_{2-x}\text{Sr}_x\text{RuO}_4$. Data marked with [†] and [‡] were measured by Paul Steffens [7] and Jörg Baier [106], respectively. The structural transition temperature for the $x=0.15$ compound marked with [°] is approximated from a neutron diffraction study of Oliver Friedt [78]. The x-ray diffraction down to 20 K only shows an incomplete phase transition. The $x=0.03$ sample labelled with PA542 was prepared by P. Adelman from Karlsruhe.

octahedra with a $I4_1/acd$ symmetry and rather large rotation angle of 7.8° of the RuO_6 octahedra. In the $I4_1/acd$ space group the rotation direction of RuO_6 octahedra is reversed between RuO_2 -layers separated by 12.7 \AA which results in a doubling of the unit cell both in the **c**-direction (25.4 \AA) and in the **ab**-plane ($\sqrt{2}a \times \sqrt{2}a$).

In the region between $x=1.5$ and $x=2.0$ it was not clear, whether a first order transition with an abrupt onset of the rotation angle to a finite value or a smooth increase of the rotation angle from a critical concentration is realized. Moreover the available data did not yield a sensible answer to the question, if an extrapolation would expect Sr_2RuO_4 to be distorted or not. Thus samples with $x=1.7$ and $x=1.9$ have been prepared and measured on the high resolution neutron powder diffractometer 3T.2 at Saclay, both at room temperature and 10 K. Furthermore, the powder diffraction patterns taken by Oliver Friedt were reevaluated with exactly the same procedure in order to gain the most possible consistent picture.

The diffractograms were fitted with the FULLPROF program with the conventional Rietveld algorithm. Like in Sr_2RhO_4 [14], the rotation is not perfectly ordered, but shows stacking faults along the **c**-axis which are not extraordinary, as the involved layers are $\sim 12 \text{ \AA}$ apart. In this distance the sole movement of the oxygen ions in a collaborative way could easily be disturbed. To describe these stacking faults, the split model was used where the displaced oxygen atom is entered twice with positions corresponding to clockwise and counter-clockwise rotation. The occupation numbers of the two atoms are constrained to sum up to one. This allows to calculate the diffraction pattern of a disordered structure

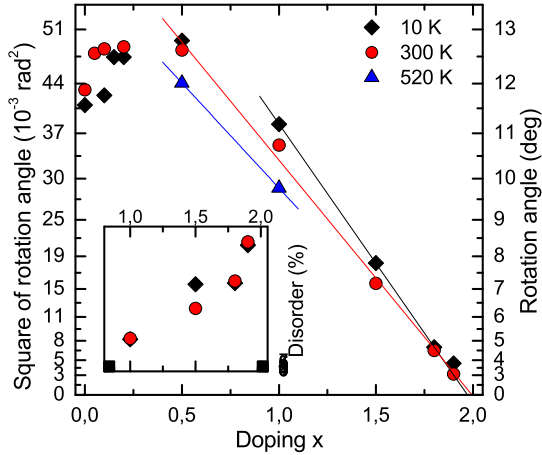


Figure 4.6: Plot of the data from table 4.2. Shown is the square of the rotation angle of the RuO_4 octahedron around the \mathbf{c} -axis for three different temperatures. For reference, the right scale indicates the non-squared rotation angle. In the inset, the split-parameter describing the disorder of the stacking in \mathbf{c} -direction is shown.

x	10K	290K	520K
0.00	11.58	11.88	
0.05		12.57	
0.10	11.77	12.65	
0.15	12.5	12.20	
0.20	12.5	12.69	
0.50	12.8	12.63	12.01
1.00	11.19	10.75	9.78
1.50	7.81	7.18	
1.80	4.69	4.53	
1.90	3.80	3.10	

Table 4.2: Rotation angles of the RuO_6 octahedron around the \mathbf{c} -axis. Most data were taken from O. Friedt [78] and P. Steffens [7] but reevaluated to yield a more consistent results.

with a Rietveld program intended to handle only perfect ordered structures. Furthermore all cases from perfect ordering (one position is fully occupied while the other is vacant) to a totally random distribution of clockwise and counterclockwise rotations (both occupancy numbers are the same) could be covered.

Figure 4.6 and table 4.2 give the results of the evaluations. The rotation angle at room temperature exhibits a maximum near the pure Ca_2RuO_4 and then decreases with increasing strontium content. Above $x=0.5$ the rotation angle decreases monotonically and vanishes at 1.99(13) as derived from a fit to the square of the rotation angle. Furthermore the disorder of the rotation increases above $x=1.0$ and reaches basically 100%, i. e. a totally random arrangement of the rotation at $x=2.0$. This could be understood as with decreasing rotation angle the energy costs for a stacking fault equally decreases and they become more likely. These findings are supported by the phonon dispersion [107] which shows a very flat dispersion along the \mathbf{c} -direction indicating almost no next-layer coupling. From these data, pure Sr_2RuO_4 is therefore predicted to show no rotational distortion while is certainly very close to one as was already confirmed before. Furthermore an abrupt onset of the rotational distortion to a finite value at a critical concentration is likewise not observed.

In summary, Sr_2RuO_4 is very close to a rotational instability but shows no sign of any rotation. A small inclusion of calcium however is sufficient to induce a rotation of the octahedra. At first this rotation is not coherently ordered but with increasing rotation angle the imperfection is more and more reduced. A

perfect, well defined and three dimensionally ordered arrangement is however not established below a calcium concentration of $x=1.0$.

4.1.4 Phase Diagram

The obtained results in the above sections were used to extend the phase diagram established earlier [7, 78, 99]. The new revised phase diagram is shown in figure 4.7. Here the phase boundaries denote the transitions observed upon heating, i. e. the larger of the two values if a hysteresis is present.

On the calcium-rich region a number of points could be added to the phase boundaries between the $Acam$ ⁶ and $L-Pbca$ phase and between the $L-Pbca$ and $S-Pbca$ phase as well as for the magnetic and the metal-insulator transition. This clearly shows the metallic behavior of the $L-Pbca$ phase while the $S-Pbca$ phase is insulating.

In the metamagnetic region $x>0.2$ the transition from the $I4_1/acd$ to the $Pbca$ phase is depicted for $x=0.2$ measured by P. Steffens, $x=0.22$ and $x=0.25$ measured in the diploma thesis preceding this work and $x=0.5$ measured by O. Friedt. The shown course of the phase boundary is a guide to the eyes and might be improved if new samples in the metamagnetic region could be synthesized.

The rotation angle as function of the doping was reevaluated and one new point could be added. The data show the disappearance of the rotation in the vicinity of Sr_2RuO_4 where both the magnitude reduces and the disorder increases.

⁶The c glide plane is in fact an e double glide plane thus the symbol should actually be written as $Aeam$

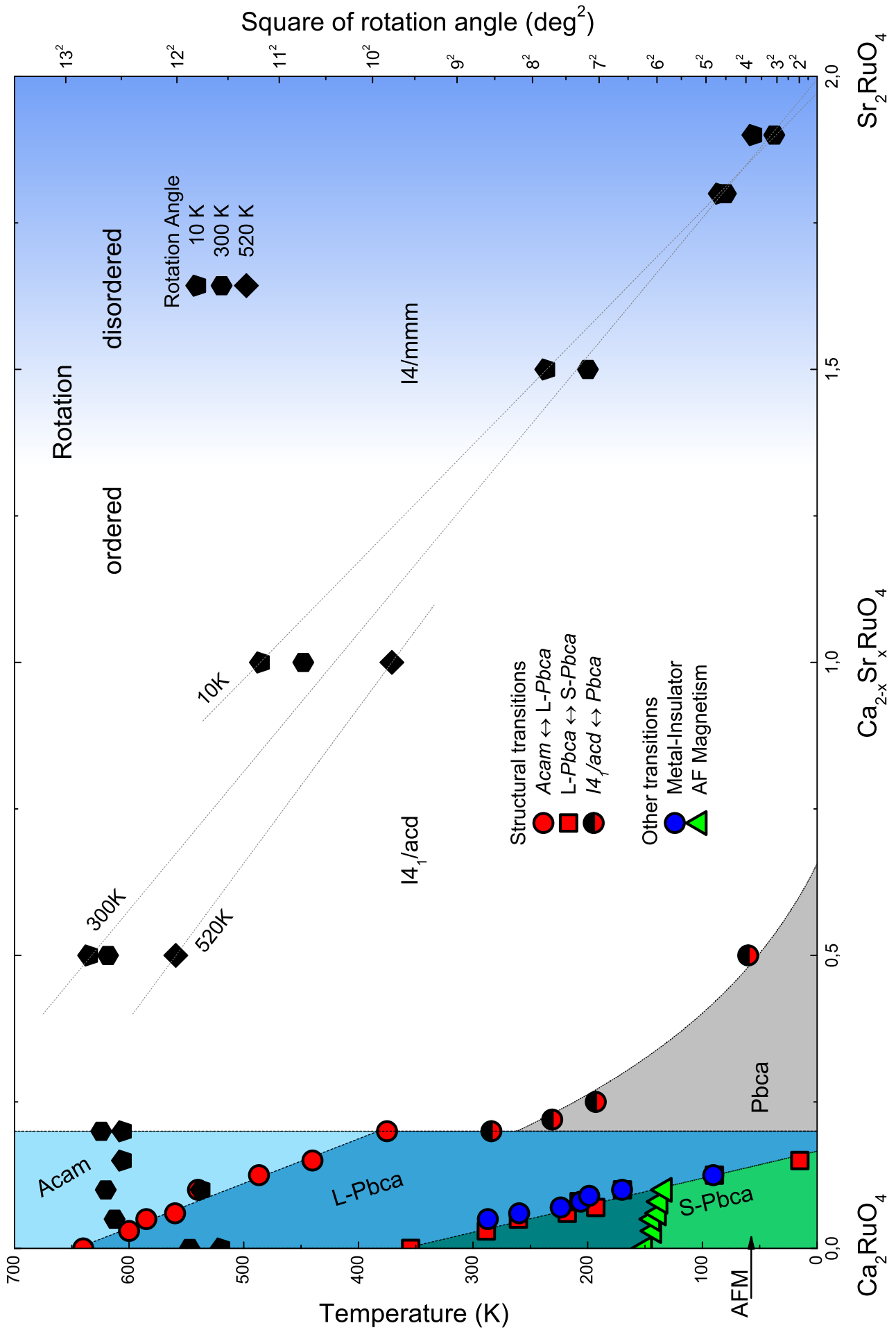


Figure 4.7: Revised phase diagram. See the text for a description.

4.2 Magnetic structure of $\text{Ca}_3\text{Ru}_2\text{O}_7$

Opposed to the previous structures of the manganites and $\text{Ca}_{2-x}\text{Sr}_x\text{RuO}_4$ which are the single layer i. e. $n=1$ representatives of the corresponding Ruddlesden-Popper series, $\text{Ca}_3\text{Ru}_2\text{O}_7$ possesses the double layer perovskite structure shown in figure 4.8. Two layers of corner shared RuO_6 octahedra are stacked and separated from the next double layer by a CaO intercalation. In the center of eight octahedra within one double layer a further calcium is situated. Ruthenium ions are shown black, calcium ions red and oxygen ions orange in the figure. This double layer structure is the first step towards a more three dimensional structure, note that the 3D perovskite structure is the $n=\infty$ end member of the Ruddlesden-Popper series. The prototype compound of this structure is $\text{Sr}_3\text{Ti}_2\text{O}_7$, actually described for the first time by Ruddlesden and Popper themselves [109]. The ideal, non-distorted structure possesses the space group $I4/mmm$ which matches that of the single layer structure. Like there, the octahedra may be rotated with a subsequent reduction of the symmetry and indeed the lattice of $\text{Ca}_3\text{Ru}_2\text{O}_7$ is not tetragonal but orthorhombic.

Basic properties of $\text{Ca}_3\text{Ru}_2\text{O}_7$

The large interest in $\text{Ca}_3\text{Ru}_2\text{O}_7$ results from the observation of two closely spaced phase transitions. At high temperatures, the system features a metallic resistivity and is not magnetically ordered (PM)⁷. Upon cooling, first an antiferromagnetic order with a Néel temperature of 56 K is observed and at a lower temperature of 48 K a metal to non-metal transition is found (AFNM), where the insulating phase is characterized by a small gap of only 0.1 eV [111]. In the intermediate region the system is an antiferromagnetic metal (AFM-b) [112]. With an increasing magnetic field both transitions move to slightly lower temperatures, the exact course and adjacent phases depend on the direction of the magnetic moment within the ab -plane. In case of an alignment along the \mathbf{a} -axis, the AFM-b phase is suppressed above roughly 3 T while the AFNM phase persists up to 6 T. Above 6 T a ferromagnetic phase (FNM) is present, which exhibits a lower resistivity than its precursor but possesses a negative temperature coefficient. As this is the fingerprint of an insulator and this

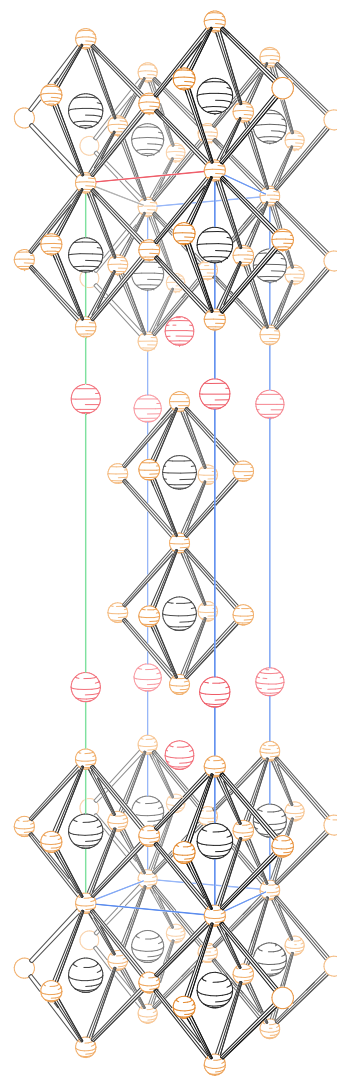


Figure 4.8: Double-layered perovskite structure.

⁷The labelling of the different phases is borrowed from McCall *et al.* [110]

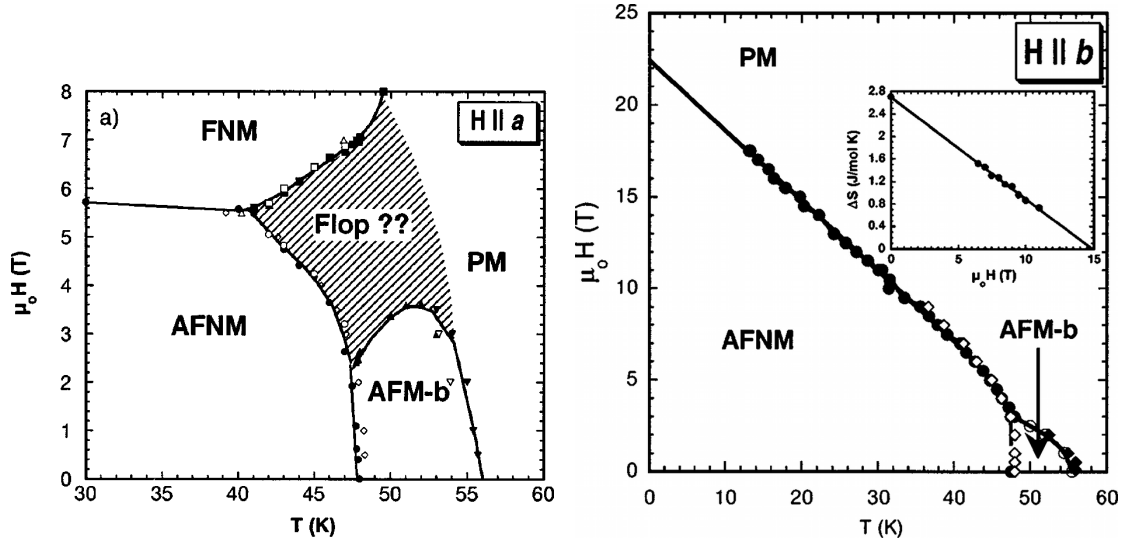


Figure 4.9: Phase diagram of $\text{Ca}_3\text{Ru}_2\text{O}_7$ from [110] for the magnetic field in **a** (left) and **b** (right) direction. The anisotropy of the system is apparent from the largely different phase boundaries. The paramagnetic metal (PM), antiferromagnetic nonmetal (AFNM) and antiferromagnetic metal (AFM-b) are common to both magnetic field directions while the ferromagnetic nonmetallic (FNNM) phase is only reachable with the magnetic field in the **a**-direction.

phase is thus denoted as non metallic. In this phase the spins are strongly polarized with an effective momentum of $1.73 \mu_B/\text{Ru}$. In an intermediate temperature regime around 45 K the resistivity shows two transitions from the AFNM phase to a real metallic phase (positive temperature coefficient) and at a higher field to the FNM phase. If the field is aligned along the **b**-axis, the FNM phase is not observed anymore. Instead the critical field needed to suppress the AFNM phase increases linearly with decreasing temperature and is extrapolated to 22.5 T for vanishing temperature. All these data were reported by McCall *et al.* [110], their phase diagram is shown in figure 4.9.

X-ray single-crystal diffraction by Cao *et al.* [113] and combined X-ray diffraction and Raman spectroscopy studies by Iliev *et al.* [114] found the space group $Bb2_1m$ at room temperature and no evidence for a further change of the symmetry at the Néel or the Mott transition. A large coupling of the lattice to the Mott transition was reported by Cao *et al.* [115] who observed a shrinking of the c lattice constant at $T=48$ K. This was confirmed by electron single-crystal and neutron powder diffraction conducted by Yoshida *et al.* [116] who additionally found an increase of the a and b lattice constants at the Mott transition. The low temperature lattice constants obtained from their analysis are $a=5.3577(2)$ Å, $b=5.5356(2)$ Å and $c=19.5212(9)$ Å at 8 K. They were successfully in refining the nuclear structure from the neutron powder diffractograms but the magnetic structure was deduced from the single observed strong magnetic (110) reflection and the absence of the magnetic (300) reflection reflection.

In this context a neutron single-crystal diffraction to unambiguously determine the magnetic structure in both the AFNM and AFM-b phases was planned and executed at the 5C.2 single-crystal diffractometer at the Orphée reactor in Saclay. The results of this experiment will be discussed below. In the meanwhile, resonant x-ray data from Bohnenbuck *et al.* [117] and elastic neutron scattering data from a triple axis spectrometer by Bao *et al.* [118] were published. Both could determine the magnetic structure to be ferromagnetic double layers stacked anti-ferromagnetically along the **c**-axis with the moment along the **b**-direction in the low temperature phase and along **a** in the intermediate phase.

Single crystal neutron diffraction

Single-crystal neutron diffraction was carried out at the 5C.2 diffractometer at the Orphée reactor in Saclay, France. A roughly $4 \times 4 \times 2 \text{ mm}^3$ large crystal of $\text{Ca}_3\text{Ru}_2\text{O}_7$ was mounted in a closed cycle cryostat attached to the eulerian cradle of the diffractometer. A first orientation matrix was determined at room temperature and several scans were done to check, that the crystal is untwinned. Indeed no evidence for twinning was found, especially the (110) reflections are sharp and show no shoulders.

Three datasets were collected, one at 5 K in the antiferromagnetic insulating phase, one at 52 K, i. e. in the intermediate antiferromagnetic metallic phase and the last at 60 K in the paramagnetic phase. Data reduction was performed with the COL5 program and FULLPROF was employed to refine the data.

Prior to the refinement the possible magnetic arrangements were analyzed by the BASIREPS program. This is part of the FULLPROF distribution and calculates the irreducible representations of the space group with respect to the propagation vector. The propagation vector is clearly identified as (001) by the occurrence of magnetic (00 l) reflections with odd l . Given the space group, the position of the ruthenium atom and the propagation vector, BASIREPS finds four one-dimensional representations. The theory of irreducible representations states, that the occurrence of an one-dimensional irreducible representation is equivalent to the description of the magnetic structure by a Heesch-Shubnikov-group⁸. Moreover, the output of a representation analysis is exhaustive, thus exactly four distinct magnetic structures could possibly exist, each is described by one of four distinct magnetic space groups. To determine these, one has to note, that the mirror plane $m_z = (x, y, -z)$ is the product of the glide-plane $b_x = (-x, y + 1/2, z)$ and the screw axis $2_{1,y} = (-x, y + 1/2, -z)$. The magnetic space group is now generated by adding the time reversal operation to some symmetry elements of the underlying space group. Thus the choice of the time reversal symmetry on the glide-plane b_x and the screw axis $2_{1,y}$ immediately fixes the choice for the mirror plane m_z , as the group multiplication table has to be preserved. That results in the four magnetic space groups $Bb2_1m$, $Bb'2_1m'$, $Bb2'_1m'$ and $Bb'2'_1m$.

⁸In the following, the term magnetic space group will be used for the Heesch-Shubnikov-groups.

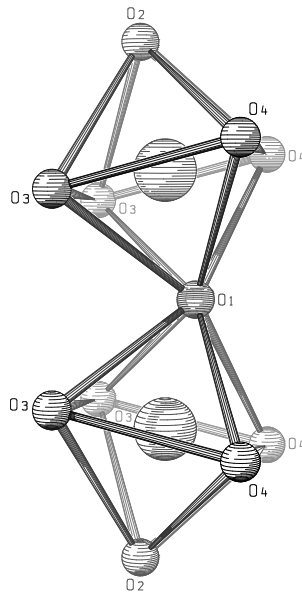
Ru-Pos	$Bb2_1m$	$Bb2'_1m'$	$Bb'2_1m'$	$Bb'2'_1m$
(0 0 0.1)	u v w	u v w	u v w	u v w
(0 0 -0.1)	-u -v w	u v -w	u v -w	-u -v w
(1/2 1/2 0.1)	u -v -w	u -v -w	-u v w	-u v w
(1/2 1/2 -0.1)	-u v -w	u -v w	-u v -w	u -v w

Table 4.3: Different couplings of the magnetic moments within one double layer of $\text{Ca}_3\text{Ru}_2\text{O}_7$ for the four different magnetic space groups. The location of the four ruthenium positions within one bilayer is given in the first column, the symbols ($\pm u$, $\pm v$, $\pm w$) denotes the magnetic moment components at the corresponding position, their coupling is defined by the magnetic space group. Those components that yield a ferromagnetic coupling of one bilayer in a certain direction are shown in bold. The adjacent bilayer at $z=0.5$ is coupled antiferromagnetically due to the occurrence of a propagation vector of (001) and not shown here. Consider for example a phase where the spins are aligned in **b**-direction ($u=w=0$, $v=M$). Ferromagnetically aligned bilayers that are stacked antiferromagnetically (+ + --) are described by $Bb'2_1m'$, whereas $Bb'2'_1m$ describes a magnetic structure, where a bilayer consists of antiferromagnetically ordered single layers. The antiferromagnetic bilayer-bilayer coupling finally results in a (+ - - +) stacking.

Moreover the representation analysis yields the coupling of the magnetic moments between all four ruthenium positions within one bilayer. These are presented in table 4.3. The results of BASIREP show that a collinear alignment of the spins is only possible along the principal axes. Finally the propagation vector (001) clearly indicates an antiferromagnetic coupling of adjacent bilayers.

These results were now used to refine the low temperature data. In a first step, the data was fitted to all four space groups without any restrictions for the direction of the magnetic moment except for the $Bb'2_1m'$ space group, where the refinement of the z -component was unstable and only x and y components were allowed to vary. The instability of the z -component is caused by the domination of magnetic reflections with large l component, both in intensity and number of recorded reflections. The z -component of the magnetic moment does only contribute to those structure factors, whose scattering vector is perpendicular to the magnetization, e.g. mainly to in-plane ones. Those are essentially weak reflections, which on the one hand is the reason of the unstable refinement. On the other hand the occurrence of strong (00 l) reflections and the weakness of the in-plane ones indicate that the magnetic moment is primarily located within the ab -plane, which justifies the neglect of a z -component in the refinement of the $Bb'2_1m'$ space group. The best fit was observed for this space group with an agreement factor $R(F2)_w=6.77\%$. An analysis of the result showed a rather large error for the x component of the magnetic moment which was consequently set to zero and excluded from further refinements. Despite having less degrees of freedom the agreement factor remained constant and only minor changes in the

Figure 4.10: Oxygen environment around the ruthenium ion in the $Bb2_1m$ space group of $\text{Ca}_3\text{Ru}_2\text{O}_7$. Displayed are two octahedra of one bilayer, the viewing direction is the \mathbf{b} -axis, the \mathbf{c} -axis lie vertical. The atomic positions used in creating this sketch, were taken unexaggerated from the 5 K neutron single-crystal diffraction measurement. One of the apical oxygens, O(1), is situated in the middle of the double layer, exactly on the m mirror plane, the other one, O(2) on the outside. O(3) and O(4) are the two inequivalent basal oxygens. The calcium ions are not drawn. The tilting of the octahedra is clearly visible.



remaining parameters were observed. This shows that the AFNM phase consists of ferromagnetic bilayers stacked antiferromagnetically with magnetic moments pointing in the \mathbf{b} -direction, consistent with the results of Bohnenbuck *et al.* and Bao *et al.*. The size of the magnetic moment was determined to be $1.64(3) \mu_B$, comparable to the $1.8(2) \mu_B$ found by Bao. FULLPROF employs the magnetic form factor of Ru^{1+} for the refinement.⁹

The same procedure was performed for the $T=52\text{ K}$ data-set in the AFM-b phase. This time, the best match was found for the $Bb2'_1m'$ space group with an agreement factor $R(F2)_w=5.91\%$. The removal of spin components in \mathbf{b} - and \mathbf{c} -direction did not change the result significantly which shows that the spins are aligned along the \mathbf{a} -axis. The size of the magnetic moment is $0.76(3) \mu_B$. Table 4.3 $Bb2'_1m'$ yields for spins aligned in the \mathbf{a} -direction ($u=M, v=w=0$) only positive coefficients thus the bilayer is again ferromagnetically ordered. Adjacent bilayers are in turn stacked antiferromagnetically.

The analysis of the $T=60\text{ K}$ data is simplified due to the absence of a magnetic order as only a refinement in the $Bb2_1m$ space group had to be performed.

The results of all three refinements are presented in table 4.4. Here hardly any difference is observed in the nuclear structure of the three phases. The atomic positions do not change significantly and the bond lengths basically resemble the course of the lattice constants. The ruthenium-oxygen environment as obtained from the refinement is shown in figure 4.10. This also serves to clarify the nomenclature of the different oxygen positions. O(1) is one apical oxygen located in the middle of the bilayer exactly on the m mirror-plane while O(2) is the second apical oxygen located on the exterior of the bilayer. O(3) and O(4) are basal oxygen atoms. The tilt axis, as determined from the bisectrix of the Ru-O(1)-Ru

⁹The parameters of the form factor are: $A=0.4410$, $a=33.3086$, $B=1.4775$, $b=9.5531$, $C=-0.9361$, $c=6.7220$ and $D=0.0176$, see [119] for the definition of these parameters.

bond angle is rotated by $15(2)^\circ$ from the **b**-axis, thus the largest portion of the Ru-O(1)-Ru bond angle is located in the xz -plane.

Summary

The nuclear and magnetic structure of $\text{Ca}_3\text{Ru}_2\text{O}_7$ was analyzed with single-crystal neutron diffraction at three different temperatures corresponding to the paramagnetic metallic, the antiferromagnetic metallic and the antiferromagnetic insulating phase, respectively. Although the lattice constants show a distinct anomaly at the metal-insulator transition no strong change is observed for the atomic positions. The magnetic order was confirmed to consist of ferromagnetic bilayers which are coupled antiferromagnetically. In the low temperature phase, the magnetic space group is $Bb'2_1m'$ with a magnetic moment of $1.64(3) \mu_B$ pointing along the **b**-direction. At the phase transition to the antiferromagnetic metallic phase the moment is flipped to the **a**-axis with a reduced value of $0.76(4) \mu_B$ whereas the magnetic space group is changed to $Bb2'_1m'$.

		5 K	52 K	60 K
Space group		$Bb'2_1m'$	$Bb2'_1m'$	$Bb2_1m$
a	(Å)	5.3677(2)	5.3637(2)	5.3632(2)
b	(Å)	5.5356(2)	5.5325(2)	5.5315(2)
c	(Å)	19.5212(9)	19.5375(7)	19.5405(7)
R_w	(%)	6.82	6.80	7.25
N_{Nuc}	—	724	490	705
N_{Mag}	—	137	82	—
\mathbf{M}	(μ_B)	1.64(3)	0.76(4)	—
Direction	—	\mathbf{b}	\mathbf{a}	—
Tilt and rotation				
ϕ_{tilt}	deg	14.11(3)	13.80(7)	14.04(5)
ϕ_{rot}	deg	11.26(4)	11.36(4)	11.39(5)
Bond length				
Ru-O(1)	Å	1.9838(11)	1.982(2)	1.986(2)
Ru-O(2)	Å	1.9855(15)	1.987(3)	1.992(2)
Ru-O(3)	Å	2.004(2)	2.002(2)	2.004(2)
Ru-O(3)	Å	2.004(2)	2.004(3)	2.017(3)
Ru-O(4)	Å	1.985(2)	1.980(3)	1.990(3)
Ru-O(4)	Å	1.990(2)	1.989(2)	1.995(2)
Bond angles				
Ru-O(1)-Ru	deg	152.25(9)	152.4(2)	152.22(14)
Ru-O(3)-Ru	deg	149.71(10)	149.82(11)	149.52(13)
Ru-O(4)-Ru	deg	150.44(10)	150.59(12)	150.43(14)
Ru	(x,0,z)			
	x	-0.2517(2)	-0.2519(2)	-0.2518(3)
	z	0.09866(5)	0.09852(12)	0.09855(8)
	U_{11}	0.0004(3)	0.0016(3)	0.0012(4)
	U_{22}	0.0016(3)	0.0016(4)	0.0017(4)
	U_{33}	0.0008(2)	0.0007(10)	0.0012(5)
O(1)	(x,y,0)			
	x	-0.3374(4)	-0.3371(5)	-0.3374(5)
	y	0.0226(5)	0.0225(5)	0.0223(6)
	U_{11}	0.0029(6)	0.0034(8)	0.0035(9)
	U_{22}	0.0058(9)	0.0052(10)	0.0049(11)
	U_{33}	0.0029(5)	0.006(2)	0.0039(11)
O(2)	(x,y,z)			
	x	-0.1824(2)	-0.1825(3)	-0.1833(3)
	y	-0.0198(5)	-0.0209(5)	-0.0209(5)
	z	0.19841(6)	0.19826(13)	0.19845(9)
	U_{11}	0.0036(5)	0.0045(6)	0.0047(6)
	U_{22}	0.0065(6)	0.0059(7)	0.0061(7)
	U_{33}	0.0023(4)	0.0027(13)	0.0049(7)

Continued on the next page

		5 K	52 K	60 K
O(3)	(x,y,z)			
	x	0.0521(2)	0.0526(3)	0.0524(3)
	y	0.2007(4)	0.1999(5)	0.1989(5)
	z	0.08081(6)	0.08113(13)	0.08088(9)
	U ₁₁	0.0020(4)	0.0031(5)	0.0030(6)
	U ₂₂	0.0044(5)	0.0036(6)	0.0050(7)
	U ₃₃	0.0039(4)	0.0079(15)	0.0057(8)
O(4)	(x,y,z)			
	x	-0.4492(2)	-0.4485(3)	-0.4488(3)
	y	0.2968(4)	0.2969(5)	0.2969(5)
	z	0.11607(6)	0.11551(12)	0.11588(9)
	U ₁₁	0.0020(5)	0.0034(6)	0.0028(6)
	U ₂₂	0.0044(5)	0.0044(6)	0.0056(7)
	U ₃₃	0.0042(4)	0.0037(15)	0.0055(7)
Ca(1)	(x,y,0)			
	x	0.2359(4)	0.2363(6)	0.2366(6)
	y	-0.0569(5)	-0.0563(6)	-0.0564(7)
	U ₁₁	0.0024(9)	0.0033(11)	0.0033(12)
	U ₂₂	0.0057(10)	0.0049(12)	0.0053(13)
	U ₃₃	0.0017(6)	0.004(3)	0.0031(15)
Ca(2)	(x,y,z)			
	x	0.2443(3)	0.2442(4)	0.2444(4)
	y	0.0535(4)	0.0527(5)	0.0524(5)
	z	0.18862(8)	0.18871(15)	0.18880(11)
	U ₁₁	0.0015(6)	0.0025(7)	0.0031(8)
	U ₂₂	0.0037(6)	0.0031(7)	0.0026(8)
	U ₃₃	0.0018(4)	0.0011(18)	0.0032(11)

Table 4.4: Results of the refinement of the nuclear and magnetic structure of $\text{Ca}_3\text{Ru}_2\text{O}_7$ at the temperatures 5 K, 52 K and 60 K, respectively. The lattice constants were taken from [116]. The weighted agreement factors are based on F^2 and are calculated by FULLPROF for all reflections (R_w), including the magnetic ones. Bond length within one octahedron and the bond angles between ruthenium ions within one bilayer are calculated from the refined atom positions. The angle between ruthenium atoms located in different sheets of one bilayer is given by Ru-O(1)-Ru while Ru-O(3)-Ru and Ru-O(4)-Ru denote the bond angles between ruthenium ions within one sheet. The tilt (ϕ_{tilt}) and rotation angles (ϕ_{rot}) are calculated from the basal oxygen positions. Note that the origin of $Bb2_1m$ is not fixed to a point but lies *on* the \mathbf{b} -axis. A collective displacement of all atoms in this direction results in a total equivalent description of the structure. Therefore the y -component of one selected atom has to be fixed to an arbitrary value. In this case, the y -component of the ruthenium position was chosen as 0.

5 Clip

Clip, (Cologne Laue Indexation Program), is a software for the analysis of Laue images. It is provided with a semi-automatically indexing function. This feature gives the possibility to refine a solution and allows to calculate the required rotations to reorient the crystal. It supports multiple crystals and projections at the same time. An unique feature is the native support for the 12-bit gray scale images of the Fuji BAS image plate scanner, which is used at the institute Laue camera. The program has been used very successful since 2006.

The software is written in the PYTHON language [120] with additional C++ parts for the speed-critical sub-systems. The graphical user interface is realized with the help of the QT [121] toolkit and its python bindings PYQT [122]. The C++ library is made available to the PYTHON system with the help of the SIP interface generator [123]. The use of the cross-platform toolkit QT and PYTHON allows the use on Linux, Windows and Max OS X computers. Only the small and very portable C++ library has to be specifically compiled for each platform. For the Windows platform, a stripped-down install package including an embedded version of the PYTHON interpreter is available for simple deployment. The program is licensed under the terms of the Gnu General Public License [124] and is publicly available at <http://clip.berlios.de>.

Laue method

The Laue method is a diffraction technique that uses a fixed single crystal and a polychromatic primary beam. This differs from most other diffraction techniques that usually uses a monochromatic beam.

Because of the fixed crystal, the angle θ between the primary beam and a set of lattice planes is fully determined by the crystal orientation. Nevertheless, the Bragg equation $\lambda = 2 \cdot d \cdot \sin(2\theta)$ can be satisfied, if the wavelength λ is contained in the primary beam. Therefore a large number reflections occur, even with a stationary crystal, which is the big advantage of the Laue method. The direction of a scattered beam does not depend on the lattice plane spacing d or equivalently on the length of the reciprocal lattice vector but only on the direction of the latter. Thus higher harmonic reflections always overlap with the fundamental one.

This represents the drawback of the Laue method. The length of the reciprocal lattice vector is not accessible and thus the determination of lattice constants is not possible.¹ Moreover because of the systematic massive spot overlap and the

¹At least not in a simple and straight forward way, see [125].

wavelength dependence of the primary beam intensity, the scattering amplitude is different to extract, which complicates the application of the Laue method for the structure solution.

But because of the large number of spots and its simple interpretation as a special kind of projection of the reciprocal lattice, the Laue method is commonly used to determine the crystal orientation.

Nomenclature To clarify the description of the program below, the following nomenclature will be used: *Reciprocal lattice vector*, *reciprocal space vector* and *scattering vector* are used interchangeably and denote a rotated linear combination of the reciprocal lattice basis vectors \mathbf{a}^* , \mathbf{b}^* and \mathbf{c}^* . Different from that is the *scattered ray* or *scattered beam* which denote the actual x-ray or neutron beam emerging from the crystal after diffraction. It forms twice the angle with the primary beam as the scattering vector does. Finally *Reflection* or *spot* represents the actual spot that is caused by the scattered beam on the two-dimensional detector or film. These objects are different aspects of the same diffraction process and will be labeled with the Miller indices of the reciprocal lattice vector. In this sense, a (hkl) reflection is a spot caused by a diffraction with a scattering vector equal to the (hkl) reciprocal lattice vector.

5.1 Program Description

Coordinate system

The details of the underlying coordinate system are usually not of much interest for the routine use of Clip, nevertheless it is sometimes useful to know the chosen convention.

The crystal resides at the origin of the laboratory coordinate system. The primary beam points along the positive \mathbf{x} -axis, $k_i = (0, 0, +k)$, the \mathbf{z} -axis points upwards, and the \mathbf{y} axis in the horizontal direction.

The crystal coordinate system is defined by the crystal axes \mathbf{a} , \mathbf{b} , and \mathbf{c} . Within the local coordinate system of the crystal, \mathbf{a} is defined to point in the $\hat{\mathbf{x}}$ direction, \mathbf{b} lies within the $\hat{\mathbf{x}}\hat{\mathbf{y}}$ plane with a positive $\hat{\mathbf{y}}$ component and \mathbf{c} completes the right-handed system. The basis vectors of the reciprocal space are defined in the usual way as $\mathbf{a}^* = \frac{1}{V}(\mathbf{b} \times \mathbf{c})$, $\mathbf{b}^* = \frac{1}{V}(\mathbf{c} \times \mathbf{a})$ and $\mathbf{c}^* = \frac{1}{V}(\mathbf{a} \times \mathbf{b})$. With this choice, \mathbf{c}^* points along the $\hat{\mathbf{z}}$ -axis.

The translation from the local crystal system to the laboratory frame done by a rotation matrix \mathbf{R} . If Euler angles are used to describe this matrix, the angles are Ω , χ and Φ and refer to rotations around the \mathbf{z} -, \mathbf{x} - and \mathbf{y} -axis, respectively where the Ω rotation is performed last. Thus the rotation matrix is $\mathbf{R} = \mathbf{R}_z(\Omega) \cdot \mathbf{R}_x(\chi) \cdot \mathbf{R}_y(\phi)$. A reciprocal lattice vector \mathbf{G} defined by its Miller indices (hkl) is expressed in the laboratory frame as $\mathbf{G} = \mathbf{R} \cdot (\mathbf{a}^* \cdot h + \mathbf{b}^* \cdot k + \mathbf{c}^* \cdot l)$.

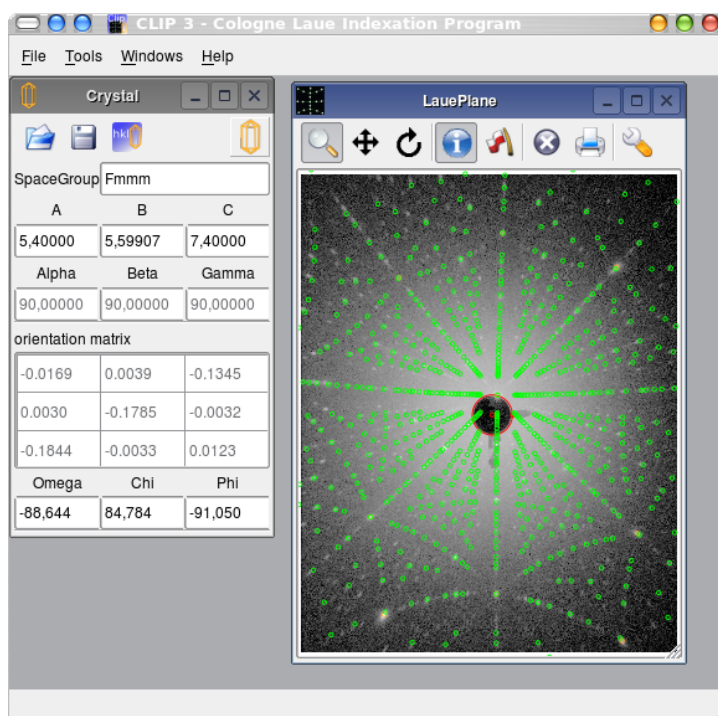


Figure 5.1: Clip main window with crystal definition and one Laue Plane

Main Window

Figure 5.1 shows the main window of Clip with the two principal sub-windows, the crystal definition and the Laue projection plane.

The work paradigm is to define one or several crystals and connect them to projectors, which display a point pattern derived from either the direct or the reciprocal lattice of the crystal. The details of the projection depends on the type of the projector. One crystal might be connected to many projectors, while a projector can only be connected to a single crystal but the majority of cases will only employ a single crystal and a single projector. Up to now, two different projectors are available, a stereographic projection of reciprocal lattice vectors and a planar projection of the scattered ray vector, the latter represents exactly the pattern observed on an usual Laue diffractometer with a flat film. But other types of projectors might be implemented, like a gnomonic projection of the reciprocal space or cylindrical² or conical Laue-camera geometries.

Crystal and projector windows can be opened from the *File* menu. Additionally, the complete workspace can be saved and restored here. This save and restore function covers all crystal data and the settings of projectors connected to them. This allows to save the result of an indexing, including the refined parameters and the marked spots. The *Tools* menu allows to open the tool windows, which are described below in their occurrence in a typical workflow.

²This type of geometry is used i. e. by the neutron Laue diffractometer Vivaldi [126] at the ILL

Crystal Window

Figure 5.2 shows window for the definition of the crystal parameters. The three toolbar buttons at the top allow the save and load the crystal definition to a xml file and to start the indexing procedure. The xml-file generated by the save button contains the space group, the lattice parameters and the three Euler angles. The crystal icon in the upper right corner can be dragged to a projection window to connect them.

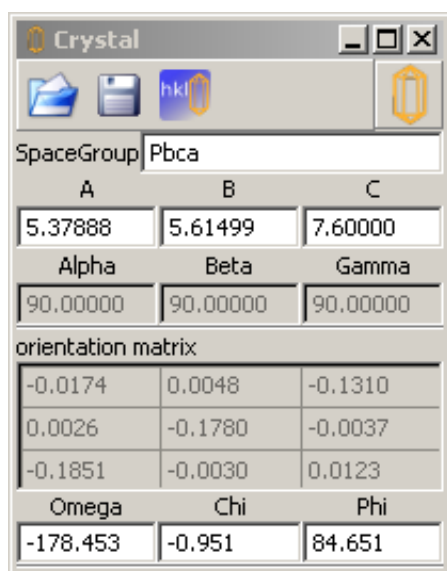


Figure 5.2: Crystal parameter input window.

Below the toolbar, one finds the input for the space group (*SpaceGroup*). The space group determines the enterable lattice parameters (e.g. all angle parameters are fixed to 90° for the orthorhombic space groups) and allows to identify and suppress equivalent solutions in the indexing procedure. The program uses a very relaxed checking of the space group. Everything which is formally correct should be accepted, e.g. $F1$, $F4/mmm$, $Pbaa$ but not $Paaa$ ³. At the moment systematic extinctions, even for the lattice centering, are not handled, therefore e.g. $Pmmm$, $Pnma$ and $Fmmm$ would give exactly the same result. A special treatment is implemented for the trigonal space groups. If entered as e.g. $R3m$, the program uses the rhombohedral primitive setting $a = b = c$, $\alpha = \beta = \gamma$, when entered using the non-standard centering symbol “H” ($H3m$) the hexagonal setting $a=b \neq c$, $\alpha = \beta = 90^\circ$, $\gamma = 120^\circ$ is used. When changing directly between these space group symbols, the lattice constants and the crystal orientation are converted accordingly in order to get the same diffraction pattern. The crystal orientation is performed in a way, that $(111)_{rhomb}$ and $(1\bar{1}0)_{rhomb}$ coincides with the $(001)_{hex}$ and $(100)_{hex}$, respectively.

The inputs for the lattice constants (A , B , C , $Alpha$, $Beta$, and $Gamma$) are found below the space group input. Depending on the entered space group, some of the fields are disabled, e.g. for a cubic space group, only the a lattice constant has to be entered. Below the lattice constants, the orientation matrix is displayed. It consists of the rotated reciprocal lattice basis vectors, expressed in the Cartesian laboratory frame. Finally, at the bottom, inputs for the three Euler angles ($Omega$, Chi and Phi) are present. They are updated every time the crystal is rotated.

³The glide vector of the first a glide plane is perpendicular to the plane and thus not necessary. A shift of the plane by $x=1/4$ gives the correct symbol $Pmaa$

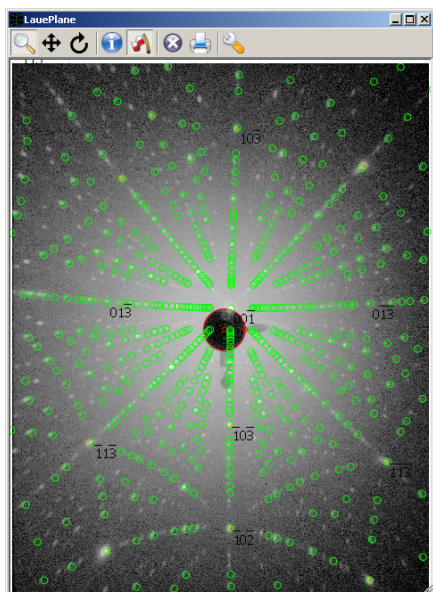


Figure 5.3: Laue plane window with a back reflection Laue image of SmTiO_3 from [127]

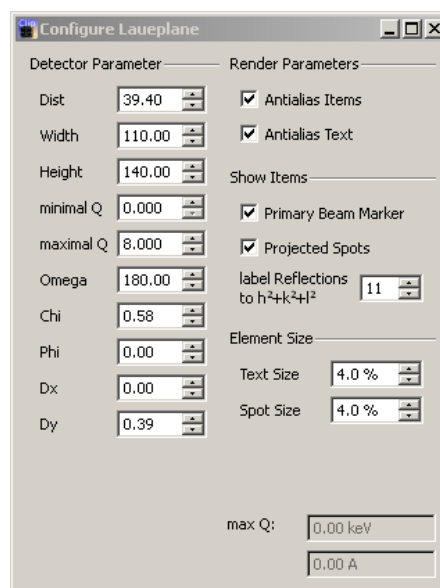


Figure 5.4: Configuration panel for a Laue plane window.

Laue Plane

The Laue plane window represents the film/image plate, where the Laue pattern will be drawn. It displays the recorded image, the primary beam marker, reflection markers and the calculated spots. With the help of the mouse, the image can be resized, visible spots on a recorded image can be marked and the Laue pattern can be moved which corresponds to a change in the crystal orientation.

The mouse action on most of the Laue plane depends on the selected button in the upper toolbar. The three leftmost buttons define the drag'n'drop behavior. If the *magnifying glass* is selected, a press on left mouse button and subsequent drag of the mouse allows to zoom into the Laue plane. If an image is loaded, that is zoomed as well. The *crossed arrows* buttons allows to drag the calculated Laue pattern freely around. During the drag, the mouse position is continuously converted to a scattering vector that would produce a reflection spot at the that position. For each update step, the crystal orientation is changed by a rotation, that brings the previous vector to the actual one. Thus, if one starts the drag at a calculated reflection spot, it will stay at the mouse position. This mode allows a very intuitive navigation through the reciprocal space. If the *circular arrow* is selected, the rotation axis during the drag is confined to a preselected and fixed axis, see the rotation tool.

The next two buttons define the action of a single mouse click with the left button. If the *info* button is selected, an info panel for the nearest reflection is added to the Laue plane. These info panels appear on a printout and will disappear as soon as the crystal orientation is changed. The *flag* button allows to

mark recorded reflections for later use for indexation and orientation refinement. If the cursor moves over an info panels or a reflection marker, it will change to a crossed arrow cursor and the item may be moved by drag'n'drop on the Laue plane.

The primary beam is represented by two concentric red circles, the outer one with a handle. The inner cycle can be dragged around to define the primary beam position on the Laue plane. With the help of the handle of the outer circle, the latter can be resized to match an appropriate feature in the recorded image if such a signature is provided.

A short mouse click with the right button restores the previous zoom level and a longer click on the right button opens a context menu. That allows to set the rotation axis to the reciprocal lattice vector of the reflection that is nearest to the actual mouse position, to delete all reflection information panels and to clear all reflection markers or only the marker nearest to the actual mouse position.

The three rightmost buttons on the toolbar allow one to open or to close a Laue image, to print the Laue plane including all decorations and to open the configuration dialog for this Laue plane. The image file may be any image format that is recognized the PYTHON IMAGE LIBRARY. Additionally the program is able to read the format which is returned by the Fuji BAS image plate reader. This format has a higher dynamic range of 12 bits, compared to 8 bits of conventional gray scale image formats. In order to take advantage of this improved range, the image is internally represented with the full information and mapped to screen colors by an user modifiable transfer curve, see figure 5.10. If an image is loaded, four more buttons for image rotation and flipping appear.

Figure 5.4 shows the configuration dialog. On the left are the parameters of the projection. From top to the bottom they are:

Dist Distance from the crystal to the projection plane.

Width Width of the projection plane. If a BAS image is read, this parameter is taken from the image.

Height Height of the projection plane. If a BAS image is read, this parameter is taken from the image.

minimal Q Lower bound of the wave vector distribution in \AA^{-1} .

maximal Q Upper bound of the wave vector distribution in \AA^{-1} . A higher value produces more spots and may slow down the program. The upper bound is also shown in the lower right corner as x-ray tube voltage⁴ and x-ray wavelength.

Omega, Chi spherical coordinates of the plane normal. Ω is the rotation around the **z**-axis, therefore $\omega=0^\circ$ corresponds to a transmission Laue configuration,

⁴also corresponds to the electron energy

while $\omega=180^\circ$ corresponds to a back reflection Laue configuration. χ is the polar angle.

Phi Rotation of the plane around the plane normal.

Dx and Dy Position of the penetration point of the plane with a line that is normal to the plane and passes the crystal.

On the right side, one finds parameters which alter the appearance of the display. The *Render Parameters* allow one to enable or to disable the anti-aliasing for the text and the items on the projector plane like projected reflection markers. The anti-aliasing provides better image quality but may give a slower update during motions. In the *Show Items* category, the two check boxes allow to show or hide the primary beam marker and the projected spots. The latter is very handy when one marks spots for indexing. Additionally, one can specify, up to which value of $h^2+k^2+l^2$ the index is displayed aside the calculated reflections. Contrary to the reflection info panels, these indicators move along with the reflections which allows a quick navigation in the reciprocal space. Finally the *Element Size* category allows to specify the size for the calculated spots and all text items in the projector plane.

Index Search

Figure 5.5 shows the indexing tool. The aim of this tool is to semiautomatically determine the orientation of the crystal at the time of the exposure.

In order to start the indexing procedure, the correct space group and lattice constants have to be specified, the measured crystal-detector distance has to be entered in the configuration dialog⁵, the primary beam marker should be moved to the appropriate position and some spots have to be marked. Choosing a suitable set of spots depends very much on the experience of the experimenter. Some presumably low indexed spots should be marked to increase the probability that a solution is found and some spots at the border of the detector should be marked to improve the fitting performance. When this setup is complete, one can start the indexing and check if a correct solution is found. Otherwise one should change some of the mark spots, try different lattice constants, detector or fitting parameters and start over with the indexation search.

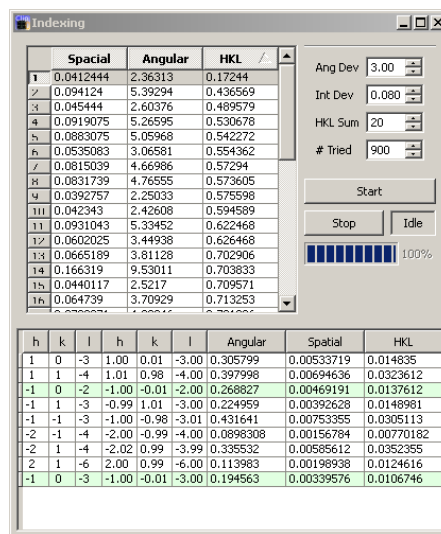


Figure 5.5: Indexing tool window.

⁵a distance of 30 mm is set as default

Description of the indexation algorithm In this paragraph, the algorithm is described, which might help the experienced user to efficiently tune the parameters of the algorithm for improved speed and increased probability to find a correct solution. From a mathematical point of view, indexation is the determination of a rotation matrix \mathbf{R} , that transforms the reciprocal space such that every scattering vector coincide with a reciprocal lattice vector. Note that this is exactly the Laue equation.

From the marker positions and the orientation of the detector in the laboratory frame the direction of the scattered ray is known. The bisection between the scattered ray vector and the primary beam vector represents the scattering vector \mathbf{k}_i . Due to the Laue geometry only its direction is accessible, i. e. a set of unit vectors \mathbf{n}_i for the i -th marked spot serve as input for the algorithm. With the reciprocal space basis vectors \mathbf{a}^* , \mathbf{b}^* and \mathbf{c}^* (or its combination to the matrix \mathfrak{R}), the unknown scattering vector length k_i and the Miller indices $(h_i k_i l_i) = \mathbf{h}_i$, the Laue equation is

$$\begin{aligned} \mathbf{k}_i = k_i \cdot \mathbf{n}_i &= \mathbf{G}_i \\ &= \mathbf{R} \cdot (\mathbf{a}^* \cdot h_i + \mathbf{b}^* \cdot k_i + \mathbf{c}^* \cdot l_i) \\ &= \mathbf{R} \cdot \mathfrak{R} \cdot \mathbf{h}_i \end{aligned}$$

This equation can be transformed to

$$s_i \cdot \mathfrak{R}^{-1} \cdot \mathbf{R}^{-1} \cdot \mathbf{n}_i = [h_i k_i l_i] \quad (5.1)$$

with appropriate scale factors s_i . For a correct rotation matrix and scale factors, the right side of this equation would yield a vector whose components are very close to integers. That allows to build a score function to compare different rotation matrices by summing the deviation from integer components over all \mathbf{n}_i vectors.

In order to create test matrices, the program tries to guess the Miller indices of two scattering vectors. This is done by generating a list of the *# Tried* shortest normalized reciprocal lattice vectors $\{\mathbf{t}_m\}$, calculating all angles between pairs of that list and then comparing these angles with those of all pairs of scattering vectors. If the angles differ by no more than the parameter *Ang Dev*, the two reciprocal lattice \mathbf{t}_m and \mathbf{t}_n are regarded as candidates for the scattering vectors \mathbf{n}_i and \mathbf{n}_j .

$$|\sphericalangle(\mathbf{t}_n, \mathbf{t}_m) - \sphericalangle(\mathbf{n}_i, \mathbf{n}_j)| < \mathbf{AngDev}$$

Now an optimal rotation matrix \mathbf{R}_t is calculated by the Kabsch algorithm [128] with $\mathbf{t}_m = \mathbf{R}_t^{-1} \cdot \mathbf{n}_i$ and $\mathbf{t}_n = \mathbf{R}_t^{-1} \cdot \mathbf{n}_j$.⁶

For the remaining scattering vectors \mathbf{n}_i , the vector $\mathfrak{R}^{-1} \cdot \mathbf{R}^{-1} \cdot \mathbf{n}_i$ is calculated that should be almost scalable to an integer vector according to equation 5.1. The vector is divided by its largest component and successively multiplied by integer values ranging from 1 to *max HKL*. If the difference of the components to integer

⁶A second rotation where \mathbf{t}_m and \mathbf{t}_n are exchanged has also taken into account.

numbers is less than *Int Dev* the components are rounded and used as Miller indices.

If all vectors could be indexed, the optimal rotation matrix is calculated from all scattering vectors. Further on it is checked, that this rotation matrix is not the product of an already found solution with a rotation matrix from the Laue group of the crystal. In that case, the two solutions are equivalent and the newly found is skipped. If it turns out to be unique, the rotation matrix and the determined Miller indices are stored as a new possible solution.

For each solution, the rounded integer and non-rounded Miller indices and three scores are shown. The scores named Angular, Spacial and HKL. HKL is the summed absolute difference from integer of hkl in equation 5.1, Spacial and Angular are defined as follows:

$$\text{Spacial} = \sum_i \mathbf{n}_i - \mathbf{h}_i \quad \text{Angular} = \sum_i \text{acos}(\mathbf{n}_i \cdot \mathbf{h}_i)$$

with $\mathbf{h}_i = \frac{\mathbf{R} \cdot \mathbf{h}_i}{\|\mathbf{R} \cdot \mathbf{h}_i\|}$. The solutions list could be sorted according to all three scores, which allows to quickly check the solutions with the lowest score and hence the highest agreement with the marked spots first. Here the probability of a solution, that does not only match the marked points but the complete pattern is largest.

Parameter Refinement

Figure 5.6 shows the fit tool window. At the top, the parameters which might be varied along with their values are shown. For the cell constants, it is ensured, that at least one of *a*, *b*, and *c* is kept constant, as it is not possible to determine all three with the Laue technique. With the *Index Marker* button, all marked spots are indexed analog to the procedure described in the previous paragraph. With the right *Fit* button, the orientation and all selected parameters will be varied in order to minimize the HKL score factor. For a good fit, some spots at the border of the Laue image should be marked. In the first step, only the orientation should be refined, then the distance, Omega and Chi should be added to the refined parameters and finally the lattice constants could be fitted. If Omega and Chi are refined, the Dx and Dy parameters are adjusted in order to keep the primary beam marker at its position.

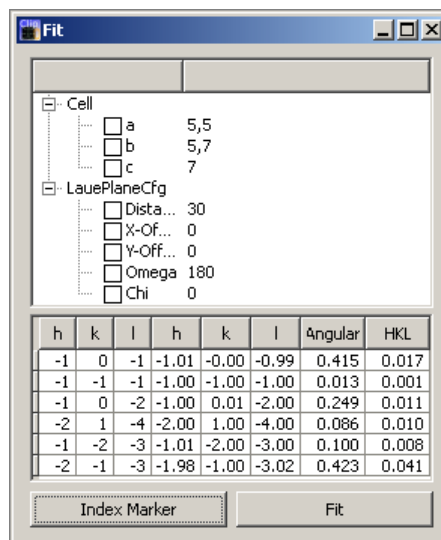


Figure 5.6: Fit window.

Rotation

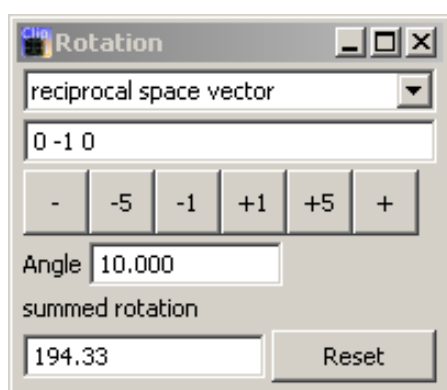


Figure 5.7: Rotation tool window

It is set to zero if the rotation axis is changed or the *Reset* button is pressed. Additionally to the predefined rotation angles of $\pm 1^\circ$ and $\pm 5^\circ$, the input box *Angle* allows to set an user defined one.

Figure 5.7 shows the rotation tool. It allows to select one of the principal laboratory frame axes (primary beam (*z*), horizontal (*x*) or vertical (*y*) axis) or to specify an arbitrary axis in the laboratory frame, the reciprocal space or the direct space as rotation axis. The change of the rotation axis from the Laue plane context menu is forwarded to this tool as well. The accumulated rotation angle is shown in the *summed rotation* box, regardless if the rotation is performed by mouse drags on the Laue plane or the buttons

Reorientation

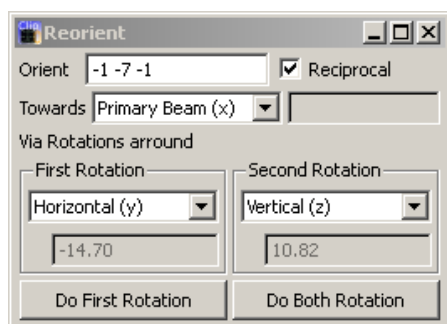


Figure 5.8: Reorientation tool window

the lower part of the window, two combo boxes allow to define the goniometer axis, around which the rotations will be performed, which will be applied in the indicated order (first, second). Thus the axis of the *Second Rotation* is fixed in the laboratory frame, while the axis of the *First Rotation* is influenced by the first one. Below the two combo boxes, the determined rotation angles are shown. The buttons *Do First Rotation* and *Do Both Rotations* allow to adopt the first or both rotations, respectively

The reorientation tool (figure 5.8) allows to calculate the angles, that are necessary to transfer the actual orientation to a desired one. In the top input box (*Orient*), a real or reciprocal lattice vector is entered, which should be rotated towards the direction specified in the combo box in second row (*Towards*). The three principal laboratory axis and arbitrary real and reciprocal lattice vectors are possible choices. For the latter two choices, the text input box will be enabled to enter the desired Miller indices. Fractional indices are possible in this case. In

Reflection Information

The reflection info window shows the angles between a reciprocal lattice vector and the $\pm x$ -, $\pm y$ - and $\pm z$ -axes. The Miller indices are automatically updated upon

a mouse click on the Laue panel if its info mode is active. The nearest reflection to the mouse click position is then chosen. Moreover it is possible to specify the Miller indices manually.

If the angle between the reciprocal lattice vector and the primary beam is less than 90° , the reflection condition is satisfied and a reflection does occur if the structure factor is finite. In that case, Q in \AA^{-1} , the interplane distance d in \AA and the scattering angle 2θ in $^\circ$ are displayed as well. Depending on the selected Q -range for the Laue plane, the diffraction orders that possibly lead to a reflection are shown. Due to the Laue geometry, all these diffraction orders do fully overlap at the same spot.

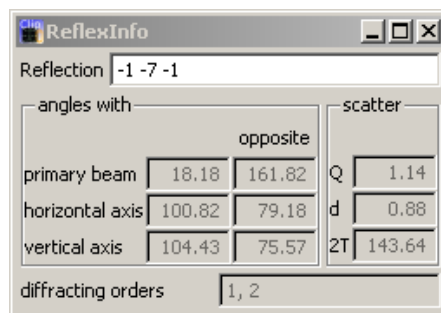


Figure 5.9: Reflection information window

Transfer Curve

The image transfer curve (figure 5.10) allows to adjust the contrast of an image. It works like analog tools in various graphics softwares, like THE GIMP or Adobe PHOTOSHOP. Curves can be edited, and saved to or loaded from disk. Additionally the image might be rotated in 90° steps or flipped horizontally or vertically. In contrast to the similar function of the projector window, only the image itself is affected, neither the aspect ratio nor the marked spots are updated. This serves for the case, where the image orientation is changed and afterwards spots are marked and indexed. If know the workspace is saved and later loaded, the spot positions does not match these of the image. Here, only (!) the image has to be transformed. As this behavior is somewhat special, it will be reimplemented in future versions.

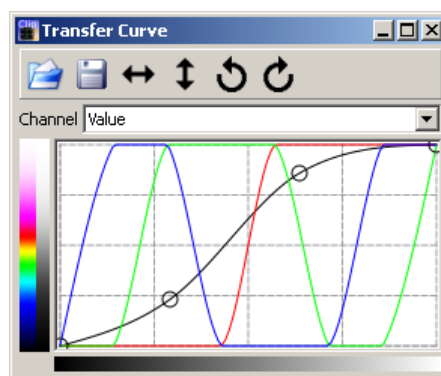


Figure 5.10: Transfer curve tool window

5.2 Future developments

All required features for a successful treatment of Laue exposures are basically available in Clip and the user interface is quite self consistent. Therefore only a few features are scheduled in the short term. These include the handling of systematic extinctions from the space group, the possibility to display some crystal information on the projection plane, an improved marker handling and performance improvements.

Once a marker is placed on the projector plane, there is now way to identify

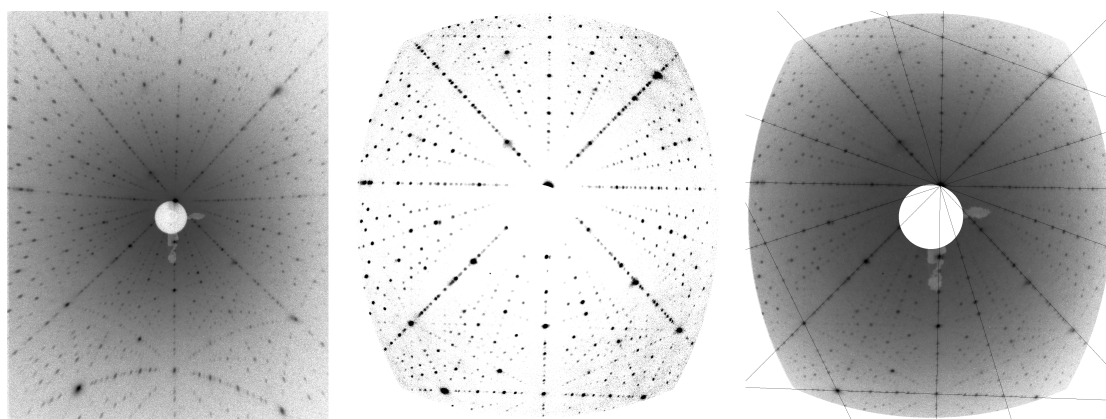


Figure 5.11: (left) Undistorted Laue image of SmTiO_3 . (middle) The calculated gnomonic projection with removed background and saturated spots for enhanced line detection. Note how curved line near the bottom is transferred to straight one. (right) Gnomonic projection without background-removal with the first ten detected lines.

which marker corresponds to which index and score in the indexing and the refinement tool. Thus, it would be very helpful to select in the indexing window a marker line with a bad score and get the corresponding marker highlighted.

It should be possible to add a crystal information panel on the Laue plane, similar to the reflection info panels. This panel should show lattice constants, orientation and some user defined text such as sample description/identification. It will be extremely useful when printing the indexed image and serves as a documentation of the work. Up to now, users manually write these data on the hardcopy.

Long term developments depend strongly on required features. Some possible enhancements are outlined below.

As multicore processors are more and more common, certainly more parts of the code will be ported to multithreading algorithms which in turn would greatly improve performance. More image processing features could be implemented, like cropping the image, background reduction or new image formats. Up to now, no handling of twinned crystals is possible. It would be nice, if the twinning law could be entered to clip and spots for different twins are marked e. g. by different colors.

The indexing routine might be updated. Indexing relies on marking at least two low indexed reflections. The algorithm itself allows to use direct space vectors instead of or additional to reciprocal space vectors as input. As direct space vectors correspond to zones in the reciprocal space and especially low indexed zones form clearly visible curved lines of bright spots in the diffraction pattern, this might give better results for indexation in particular in pathological cases. In fact the second edition of clip uses this approach but it was abandoned as spot had to be selected separate for indexing and refining which decelerates the workflow.

Another improvement in indexing would be a fully automatic algorithm, at least

for simple problems. Wenk *et al.* [129] propose an algorithm where the Laue image is transformed by a gnomonic projection. This projection transfers great circles viz. zones to straight lines, see figure 5.11. Low indexed zones with lots of bright spots appear as pronounced lines, which in turn are detected by a subsequent Hough transform. First test showed indeed human visible straight lines, but the background of the image plate images needs to be carefully stripped in order to reliably recognize them by the computer. So the crucial step is a fool-proof background reduction, which also would be an improvement in itself.

A model of the crystal structure could be used to calculate the spot intensities. This would allow to handle weak reflections which might not be visible on the exposure. They might just be masked if below a certain threshold or the size of the calculated spots could scale with calculated intensity.

At the very end, clip might support the integration of spots, scaling them according to the wavelength distribution etc. and output in a form suitable for single-crystal refinement.

5.3 Summary

Clip has proven to be a very useful program for crystal orientation in the institute of physics II. The discussion with users, also external ones, indicate, that Clip is also an user-friendly program that is quite easy to learn. The latter point is clearly difficult to judge for the author of the program

The development basically followed the suggestions and needs of the users⁷, therefore some simple features like systematic extinctions are not yet available, while others like printing of the Laue plane are.

Clip has been extensively used in the institute of physics II for orientation and checking a large variety of crystals. Its indexing algorithm showed good performance in the automatically determination of the orientation of most of the samples.

The fit procedure allows one to distinguish between various models, if some common crystallographic sense is used. The pseudo-cubic perovskites may serve as an example. They often crystallize in the orthorhombic space group $Pbnm$, which emerges from the cubic base structure by a rotation of 45° around the c -axis and doubling of the c -lattice constant. Thus, the lattice constants in terms of the cubic a lattice constant are roughly $\sqrt{2}a$, $\sqrt{2}a$, and $2a$, with only a very small difference between the a and b lattice constants. A direct assignment from the calculated pattern is in most cases ambiguous. If one records a Laue pattern with the (001) reflection in direction of the primary beam and mark some reflections, the refinement of the a and b lattice parameters will find the orthorhombic orientation. This allows to distinguish between the short and long in-plane axis and works surprisingly well for small orthorhombic splittings.

⁷and the authors interests

Clip might profit from further development, but its present version is successfully employed for routine orientation. Its automatic indexation routine largely simplifies the task of crystal orientation for the user.

6 Powder Diffractometers

During this thesis, a fair amount of work was done in improving the control program of the powder diffractometers. This program was initially developed in collaboration with Matthias Haider during his diploma thesis in the LABVIEW programming language. This chapter will summarize the changes from the point described in the diploma thesis of Matthias Haider [8].

The cryostat temperature control was implemented with the help of a fuzzy logic controller, but did not yield a satisfactory regulation performance. Section 6.1 describes the new approach with two coupled PID loops.

While temperature dependent measurements are done normally at defined temperature points, it is sometimes desirable to sweep the temperature and measure without temperature stabilization as often as possible. Section 6.2 introduces the sweep module, discusses the possible applications and finally presents a real-world example.

The last section in this chapter gives an introduction to the various tools for calibration of the powder diffractometers. Here a step by step tutorial will show the procedure for a complete alignment.

6.1 Cryostat Control

One of the outstanding features of the D5000 diffractometer¹ is the ability to record powder diffractograms from 10 K up to ~ 1500 K. While the HTK for temperatures above room temperature includes its own proprietary temperature controller which only has to regulate the heating current, the situation for the cryostat is more challenging. Here the cryostat temperature is controlled by two variables, the heater on the helium evaporator and an adjustable valve between the cryostat exhaust and the helium pump.

Figure 6.1 shows the hardware setup of the cryostat system. Helium is drawn from the dewar and enters the evaporator where it is heated to the appropriate temperature. It then passes the sample which has no direct contact with the evaporator and is therefore thermalized mainly by the helium. Afterwards the helium cools the radiation shield, passes a computer controlled valve where the flow is regulated and is then pumped to the helium recovery line. The heater is operated by a genesis 2000 PID controller. Additionally, this unit has four

¹In this context, the term “D5000” denotes one of the two powder diffractometers of the institute. Both of them are in fact equipped with a Siemens D5000 goniometer. The second diffractometer is called “Drehanode” and the control program is able to control both units.

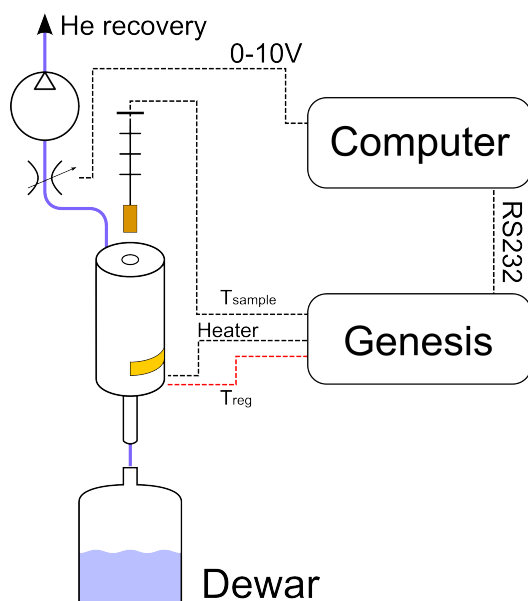


Figure 6.1: Overview of the cryostat configuration. The pump draws helium from the dewar through the cryostat, the flow rate is adjusted with the electromechanical valve between cryostat exhaust and helium pump. The Genesis temperature controller measures the temperature of the evaporator and the sample and drives the heater. The computer operates the genesis controller via a serial connection and the helium valve via a voltage.

channels for silicon diode temperature sensors with $10\ \mu\text{A}$ excitation current. The helium valve is controlled by a digital/analog converter card inside the control computer.

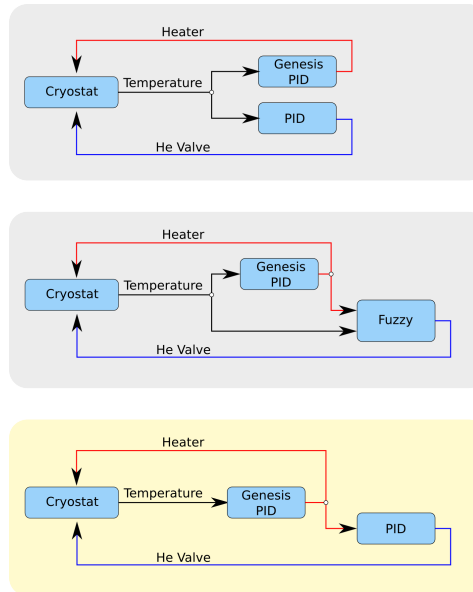
After a defect of the heater, we decided to modify the system in order to improve the regulation performance. Until then, the heater consisted of a constantan wire, which was wound around the inlet of the evaporator with several layers and glued with GE 7031 varnish. Because of poor thermal conductance the wire was prone to overheat at higher currents. This effect strengthened over time, as the GE 7031 varnish evaporates and the layers are only loosely packed. Therefore we installed five high-power resistors in TO-220 packages, which were soldered directly on the copper surface of the evaporator. This ensured a much better thermal conductivity and allows about two times higher heating power.

As a second modification an extra temperature sensor was added. By then, the temperature was solely measured at the sample holder position inside the helium flow by a DT-670 silicon diode, which resulted in a long time delay between a change in the heater output and a corresponding reaction of the temperature sensor. We believed, that this was the major issue for the poor temperature stabilization.

As a calibrated DT-670 diode is relative expensive, we used the cheap 1N4148² model for the first tests and calibrated several of them with the “Schnellmessstab”. One, whose calibration curve was stable during several thermal cycles was selected for the cryostat. The resulting calibration curve shares the features of the standard curves DT-670 and DT-400 like the strong increase at low temperatures, but show different absolute values and a stronger slope, see figure 6.5a. The diode was glued near to the heating resistors in the isolation vacuum space and the calibration

²100 diodes can be bought for approximately 1euro.

Figure 6.2: Different control schemes employed in temperature regulation. **Top:** Two PID loops regulating the Heater and the Helium Valve separately. **Middle:** One PID loop operates the heater, plus a fuzzy logic controller operating the helium valve with cryostat temperature and heating power as input. **Bottom:** Two coupled PID loops. The primary loop operates the heater and serves as input for the secondary loop, which operates the helium valve.



curve were loaded in the genesis controller. The output of this sensor is then used for temperature regulation.

It turned out, that despite the calibration, the two sensors did not indicate the same temperature. Especially at low temperatures, the sample temperature is about 10 K lower than the regulation temperature. As we were initially not sure about the general applicability and long term stability of the 1N4148 diode, we did not adopt the calibration curve, but instead we monitored the behavior over several cooling cycles. Beside this issue, the performance was so good, that we decided not to replace the 1N4148, as it is used only for temperature regulation while the sample temperature itself is measured with the proven DT-670 diode.

After these hardware modifications, we redesigned the control program in order to change the algorithm and to account for the additional temperature sensor, the 1N4148 diode for temperature regulation. The DT-670 is now solely utilized to determine the sample temperature.

The challenging part of the cryostat temperature control is the integration of the helium valve in the whole control loop. The use of the genesis controller constrain the heater control to the PID loop running in the genesis controller itself. Three schemes have been developed over time, see figure 6.2 for a graphical representation. The first one consists of the heater PID loop and a helium valve PID loop running parallel. Both loops utilize the temperature as input and operate their output in order to drive the temperature to the desired setpoint. As e. g. an increase of the heating power could be compensated by a corresponding increase of the helium flow, there is a multitude of optimal outputs for the two loops, which are all equivalent. As a PID loop only has one input parameter, no additional knowledge could feed to the system, which would break this equivalence. Therefore it is not possible to simultaneously minimize the helium flow, which is greatly desirable, both for cost reasons and for increased measurement time with one

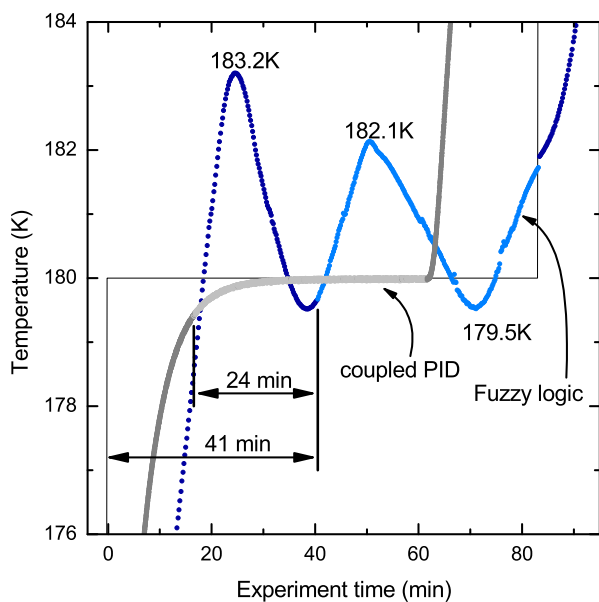


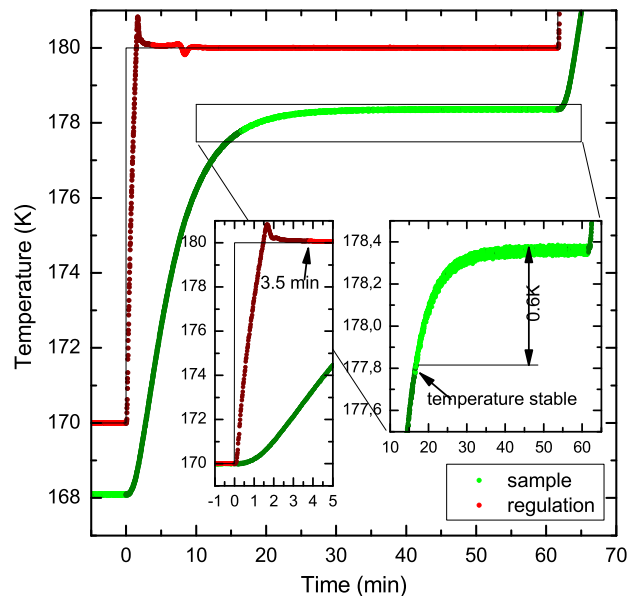
Figure 6.3: Comparison of a temperature step performed with the fuzzy logic controller and the new control program. Both curves show the temperature at the sample position, the curve for the coupled PID is shifted to match the setpoint. Light colors indicate the period, were the diffractogram is taken. The Fuzzy logic controller performs much worse, it takes 41 min before the temperature is stable and even then it oscillates with ~ 2.6 K.

hundred liter dewar. Further on, the two coupled loops tend to oscillate against each other.

These problems were addressed in the second approach, where a fuzzy logic controller using the temperature deviation and the heater setting as input controls the helium valve. Unfortunately the LABVIEW implementation of the fuzzy logic controller is very cumbersome to use. The fuzzy logic rules have to be edited in a special editor and saved to a binary file which is then loaded by the control VI. The definition and fine tuning of the rules is very time consuming and does not allow separate parameterizations for different temperature regimes. This might be addressed using not only the temperature deviation but also the absolute temperature as input, but this would multiply the number of parameters. Additionally there is much less expertise in tuning this algorithm than in tuning the better known PID algorithm. This resulted in a less than optimal implementation with poor regulation performance, see figure 6.3.

The new approach to the helium valve control is shown in the bottom part of figure 6.2. We shift back to a conventional PID loop, but use the heater output signal as input for the helium valve operation. The setpoint of the loop is the desired heating current. This design is possible, because e. g. a rise of the helium flow leads to a greater cooling power and therefore a temperature drop. This in turn will be compensated by the heater control loop with an increased heating power. With this scheme, it is possible to regulate the heating power to a chosen value. If selected fairly low, this optimized the helium consumption. The absolute minimum could not be reached, because this would leave no space for heater operation. In order to decouple the loops, the helium valve loop could be parameterized in such a way, that the output varies much slower than the heater output. As the heater PID loop is solely responsible for temperature stabilization, this does not affect the regulation performance.

Figure 6.4: Temperature characteristics of a cryostat measurement step at 180 K upon heating. The red curve shows the regulation temperature, the green one the sample temperature. Light colors indicate the range of stable temperatures. The left inset shows a magnification of the temperature rise. A stable condition is reached 3.5 min after the setpoint change. The right inset shows the sample temperature during the measurement.



The additional temperature sensor requires a modification to the stability criteria. As before, the regulation temperature is assumed to be stable, if the difference to the setpoint is not larger than a specified threshold ($MaxRegDev$) for a minimum time of $MinStableTime$. Because the regulation sensor has a much lower time constant than the sample sensor, the later is normally not settled by then. As it has an offset to the setpoint (see above), the difference to it could not be used. Therefore, the maximal spread may not be larger than $MaxSampleVar$ during the same time $MinStableTime$. The three quantities ($MaxRegDev$, $MaxSampleVar$ and $MinStableTime$) may, like the PID parameters, depend on the setpoint and could be entered in the program. If both temperatures are stable³ the measurement will start.

Figure 6.3 shows the performance of the new control algorithm exemplified by a measurement at 180 K in comparison with the old fuzzy logic controller. Light colors indicate the range of stable temperature control. The fuzzy logic controller shows an overshoot and large oscillations during the measurement. Also it takes twice the time, before the temperature is settled. The new control program, on the other hand, achieves a smooth temperature rise and a very stable sample temperature during the measurement. In the last 20 minutes the temperature is stable within a range of only 0.02 K. Note, that the sample temperature for the new control program has been shifted to match the setpoint.

Figure 6.4 shows the performance of the new cryostat control program in more detail. The regulation temperature is shown in red and the sample temperature in green. The regulation temperature rises extremely fast and becomes stable after only 3.5 min while the sample temperature needs 17 min to stabilize. The parameters were $MaxRegDev=120$ s, $MaxSampleVar=0.5$ K and $MinStableTime=0.5$ K.

³and for technical reasons the time since a setpoint change is greater than $MinStableTime$

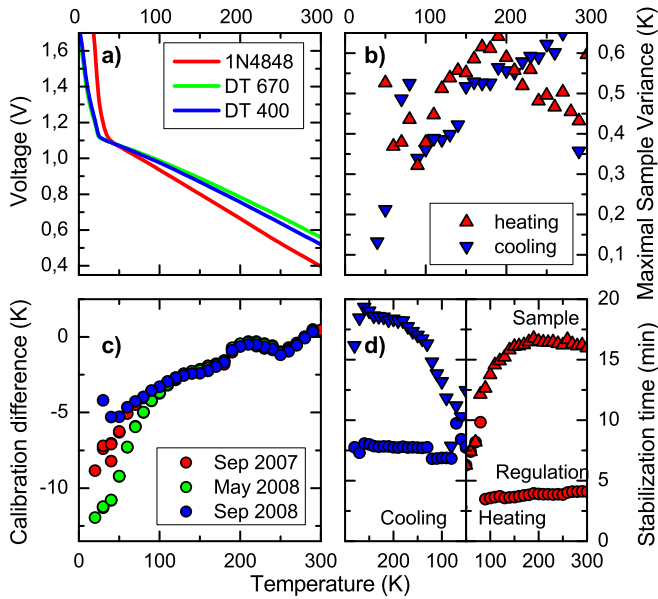


Figure 6.5: Temperature dependence of various cryostat parameters. a) calibration curves for the 1N4148 diode compared with the DT670 and DT400 standard curves. b) temperature drift of the sample temperature during measurement. Shown is the difference between maximum and minimum of the stable sample temperature. c) Offset of the sample temperature from the set-point. Below 100 K the 1N4148 diode is not long term stable. d) Time for the stabilization of regulation and sample temperature.

The two insets show the rise of the regulation temperature and the sample temperature during the measurement, respectively. The sample temperature rises⁴ during the measurement about 0.6 K, a value which might be easily reduced, but only with the drawback of (much) longer stabilization times. As the typical thermal expansion is in the order of $10^{-6}/\text{K}$, this results in an error for the determination of the lattice constants of about 10^{-5} \AA , which is well below the resolution of the diffractometer.

Figure 6.5a shows the calibration curve of the 1N4148 diode in comparison with the standard curves for DT-670 and DT-400. The slope is somewhat larger, but the kink at $\sim 25 \text{ K}$ is not as steep and shifted in temperature. The difference of the sample temperature from the setpoint ($T_s - T_{set}$) as function of the setpoint is shown in figure 6.5c determined during three different measurement cycles from September 2007 until September 2008. The difference ranges between 0 K at room temperature and $\sim 12 \text{ K}$ at low temperatures. Down to 125 K, all three curves lie on top of each other, showing no time dependence. From there on, the differences start to deviate. As it is very unlikely, that the calibration curve of the DT-670 diode, which is intended for measurements at low temperatures, will change over time, there must be a change to the calibration curve of the 1N4148. Fortunately the change does only lead to a maximal scatter of 7 K for the regulation temperature and does not affect the precise determination of the sample temperature. Only to adjust to a well defined sample temperature below 75 K is hampered. This shows, that the 1N4148 diodes are suited for undemanding applications, especially when the costs would prevent the use of the more expensive commercial low temperature sensors.

Figure 6.5b shows the maximal variation of the sample temperature as function

⁴this changes upon cooling, where the sample temperature of course drops at the beginning of the measurement

of temperature. In the whole temperature range, the temperature does not drift by more than 0.7 K.

In figure 6.5d the time needed for temperature stabilization is showing that the sample and the regulation temperature, separately upon cooling and heating. While the time needed for stabilizing the regulation temperature shows basically no dependence of the temperature, it does strongly depend on the direction of the temperature change. This is due to the fact, that the heater is regulated to $\sim 15\%$ heating current which translates to only 2% ⁵ heating power, while the maximal heating power is limited to 72% . The maximal increase of the heating power is much larger than decreasing it. If the heater is completely switched off, the helium flow has to be increased in order to increase the cooling rate. For a better regulation stability the speed of change of the helium flow rate was explicitly chosen quite low. Hence cooling takes longer time. Due to the inertia of the cryostat this does not influence the sample temperature that drastically, the difference between heating and cooling is not that pronounced. Here the stabilization time displays a temperature dependence, below 150 K it strongly decreases.

All these facts shows the very good performance of the new cryostat controller compared to the fuzzy logic controller. In December 2008 a new commercial cryostat from the company CryoVac was ordered, which was commissioned just at the end of this thesis. With minor modifications to the program done by O. Breunig and marginal advice of the thesis author the new cryostat could be operated successfully.

6.1.1 Front Panel

Figure 6.6 shows the cryostat control VI front panel. VI is the abbreviation for Virtual Instrument, the LABVIEW term for a program.

- A** Here, the setpoints for temperature and the heater could be read and changed. If the temperature setpoint is changed, either manually or by the TScan or TSweep VI's, the PID parameters for the Genesis controller and the helium valve and the stabilization criterions are updated. The time since stabilization is reset to zero.
- B** The temperatures of the two sensors near the heater and at the sample position are displayed.
- C** This panel shows the parameters for temperature stabilization and indicates, whether the criterions are met. The button pops up a window which shows the actual values used in the determination of stability.
- D** The PID parameters for the temperature control by the Genesis controller, the heating current limit in % and the actual value of the heating current

⁵P = U · I = R · I² : (15%)² = 2.25%

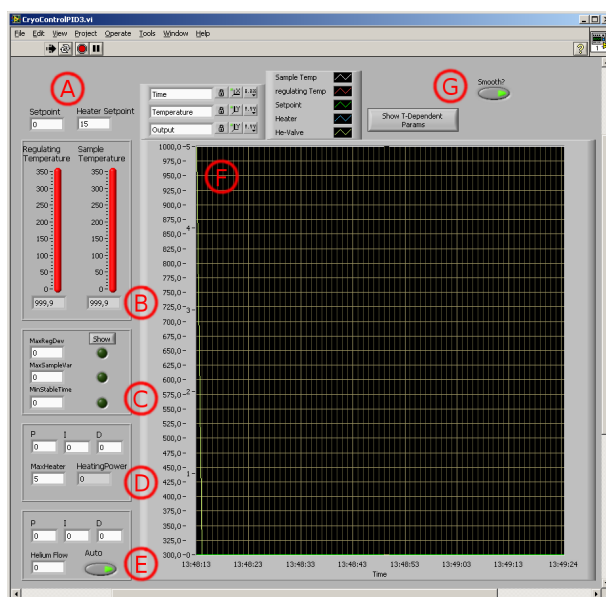
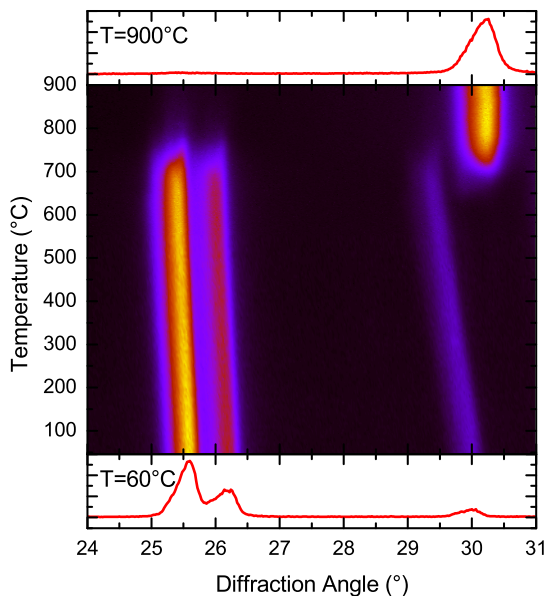


Figure 6.6: Front panel of the cryostat control VI. See the text for a description of the marked items.

are displayed. Upon a setpoint change, the PID parameters are set to the setpoint dependent default values. A change of the heating current limit will be passed to the controller and will stay effective even when the controller is reset.

- E** PID parameters for the helium valve control, the actual value of the helium valve and the ability to switch between manual and automatic control of the helium valve. Upon a setpoint change, the PID parameters are set to the setpoint dependent default values. When in manual mode, the desired helium valve value could be entered in the lower left box. When switching to automatic mode, the PID loop regulates the helium valve bumpless from the entered value. After a setpoint change, the helium valve PID loop is stopped for a specific time, see (G).
- F** The main panel displays curves for the setpoint, regulation and sample temperature, the heating current and the helium valve position. The values are sampled once a second.
- G** The right button switches the smooth setpoint change. If switched off, the setpoint entered at (A) will be instantaneously transferred to the genesis controller and immediately get operative. This results in a step-like change of the setpoint. If activated, the genesis controller will be instead programmed to smoothly vary the setpoint from the actual temperature to the desired value. The maximal acceleration of the setpoint change will be restricted by quadratic start and end segments and a linear segment may be inserted to limit the maximal temperature slope. The setpoint change will be S-like.

Figure 6.7: Result of a temperature sweep measurement of the calcination of SrCO_3 . The data were recorded on the “Drehanode” diffractometer with the high-temperature camera in the temperature range from 50°C to 900°C and in a 2θ range from 24° to 31° . The upper and lower panel show the diffractogram at 60°C and 900°C , respectively. The central color plot shows the evaluation of the diffracted intensity. The phase transition from SrCO_3 to SrO at 750°C is clearly visible.



The left button opens a table with setpoint-dependent parameters. On a setpoint change, the row with smallest distance to the new setpoint is selected and the possibly new parameters are used in the cryostat control VI. The entries are: temperature, for which the line is valid in kelvin, three parameters for stabilization (*MinStableTime* in seconds, *MaxRegDev* and *MaxSampleVar* in Kelvin), six PID coefficients for the Genesis and the helium PID loops (arbitrary units) and the dead-time for the helium valve in seconds.

6.2 Temperature Sweeps

The TScan VI described in [8] was written for precise temperature dependent lattice constants measurements and is very well suited for this purpose. But is need for temperature stabilization impose a rather long idle time which might be tolerable if one measures a complete diffractogram. But if one wants to follow a phase transition which is clearly resolvable by only measure a few peaks, the abdication of the temperature stabilization may considerable speed up the measurement. Hence the TSweep Vi was written, which allows to run a temperature sequence with an arbitrary mixture of ramps and dwell times and at the same time records a (possibly small) section of the diffractogram as fast as possible.

A prove-of-concept application is shown in figure 6.7. SrCO_3 was slowly heated from 50 K to 900 K and diffractograms were taken in a range from 24° to 31° 2θ . With increasing temperature the diffraction lines $\{111\}$, $\{102\}$ and $\{200\}$ at 25.3° , 25.9° and 29.7° respectively shift towards lower diffracting angles due to the thermal expansion. At around 750°C the pattern changes dramatically. The three diffraction lines of SrCO_3 disappear, while a new one at 30.3° appears. As the calcination reaction is known in advance, the new phase could be easily

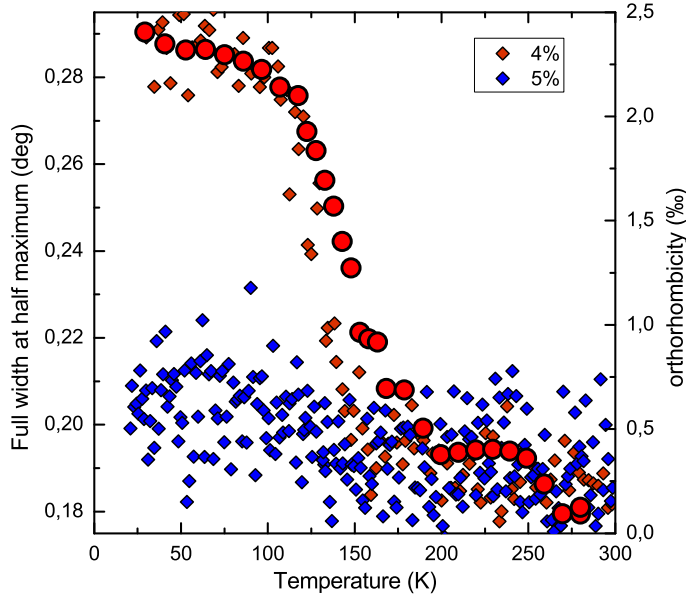


Figure 6.8: Comparison of the FWHM from the $\{110\}_t$ reflection of $\text{LaO}_{1-x}\text{F}_x\text{FeAs}$ samples with composition $x=4\%$ and 5% . For the $x=4\%$ sample, both FWHM from a sweep measurement and orthorhombic splitting ϵ are shown.

identified as SrO with the reflection as $\{111\}$. This particular reaction only serves as an example, but the technique might be used to determine optimal preparation conditions for e.g. transition metal oxides. Limitations of the method are the restricted temperature range of 1000°C and 1600°C for the steel and platinum heating elements respectively, the direct contact to the heating element and the prerequisite to employ a vacuum inside the HTK. The latter restriction might be weakened by using a low pressure atmosphere, but the body of the HTK needs a sub-ambient pressure to remain shut, a pressure above room level would burst the cup open. Additionally when used on a vertical goniometer, the hot gas will ascend and possibly destroy the Kapton foil.

The second example shows the tetragonal to orthorhombic transition in $\text{LaO}_{1-x}\text{F}_x\text{FeAs}$. For doping levels $x < 5\%$, the system shows a transition from the tetragonal space group $P4/nmm$ to the orthorhombic space group $Cmma$ at 160 K [130]. Above 5% doping, the structural transition is suppressed and the system shows superconductivity below 25 K . The physical details will be discussed in [131].

The lattice constants for several samples were measured with the cryostat and the conventional TScan VI. In order to collect more dense data on the structural transition in an acceptable time, we additionally used the TSweep VI to scan the $\{110\}_t$ reflection, which splits into the $\{200\}_o$ and $\{020\}_o$ reflections. These reflections are only 3° apart from the silicon $\{111\}$ reflection, therefore we could, with only limited expenditure of time, additionally collect this for calibration purposes. Figure 6.8 shows the result of this study. For $x=4\%$ sample, both FWHM of the $\{110\}_t$ reflection and the orthorhombic splitting ϵ derived from a lattice constants measurement are shown, while for the $x=5\%$ sample only the FWHM is displayed. The ordinate of the FWHM data is scaled in order to resemble the orthorhombic splitting. While the $x=4\%$ data show the transition at $\sim 160\text{ K}$, the

$x=5\%$ curve stays basically flat. The small increase of the width at low temperatures is not only visible in the $\text{LaO}_{1-x}\text{F}_x\text{FeAs}$ reflections but also in the silicon $\{111\}$ one and is most probable due to the sample displacement in the cryostat. That increases at low temperatures in virtually all cryostat measurements as could be seen in fits with FULLPROF to the diffractograms. The flat FWHM proves, that an orthorhombic distortion does not take place in the $x=5\%$ sample.

Figure 6.9 shows the TSweep VI front panel. In the upper part, it does not deviate to much from the TScan VI. One has to enter the directory where the data files are stored, a name template for the datafiles and start and end angle, stepwidth and angular speed for the goniometer. The character ”%” in the datafile name template will be replaced by the actual scan number. Different of course are the parameters which determine the temperature program. Like in the TScan VI one has to enter start- and end temperature. The number of temperature steps would make no sense, here, one enters the segment time. Using the same value for start and end temperature is valid and will create a dwell-segment. Entering a zero time creates a jump in the temperature profile, the result depend on the temperature controller but up to now, neither the cryostat nor the HTK controller support this.

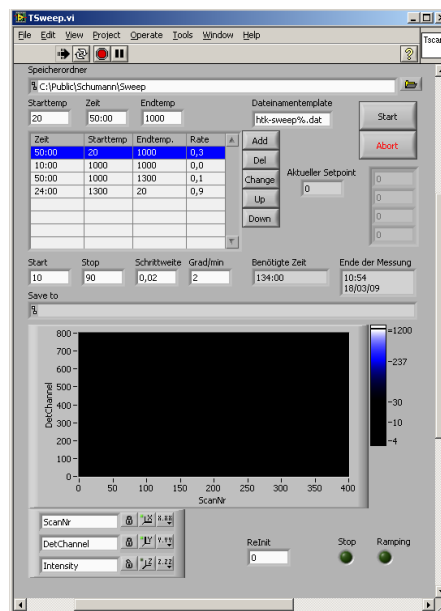


Figure 6.9: Front panel of the TSweep VI.

In the bottom part, a color map display similar to figure 6.7 is located. It gives a first quick overview on the running measurement.

6.3 Calibration Tools

This chapter will describe the various calibration tools. Some of them require the very narrow glass slit at the sample position. This slit, together with an appropriate absorber allows to scan the primary beam, without saturation of the detector. If the absorber is not in place, the detector might get completely locked up and no intensity is measured. If this condition lasts for some time, the detector can be permanently damaged.

Figure 6.10 shows the main calibration panel, which allows to start the specific tool. Additionally, it provides an easy method for setting the goniometer zero-points. *Get Zeros* will read the actual values out of the goniometer controller, while *Set Zeros* will write the values from the input boxes to it. If the *Relative* checkbox is marked, the value of the input boxes will be added to the actual value. If the zero-points are changed, they should be loaded afterwards and noted

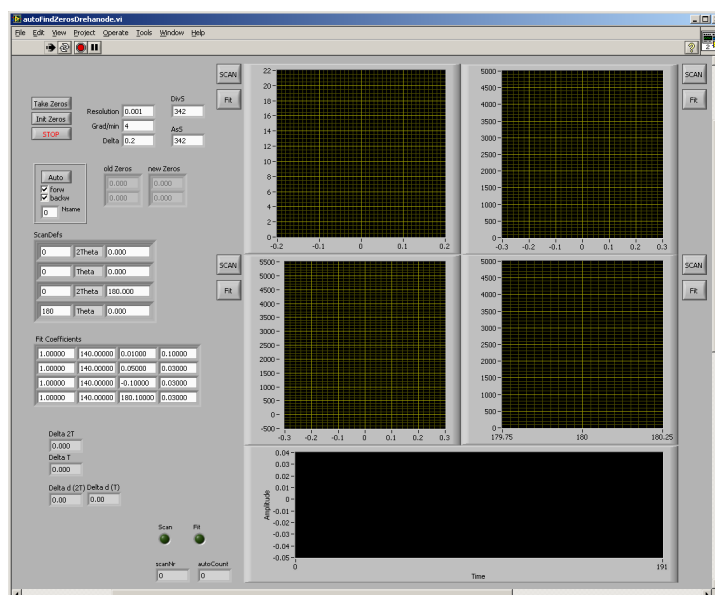


Figure 6.11: Zero-point alignment tool for the point detector

down in the lab book! This tool has to be used very carefully. No confirmation is required to overwrite the correct offsets.

The *DVal Calculator* starts an utility, which calculates the sample displacement from the lattice constants and peak position. This should be routinely used either with the silicon calibration sample or, if silicon is used as internal standard, with the sample one is about to measure. The utility returns the required displacement of the sample holder.

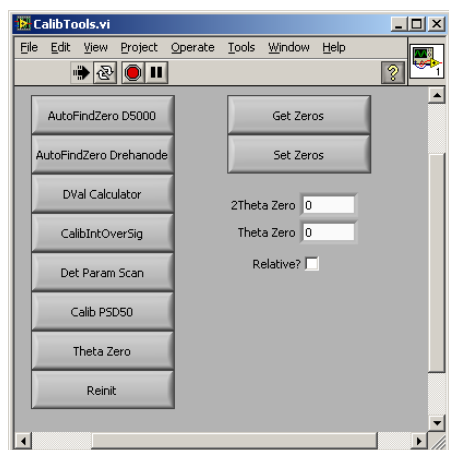


Figure 6.10: Calibration Tool starter

The *Det Param Scan* is an utility to adjust the high voltage and the discrimination for the point detector electronics. It collects the count rate as function of detector voltage or discriminator position. The user could then enter optimized values in the configuration dialog.

The *Theta Zero* tool is useful in the case of a single-crystalline sample where the scattering angle is set to a calculated Bragg reflection and the crystal is rocked around the θ axis. When a reflection is found, the θ angle is not generally the half of 2θ . *Theta Zero* will calculate and employ the necessary zero-point adjustment in order to establish this condition.

Reinit start the internal zero-point scan of the D5000 goniometer controller. The cycles move to a special position which is discovered by a photo-sensor inside the goniometer housing. This has to be done e. g. if limit switch triggers and the crash situation is solved.

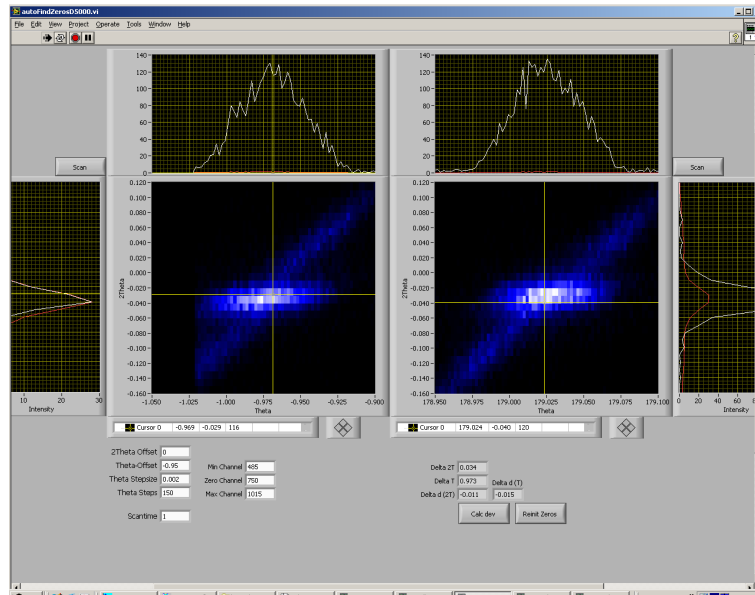


Figure 6.12: Zero-point alignment tool for the linear detector

Figure 6.11 shows the “AutoFindZerosDrehanode” zero-point alignment tool, which is used with the point detector and requires the glass slit at the sample position. It determines the primary beam position by scans of the θ and 2θ axis, while the other axis is fixed. This is done for two θ position of the slit near 0° and 180° , respectively. From these four scans, it is possible to calculate the zero-point offset and the sample displacement. The peak position determined e.g. from a θ scan sets its position for the subsequent 2θ scan and vice versa. Thus several iterations have to be performed until the values have converged.

The two left panels of the VI show the intensity profile of 2θ scans at fixed θ positions while the right ones show the intensity profiles of θ scans at fixed 2θ positions. In upper row the glass slit is positioned near $\theta=0^\circ$ and rotated around 180° in the lower one. The *Scan* button starts the scan for the corresponding panel while the *Fit* button calculates a fit with a gaussian profile. The scan parameter are specified near the upper left panel. If the diffractometer is equipped with motorized slits, their position could be put here as well. If suitable good positions are found manually, the rest of the process could be automated. The *forw* and *backw* checkboxes specify if the scans at $\theta=0^\circ$ and 180° should be carried out respectively. As the θ drive needs quite a long time to go from 0° to 180° and only θ and 2θ values on the same θ side are correlated, *Nsame* specifies the number of iterations in one θ position. If a good solution is found, the new zero-points could be adopted with the *Set Zeros* button.

As a 2θ scan is not feasible with the linear PSD 50 detector, a similar program has been written for this case. Figure 6.12 shows this “AutofindZerosD5000” tool. The linear detector allows to collect the whole θ - 2θ plane with only a single θ scan but with fixed 2θ resolution. The left and right panels correspond to a θ position

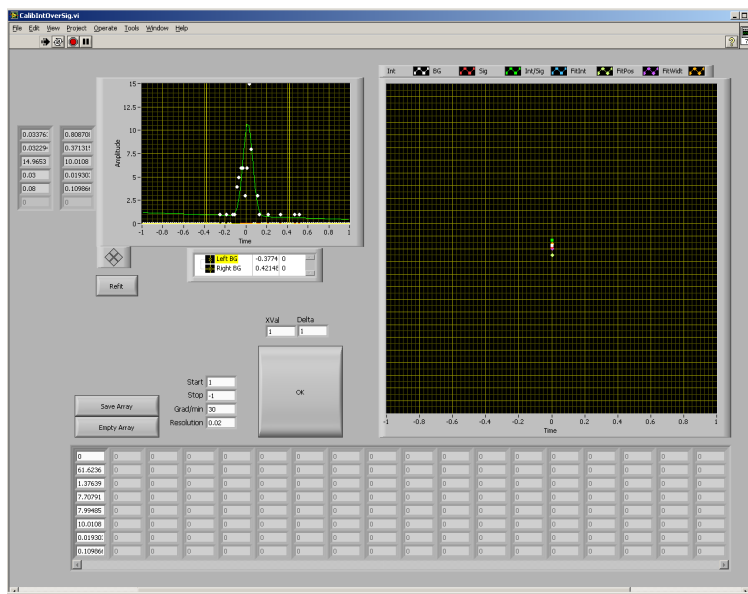


Figure 6.13: General purpose calibration utility

of 0° and 180° respectively and display the typical pattern from the glass slit. The center of gravity of the intensity data is used to calculate the necessary zero-point adjustment.

This tool could also be used to perform a rocking scan with a single-crystal sample. Here the θ and 2θ offset have to be specified accordingly.

The “CalibIntOverSigma” utility (figure 6.13) could be employed to a huge variety of problems. Basically it scans a reflection and determines its intensity, peak height, FWHM and position. The parameters are plotted as function of an arbitrary parameter “XVal”, which might be automatically modified after each scan (“Delta”). This is especially helpful with the PSD 50 detector, whose electronic offers no computer control. The program allows it to very quickly scan a reflection with different setting for e. g. the detector high-voltage or the discriminator position and evaluates their impact. The data might be saved for documentation purposes.

The CalibPSD50 utility (figure 6.14) allows to test the response of the linear detector Braun PSD 50. It requires an aligned glass slit at the sample position. The detector is then moved to the position where the primary beam should be detected in the smallest channel. Then a diffractogram is taken without moving the detector and the peak corresponding with the primary beam is fitted by a gaussian. Then the detector is moved a bit and the next diffractogram is collected. This gives the response to the primary beam at different positions on the detector. As could be seen in the figure, this response is not uniformly. The intensity is larger in the center, while the width shows a minimum here, see the blue and green curve respectively. This is just a geometric effect, as the detector uses a straight instead of a curved wire. On the boundaries the primary beam does not

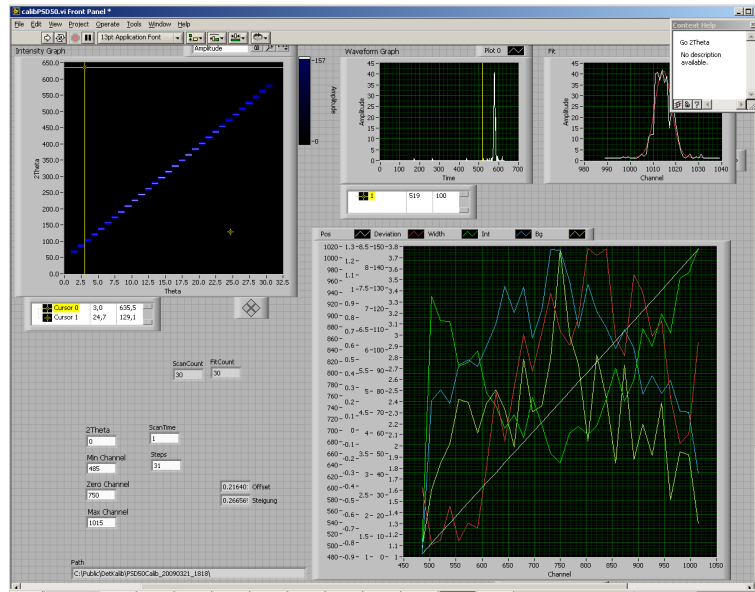


Figure 6.14: Linear detector calibration and inspection tool

enter the detector perpendicular but under a smaller angle, which widens the area where ionization takes place and therefore broadens the peak.

With an optimal calibration, the detector should give a peak-shift of 100 channels per 1° of movement. The red curve shows the deviation of the position from its nominal value. It should be flat or at least symmetric around the center. In the example, this is not the case, on the left side, the deviation is about -0.7 channels and $+0.3$ channels on the left and right side respectively. This would manifest as an additional peak broadening of $1 \text{ channel} \hat{=} 0.01^\circ$ when collecting in moving mode, which is much less than the normal peak width of minimal 0.14° and therefore tolerable. The displays “Offset” and “Steigung” show a fit to this curve. As the channel to angle ratio is adjustable at the detector electronics rack, it could be employed for an adjustment.

There are some more small calibration utilities scattered in the source code directory, which require some deep knowledge of the overall source code and the LABVIEW language. They are definitely less flexible and userfriendly than the described programs and were only required in very special situations.

Appendix A

TasFit

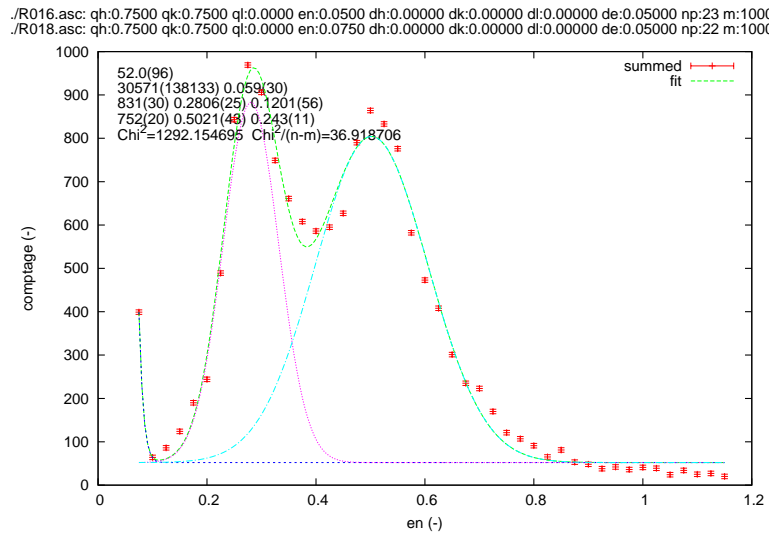


Figure A.1: Graphical output from TASFIT. Displayed is an energy scan at the magnetic zone center ($\frac{3}{4} \frac{1}{4} 0$) of $\text{Pr}_{0.5}\text{Ca}_{1.5}\text{MnO}_4$. See the text for a description.

TASFIT is fitting utility, specially suited to fit scans from triple axis experiments. It's main advantage above other tools is its ability to read several file formats natively, which, at the moment, includes those from the spectrometers Panda and Puma located at the FRM II in munich, 1T¹, 2T, 3T.1, 4F.1 and 4F.2 located in the LLB, Paris and several ILL spectrometers².

A typical result of a fit with TASFIT is shown in figure A.1. An energy scan at a magnetic zone center of $\text{Pr}_{0.5}\text{Ca}_{1.5}\text{MnO}_4$ with two magnon signals and the onset of the elastic line is fitted by three gaussians. For this fit, two scans were added, their scan number and definition is written above the output graph. In the upper left corner, the resulting parameters of the fit are displayed. The first line represents the background, in this case a constant with 52 counts. Next, the height, position and width of the three gaussians are given, most interesting are the position of the two magnon signals at 0.2806(25) meV

¹1T uses it's own file format

²data from IN3, IN8 and IN12 were tested

and 0.5021(43) meV. The fit command used to produce this plot was **fit 16,18, g=2, manual=(50000,'0.0',0.06,'0'),start=1**. The first two numbers, 16 and 18, are scan numbers. These are summed and the resulting curve is fitted with three gaussians. The starting parameters for two of them (**g=2**), are automatically determined and all parameters are allowed to vary. The third gaussian describes the elastic line at E=0 meV. If its position is allowed to vary, the fit does not converge to a meaningful result, thus it has to be fixed. This is achieved by using a string rather than a number as the second element in the **manual=(50000,'0.0',0.06,'0')** list, which creates the third gaussian. The intensity and width are initialized to I=50000 and $\sigma=0.06$ meV. The last part of the command, **start=1**, discards the first point from the experimental data, which has a very large intensity due to its vicinity to the elastic line. Its inclusion would hamper the automatic determination of the initial parameters and strongly flattens the the resolution of the ordinate.

TASFIT has to be called from within the directory containing the data files with the command `TasFit`. Alternatively the environment variable `TASSTORAGE` can be set to the corresponding directory. One has to choose the data file format and is then left on the command line which is in fact a PYTHON shell with the IPYTHON enhancements³. Thus, all commands have to be entered in a valid python syntax, but this approach gives the user the advantage of the complete scripting capabilities of PYTHON. Within the shell, the python object *fit* is the core of the TASFIT functionality. This object can be called like a normal command takes one or more scan numbers plus a set of keyword as arguments. The keyword arguments change the parameters of the fit and consists of the keyword, followed by an equal sign and a value, e. g. *g=3* sets the number of peaks to fit to three.

The enhanced interactive python shell allows one to enter the arguments for a single command without braces, but when used in more elaborate PYTHON constructs, e. g. in loops, one has to enclose all arguments in braces. While `fit 48108,g=2` would be valid as a single command on the command line, a loop has to be entered like the following:

```
for Scan in (48108, 48109, 48110):
    fit(Scan, g=2)
    #do something with the result
```

If *fit* is called with multiple scan numbers, the corresponding scans are combined. All points with similar x values⁴ are summed and then all points are normalized to the same monitor count rate. TASFIT does not check if the result is reasonable, e. g. it is possible to add constant Q and constant E scans.

The summed scans, the fit and individual peaks are plotted with the help of GNPLOT. The parameters of the fit, like intensity, position and width of the peaks, including their errors are written to the console and to the GNPLOT

³IPYTHON improves the interactive characteristics, like command history, online help, etc.

⁴see the keyword argument *fuzzy*

output. All possible keyword arguments and those methods of the *fit* object that are relevant for the user are described in the rest of this chapter.

fit

```
fit 48108,48109,48110
```

This is an instance of the `TASFIT` object but can be called like an ordinary python command. The only difference from the users point of view is the existence of methods like *fit.plot* or member variables like *fit.PeakRes*. The example sum the scans no. 48108, 48109 and 48110 and fit the result with a constant background and a single gaussian peak. The result is displayed in the console window and graphically in the `GNUPLOT` window. The `fit` command is the basis of `TASFIT` and the behavior can be adjusted with keyword arguments.

Keyword *bg*

```
fit 48108, bg=1
```

The argument of the *bg* keyword determines the type of background. If it is an integer value, it sets the degree of the background polynomial, which will be fitted to the data. `bg=0` represents a flat background, `bg=1` a linear one, etc. If the argument is a floating point number or a string of numbers separated by commas, these values represents the coefficients of a background polynomial and will fixed during the refinement, e. g. `bg=3.0` or `bg='3,4'` will set a flat background at 3.0 and a linear background $3+4\cdot x$, respectively. The default is `bg=0`

Keyword *g*

```
fit 48108, g=2
```

The *g* keyword sets the number of peaks, whose parameters are automatically determined. For the peak search, the data is smoothed first. Then the maximum is searched and a parabola is matched to the smoothed data at the five adjacent points to the maximum. From the coefficients of the parabola, the parameters of a gauss peak are determined (the Taylor expansion of the gauss series up to second order gives this correspondence). The resulting peak is subtracted from the smoothed data and the peak search is repeated if necessary. Peaks due to the *manual* keyword are subtracted from the smoothed data *prior* to the peak determination. The default is `g=1`

Keyword *eta*

```
fit 48108, eta=1
```

```
fit 48108, eta=0.5
```

```
fit 48108, eta=None
```

The peak function used within `TASFIT` is a pseudo Voigt function, i. e. the sum of a gaussian and a lorentzian where *eta* is the fraction of the lorentzian. If the

parameter of *eta* is a number, it is fixed during the refinement, *eta*=0 and *eta*=1 correspond to a pure gaussian and a pure lorentzian respectively. If set to *None*, it is allowed to vary during the refinement. The valid range is $0 \leq \text{eta} \leq 1$, the default value is *eta*=0

Keyword start and stop

```
fit 48108, start=2, stop=3
```

The keywords *start* and *stop* discards the first and last N points of the experimental data, respectively. Default is not to crop any points.

Keyword mn

```
fit 48108, mn=10000
```

The *mn* keyword sets the monitor, to which the data should be normalized to. Default is to normalize to the mean monitor of all scans.

Keyword back

```
fit 48108, back=48094  
fit 48108, back=(48094,48095)
```

The *back* keyword allows one to specify a scan number for the background, which should be subtracted from the summed data prior to the fit. If more than one scans contribute to the background, the scan numbers must be enclosed in braces. Background points, which have no counterpart in the "data scans" are skipped. The same holds for points in the "data scans" whit no counterparts in the background. The default is not to have any background scans.

Keyword manual

```
fit 48108, manual=(10000, 0, 0.04, 0)  
fit 48108, manual=((10000, '0', 0.04, '0'), (100,0.3,0.04,'0.75'))
```

The *manual* keyword allows to add peaks with specified parameters for intensity, position, peak width and *eta*-parameter, in this order. The parameters have to be enclosed in braces. If more than one peak is to be entered, the parameter sets have to be enclosed in braces, too. These peaks are in addition to the peaks generated by the *g* keyword and are subtracted from the data prior to the peak search. One has to set *g*=0, if all peaks are created by this keyword, e.g. in the case where the automatic detection of peak parameters does not work and one has to define the initial parameter by hand. If a parameter is not a number but a string, i.e. enclosed in single or double quotes, it is fixed during the fit.

Keyword fuzzy

```
fit 48108, 48109, fuzzy=0.1
```

The summation of different scans may be hampered by round-off errors which most probably exist in the scan files. If the abscissa of two points differ by less than the stepsize times the *fuzzy* parameter, they are considered equal. The stepsize of the data is determined by the smallest stepsize of all data-set or zero if no data-set has at least two points. Default is `fuzzy=0`.

Keyword `save` and `savefit`

```
fit 48108, save='scan.dat', savefit='fit.dat'
```

The keyword *save* writes the, possibly summed, scans to the file given by the argument. It has to be a string representing a valid filename. Any existing file will be overwritten.

The keyword *savefit* does the same for the resulting fit curve. The number of points can be controlled by the variable *fit.fitSavePoints* and defaults to 200. The first and second column of the output file corresponds to the x-coordinate and the total fit curve, respectively. The remaining columns, if any, correspond to the individual peaks, including the background in each case.

Default is not to save the data nor the fit.

Keyword `animate`

```
fit 48108, animate=0.4
```

The keyword *animate* is for debug and fun purposes only. It specifies a time in seconds. Try with `animate=0.4`. The effect is disabled by default.

`fit.plot`

fit.plot is a method of the *fit* object. If it is called instead of *fit*, the scans are just plotted and no fitting is performed. If multiple scan numbers are given, they are not summed, but instead normalized to the same monitor and plotted separately, with different colors.

`fit.lp`

When *fit.lp* is called after *fit* or *fit.plot*, a hardcopy is send to the default printer.

`fit.log`

fit.log (*fname*) enables writing of the fit results to a file called *fname*. For each call to *fit*, a line with all running parameters including their errors is written. Call *fit.log* without parameters to stop the logging.

fit.peakRes

fit.peakRes is no method of *fit* but a three-dimensional list holding the refined parameters including their errors. For instance `fit.peakRes[1]` holds the parameters of the second peak, `fit.peakRes[0][1]` is a tuple containing the value and variance of the position of the first peak and `fit.peakRes[0][2][0]` is the FWHM of the first peak.

The list is populated after each call to *fit* and can be used for many different purposes, e. g. in scripts saving position, intensity and width for many scans at different temperatures to a file. This is a very nice feature, as one can use `TASFIT` to interactively explore the the data and use the same program to automate the fitting of many scans and possibly perform some calculations with the results of the refinement. An example script might look like:

```
% Open a file to write the results
f=open('Resultfile.dat', 'w')
%Loop over scan numbers
for nr in (18123, 18234, 18345, 18456, 18567):
    % Fit with a single gaussian and a fixed background
    fit(nr, g=1, bg=28.0)
    % Write Fileno, Intensity and Position to file.
    % Regard the \n at the end of the format!
    f.write('%i %f %f\n'%(no, fit.peakRes[0][0][0], fit.peakRes[0][1][0]))
f.close()
```

Appendix B

Prepared samples

The prepared samples are labeled by the following nomenclature. The mixed and grounded but not otherwise treated powder is labeled just by "OJS" plus a serial number. Upon the first reaction, a second number is appended and increased for every further reaction step, e. g. OJS35 is the initial powder, and after the heat treatment, the product is labeled OJS35-1 and on further heat treatments OJS35-2, OJS35-3 and so on. Single-crystals are denoted with an "EK" after the initial sample identifier. Every attempt to grow a single-crystal gets its own unique number, e. g. OJS35EK6 is the sixth single-crystal grown out of OJS36-2.

Id	composition	remark
OJS23EK1	RuMa x=0.5 y=0.02	LPCES, 2.5 bar O ₂ , 8mm/h, multiple domains
OJS23EK2	RuMa x=0.5 y=0.02	LPCES, 2.5 bar O ₂ , 8mm/h, multiple domains
OJS22EK1	RuMa x=0.5 y=0.04	LPCES, 3 bar O ₂ , 8mm/h, multiple domains
OJS21EK1	RuMa x=0.5 y=0.06	LPCES, 3 bar O ₂ , 8mm/h
OJS20EK1	RuMa x=0.5 y=0.08	LPCES, 2 bar O ₂ , 10mm/h
OJS20EK2	RuMa x=0.5 y=0.08	LPCES, rod maybe wet, "explodes" in the focus
OJS18EK1	RuMa x=0.5 y=0.1	PH2, 2 bar O ₂ , 8 mm/h, multiple domains
OJS28EK1	RuMa x=0.5 y=0.15	LPCES, 2.5 bar O ₂ , 10mm/h
OJS31EK1	RuMa x=1.0 y=0.10	LPCES, 3 bar Ar, 10mm/h
OJS29EK1	RuMa x=0.5 y=0.20	LPCES, 2.5 bar O ₂ , 10mm/h, feed rod broken
OJS29EK2	RuMa x=0.5 y=0.20	LPCES, 2.5 bar O ₂ , 10mm/h
OJS49EK1	RuMa x=1.0 y=0.30	LPCES, 2.5 bar O ₂ , 10mm/h
OJS49EK2	RuMa x=1.0 y=0.30	LPCES, 2.5 bar O ₂ , 19mm/h
OJS25EK1	LSMO x=0.5	PH2, 2.5bar Ar, 4mm/h
OJS27EK1	LSMO x=0.7	PH2, 2bar Ar, rod directly from educts, no prereaction, no stable growth
OJS34EK1	LSMO x=0.4	PH2, 2.5 bar Ar, 4 mm/h, unstable
OJS45EK1	LSMO x=0.4	LPCES, 2.5 bar O ₂ , 10 mm/h
OJS45EK2	LSMO x=0.4	LPCES, 2.5 bar O ₂ , 6.5 mm/h, very good crystal
OJS46EK1	LSMO x=0.7	LPCES, 2.5 bar O ₂ , 7 mm/h, unstable

Continued on the next page

Id	composition	remark
OJS52EK1	LSMO $x=0.45$	LPCES, 2.5 bar O ₂ , 6.5 mm/h
OJS35EK1	LSMO $x=0.5$	LPCES, after few mm the rod feed falls down
OJS35EK2	LSMO $x=0.5$	LPCES, 2.5 bar O ₂ , 8 mm/h, seed rod split
OJS35EK3	LSMO $x=0.5$	LPCES, 2.5 bar O ₂ , 5 mm/h, good
OJS35EK4	LSMO $x=0.5$	LPCES, 2.5 bar O ₂ , 5 mm/h
OJS35EK5	LSMO $x=0.5$	LPCES, 2.5 bar O ₂ , 5 mm/h
OJS35EK6	LSMO $x=0.5$	LPCES, 2.5 bar O ₂ , 5 mm/h, very good crystal
OJS66EK1	PCMO $x=0.5$	PH2, 3 bar O ₂ , 8 mm/h
OJS66EK2	PCMO $x=0.5$	PH2, 3 bar O ₂ , 3 mm/h

Table B.1: List of the single-crystals grown in the course of this thesis. PH2 and LPCES denotes crystals grown in Cologne and at the university of Orsay, respectively. PCMO is Pr_{1-x}Ca_{1+x}MnO₄, LSMO La_{1-x}Sr_{1+x}MnO₄ and RuMa La_{1-x}Sr_{1+x}MnO₄

Id	composition	Id	composition
$\text{La}_{1-x}\text{Sr}_{1+x}\text{MnO}_4$		$\text{Ca}_{2-x}\text{Sr}_x\text{RuO}_4$	
OJS58	x=-0.1	OJS01	x=2.00
OJS57	x=-0.05	OJS02	x=0.00
OJS50	x=0.0	OJS08	x=0.30
OJS51	x=0.05	OJS09	x=0.30
OJS47	x=0.125	OJS10	x=0.25
OJS34*	x=0.4	OJS11	x=0.22
OJS45*	x=0.4	OJS12	x=0.22 + 14 % Ru
OJS52*	x=0.45	OJS13	x=0.22 + 16 % Ru
OJS25*	x=0.5	OJS14	x=0.30 + 16 % Ru
OJS35*	x=0.5	OJS15	x=0.35 + 16 % Ru
OJS27*	x=0.7	OJS16	x=0.40 + 16 % Ru
OJS46*	x=0.7	OJS17	x=0.45 + 16 % Ru
$\text{La}_1\text{Sr}_1\text{Ru}_y\text{Mn}_{1-y}\text{O}_4$ x=0		OJS19	x=0.08 + 16 % Ru
OJS30	y=0.05	OJS24	x=0.30
OJS59	y=0.05	OJS26	x=0.08
OJS31	y=0.10	OJS32	x=0.08
OJS60	y=0.15	OJS33	x=1.70
$\text{La}_{0.5}\text{Sr}_{1.5}\text{Ru}_y\text{Mn}_{1-y}\text{O}_4$ x=1/2		OJS36	x=0.10
OJS23*	y=0.02	OJS37	x=0.05
OJS22*	y=0.04	OJS38	x=0.06
OJS21*	y=0.06	OJS39	x=0.07
OJS20*	y=0.08	OJS40	x=0.09
OJS18*	y=0.10	OJS41	x=0.125
OJS28*	y=0.15	OJS42	x=0.15
OJS29*	y=0.20	OJS43	x=0.175
OJS49*	y=0.30	OJS44	x=0.22
$\text{Pr}_{1-x}\text{Ca}_{1+x}\text{MnO}_4$		OJS48	x=2.00
OJS66*	x=1/2	OJS53	x=1.90
OJS67	x=2/3	OJS54	x=1.80
OJS68	x=3/4	OJS55	x=1.60
		OJS56	x=1.50

Table B.2: List of sample identifier for all samples prepared in the course of this thesis. The polycrystalline samples, from that single crystals were grown are marked by a star.

List of Figures

2.1	Silicon Lattice Constants	5
2.2	Fits with fixed and running silicon lattice constant	5
2.3	Image of extraction ball mill	7
3.1	Sketch of the COO and Zener-Polaron model	12
3.2	La _{0.5} Sr _{1.5} MnO ₄ single-crystal grown at LPCES	13
3.3	Single-crystal growth with necking technique	15
3.4	Decomposition of Pr _{0.5} Ca _{1.5} MnO ₄ crystals	16
3.5	Possible charge ordering patterns half-doped layered manganites .	17
3.6	Sketch of the distortions appearing at the COO transition	19
3.7	Results of the LSDA calculations from Hua Wu	22
3.8	(<i>h k 0</i>) precession image calculated from Apex images data	27
3.9	Neutron powder diffraction from La _{0.5} Sr _{1.5} MnO ₄ taken at the G4.1	32
3.10	Variation of χ^2 as function of the spin direction	33
3.11	Lattice constants of Ru co-doped La _{0.5} Sr _{1.5} MnO ₄	34
3.12	Magnetic scattering of Ru co-doped La _{0.5} Sr _{1.5} MnO ₄	35
3.13	Diffuse magnetic scattering of La _{0.5} Sr _{1.5} Ru _y Mn _{1-y} O ₄	37
3.14	Superstructure peaks in ruthenium co-doped La _{0.5} Sr _{1.5} MnO ₄ . . .	38
3.15	Magneto-Resistivity of Ru co-doped La _{0.5} Sr _{1.5} MnO ₄	39
3.16	Lattice constants of La ₁ Sr ₁ Ru _y Mn _{1-y} O ₄	40
3.17	Magnetic moment of Sr ₂ Ru _y Mn _{1-y} O ₄	41
3.18	Lattice constants of electron doped La _{1-x} Sr _{1+x} MnO ₄	42
3.19	Temperature dependence of the lattice constants of Pr _{0.5} Ca _{1.5} MnO ₄	43
3.20	Suszeptibility and resistivity of Pr _{0.5} Ca _{1.5} MnO ₄	44
3.21	Results of elastic neutron scattering on Pr _{0.5} Ca _{1.5} MnO ₄	45
3.22	space group relations for single-layered perovskites	48
3.23	Possible space groups for the ordered phase	53
3.24	Magnon dispersion of Pr _{0.5} Ca _{1.5} MnO ₄	55
4.1	Sinter temperature effects	63
4.2	L- <i>Pbca</i> to S- <i>Pbca</i> transition in Ca _{1.92} Sr _{0.08} RuO ₄	65
4.3	Resistivity of Ca _{1.92} Sr _{0.08} RuO ₄	66
4.4	Transitions in Ca _{1.92} Sr _{0.08} RuO ₄	67
4.5	Structural and Metal/insulator transition	68
4.6	Rotation angle doping and temperature dependence	70
4.7	Revised Phase Diagram of Ca _{2-x} Sr _x RuO ₄	72
4.8	Double-layered perovskite structure	73

4.9	H-T Phase diagram of $\text{Ca}_3\text{Ru}_2\text{O}_7$	74
4.10	Ruthenium-oxygen octahedron in $\text{Ca}_3\text{Ru}_2\text{O}_7$	77
5.1	Main window of Clip	83
5.2	Crystal parameter input window.	84
5.3	Laue plane window	85
5.4	Laue plane configuration window	85
5.5	Indexing tool window.	87
5.6	Fit window.	89
5.7	Rotation tool window	90
5.8	Reorientation tool window	90
5.9	Reflection information window	91
5.10	Transfer curve tool window	91
5.11	Laue image and its gnomonic projection	92
6.1	Overview of the cryostat configuration	96
6.2	Sketch of the different employed PID schemes	97
6.3	Comparison of fuzzy logic and dual PID controller performance	98
6.4	Detailed performance of the new control program	99
6.5	Temperature dependence of cryostat parameters	100
6.6	Front Panel of cryostat control VI	102
6.7	Result of a SrCO_3 HTK-sweep measurement	103
6.8	Result of a $\text{LaO}_{1-x}\text{F}_x\text{FeAs}$ cryostat-sweep measurement	104
6.9	Front panel of the TSweep VI.	105
6.11	Zero-point alignment tool for the point detector	106
6.10	Calibration Tool starter	106
6.12	Zero-point alignment tool for the linear detector	107
6.13	General purpose calibration utility	108
6.14	Linear detector calibration and inspection tool	109
A.1	TASFIT graphical output	111

Bibliography

- [1] W. Friedrich, P. Knipping, and M. von Laue, *Interferenz-Erscheinungen bei Röntgenstrahlen*, Sitzungsberichte der Bayerischen Akademie der Wissenschaften zu München **1912**, 303.
- [2] W. Massa, *Kristallstrukturbestimmung*, Vieweg+Teubner, 5 edition, 2007.
- [3] M. Cwik, *The Interplay of Lattice, Spin, and Charge Degrees of Freedom in Layered Cobaltates*, PhD thesis, Universität zu Köln, 2007.
- [4] W.-D. Stein, *Struktur und Gitterdynamik in azentrischen Boraten*, PhD thesis, Universität zu Köln, 2007.
- [5] M. Cramm, *Temperatureabhängige Röntgendiffraktometrie an Seltenerd-dotiertem $(\text{La,Sr})_2\text{CuO}_{d+\delta}$ zwischen 5 und 1600 K*, Diploma Thesis, Universität zu Köln, 1991.
- [6] D. Senff, *Magnetische und orbitale Korrelationen in einfach geschichteten Manganaten der Reihe $\text{La}_{1-x}\text{Sr}_{1+x}\text{MnO}_4$* , Diploma Thesis, Universität zu Köln, 2003.
- [7] P. Steffens, *Struktur und Magnetismus in $\text{Ca}_{2-x}\text{Sr}_x\text{RuO}_4$* , Diploma Thesis, Universität zu Köln, 2003.
- [8] M. Haider, *Strukturuntersuchungen an $\text{La}_{2-x}\text{Sr}_x\text{Co}_{1-y}\text{Ru}_y\text{O}_4$ und Umbau der XPD Anlagen*, Diploma Thesis, Universität zu Köln, 2005.
- [9] K. Lyon, G. Salinger, and C. Swenson, *Linear thermal expansion measurements on silicon from 6 to 340K*, J. Appl. Phys. **48** (1976).
- [10] R. Roberts, *Thermal expansion reference data: silicon 300-850 K*, J. Phys. D – Applied Phys. **14**, L163 (1981).
- [11] D. N. Batchelder and R. O. Simmons, *Lattice Constants and Thermal Expansivities of Silicon and of Calcium Fluoride between 6° and 322° K*, J. Chem. Phys. **41**, 2324 (1964).
- [12] Y. Okada and Y. Tokumaru, *Precise determination of lattice parameter and thermal expansion coefficient of silicon between 300 and 1500 K*, J. Appl. Phys. **56**, 314 (1984).

- [13] J. Cline, R. Deslattes, J.-L. Staudenmann, E. Kessler, L. Hudson, A. Henins, and R. Cheary, *NIST Certificate, SRM 640c Line Position and Line Profile Standard for Powder Diffraction*, 2000.
- [14] M. Gottschlich, *Strukturbestimmungen an Sr_2RhO_4 , $\text{Sr}_2\text{Ru}_{1-x}\text{Ti}_x\text{O}_4$, Ti_2O_3 und V_2O_3* , Diploma Thesis, Universität zu Köln, 2009.
- [15] J. Rodríguez-Carvajal, *Recent advances in magnetic structure determination by neutron powder diffraction*, *Physica B* **192**, 55 (1993).
- [16] V. Petricek, M. Dusek, and L. Palatinus, *Jana2000. the crystallographic computing system*, 2006.
- [17] W. L. Bond, *Making Small Spheres*, *Rev. Sci. Instrum.* **22** (1951).
- [18] E. A. Cordero-Borboa, *An improved grinder for single crystal x-ray diffraction work*, *J. Phys. E – Sci. Instrum.* **18** (1985).
- [19] M. Meven, *HeiDi - Heisses Einkristalldiffraktometer*, Website, 2009, <http://www.frm2.tum.de/wissenschaft/diffraktometer/heidi>.
- [20] V. Hutanu, M. Meven, and G. Heger, *Construction of the new polarised hot neutrons single-crystal diffractometer POLI-HEiDi at FRM-II*, *Physica B* **397**, 135 (2007), Proceedings of the Sixth International Workshop on Polarised Neutrons in Condensed Matter Investigations.
- [21] Stoe & Cie, *DIF4 Diffractometer Control Program*, Stoe, Darmstadt.
- [22] J. B. Goodenough, *Theory of the Role of Covalence in the Perovskite-Type Manganites $[\text{La}, \text{M(II)}]\text{MnO}_3$* , *Phys. Rev.* **100**, 564 (1955).
- [23] E. O. Wollan and W. C. Koehler, *Neutron Diffraction Study of the Magnetic Properties of the Series of Perovskite-Type Compounds $[(1-x)\text{La}, x\text{Ca}]\text{MnO}_3$* , *Phys. Rev.* **100**, 545 (1955).
- [24] R. von Helmolt, J. Wecker, B. Holzapfel, L. Schultz, and K. Samwer, *Giant negative magnetoresistance in perovskitelike $\text{La}_{2/3}\text{Ba}_{1/3}\text{MnO}_x$ ferromagnetic films*, *Phys. Rev. Lett.* **71**, 2331 (1993).
- [25] Z. Jirák, S. Krupicka, Z. Simsa, M. Dlouhá, and S. Vratislav, *Neutron diffraction study of $\text{Pr}_{1-x}\text{Ca}_x\text{MnO}_3$ perovskites*, *J. Magn. Magn. Mat.* **53**, 153 (1985).
- [26] H. Kawano, R. Kajimoto, H. Yoshizawa, Y. Tomioka, H. Kuwahara, and Y. Tokura, *Magnetic Ordering and Relation to the Metal-Insulator Transition in $\text{Pr}_{1-x}\text{Sr}_x\text{MnO}_3$ and $\text{Nd}_{1-x}\text{Sr}_x\text{MnO}_3$ with $x \sim 1/2$* , *Phys. Rev. Lett.* **78**, 4253 (1997).

- [27] Z. Jirák, F. Damay, M. Hervieu, C. Martin, B. Raveau, G. André, and F. Bourée, *Magnetism and charge ordering in $Pr_{0.5}Ca_xSr_{0.5-x}MnO_3$ ($x=0.09$ and 0.5)*, Phys. Rev. B **61**, 1181 (2000).
- [28] Y. Tomioka and Y. Tokura, *Bicritical features of the metal-insulator transition in bandwidth-controlled manganites: Single crystals of $Pr_{1-x}(Ca_{1-y}Sr_y)_xMnO_3$* , Phys. Rev. B **66**, 104416 (2002).
- [29] P. G. Radaelli, D. E. Cox, M. Marezio, S. W. Cheong, P. E. Schiffer, and A. P. Ramirez, *Simultaneous Structural, Magnetic, and Electronic Transitions in $La_{1-x}Ca_xMnO_3$ with $x=0.25$ and 0.50* , Phys. Rev. Lett. **75**, 4488 (1995).
- [30] C. H. Chen and S.-W. Cheong, *Commensurate to Incommensurate Charge Ordering and Its Real-Space Images in $La_{0.5}Ca_{0.5}MnO_3$* , Phys. Rev. Lett. **76**, 4042 (1996).
- [31] P. G. Radaelli, D. E. Cox, M. Marezio, and S.-W. Cheong, *Charge, orbital, and magnetic ordering in $La_{0.5}Ca_{0.5}MnO_3$* , Phys. Rev. B **55**, 3015 (1997).
- [32] J. Blasco, J. Garcia, J. M. de Teresa, M. R. Ibarra, J. Perez, P. A. Algarabel, C. Marquina, and C. Ritter, *Charge ordering at room temperature in $Tb_{0.5}Ca_{0.5}MnO_3$* , J. Phys. – Condens. Matter **9**, 10321 (1997).
- [33] F. Millange, S. d. Brion, and G. Chouteau, *Charge, orbital, and magnetic order in $Nd_{0.5}Ca_{0.5}MnO_3$* , Phys. Rev. B **62**, 5619 (2000).
- [34] P. M. Woodward, D. E. Cox, T. Vogt, C. N. R. Rao, and A. K. Cheetham, *Effect of Compositional Fluctuations on the Phase Transitions in $Nd_{0.5}Sr_{0.5}MnO_3$* , Chem. Mat. **11**, 3528 (1999).
- [35] A. Daoud-Aladine, J. Rodríguez-Carvajal, L. Pinsard-Gaudart, M. T. Fernández-Díaz, and A. Revcolevschi, *Zener Polaron Ordering in Half-Doped Manganites*, Phys. Rev. Lett. **89**, 097205 (2002).
- [36] G. Zheng and C. H. Patterson, *Ferromagnetic polarons in $La_{0.5}Ca_{0.5}MnO_3$ and $La_{0.33}Ca_{0.67}MnO_3$* , Phys. Rev. B **67**, 220404 (2003).
- [37] S. Grenier, J. P. Hill, D. Gibbs, K. J. Thomas, M. v. Zimmermann, C. S. Nelson, V. Kiryukhin, Y. Tokura, Y. Tomioka, D. Casa, T. Gog, and C. Venkataraman, *Resonant x-ray diffraction of the magnetoresistant perovskite $Pr_{0.6}Ca_{0.4}MnO_3$* , Phys. Rev. B **69**, 134419 (2004).
- [38] R. J. Goff and J. P. Attfield, *Charge ordering in half-doped manganites*, Phys. Rev. B **70**, 140404 (2004).
- [39] M. Benomar, *Einkristall-Präparation und Charakterisierung von dotiertem La_2MO_4 mit $M=Co, Mn$ und Ni* , PhD thesis, Universität zu Köln, 2007.

- [40] P. Reutler, *Korrelierte Orbitale in $La_{1-x}Sr_{1+x}MnO_4$* , PhD thesis, Rheinisch-Westfälische Technische Hochschule Aachen, 2007.
- [41] M. Benomar, private communication.
- [42] D. Senff, F. Krüger, S. Scheidl, M. Benomar, Y. Sidis, F. Demmel, and M. Braden, *Spin-Wave Dispersion in Orbitally Ordered $La_{1/2}Sr_{3/2}MnO_4$* , Phys. Rev. Lett. **96**, 257201 (2006).
- [43] U. H. Zucker, E. Perenthaler, W. F. Kuhs, R. Bachmann, and H. Schulz, *PROMETHEUS. A program system for investigation of anharmonic thermal vibrations in crystals*, J. Appl. Cryst. **16**, 358 (1983).
- [44] N. E. Brese and M. O’Keeffe, *Bond-valence parameters for solids*, Acta. Cryst. B **47**, 192 (1991).
- [45] J. Herrero-Martín, J. García, G. Subías, J. Blasco, and M. C. Sánchez, *Structural origin of dipole x-ray resonant scattering in the low-temperature phase of $Nd_{0.5}Sr_{0.5}MnO_3$* , Phys. Rev. B **70**, 024408 (2004).
- [46] A. Gukasov, M. Braden, R. J. Papoular, S. Nakatsuji, and Y. Maeno, *Anomalous Spin-Density Distribution on Oxygen and Ru in $Ca_{1.5}Sr_{0.5}RuO_4$: Polarized Neutron Diffraction Study*, Phys. Rev. Lett. **89**, 087202 (2002).
- [47] M. Merz, G. Roth, P. Reutler, B. Büchner, D. Arena, J. Dvorak, Y. U. Idzerda, S. Tokumitsu, and S. Schuppler, *Orbital degree of freedom in single-layered $La_{1-x}Sr_{1+x}MnO_4$: Doping- and temperature-dependent rearrangement of orbital states*, Phys. Rev. B **74**, 184414 (2006).
- [48] M. Merz, P. Reutler, B. Büchner, D. Arena, J. Dvorak, Y. Idzerda, S. Tokumitsu, and S. Schuppler, *$O1s$ and $Mn2p$ NEXAFS on single-layered $La_{1-x}Sr_{1+x}MnO_4$: crystal field effect versus orbital coupling mechanism*, Eur. Phys. J. B **51**, 315 (2006).
- [49] Y. Murakami, H. Kawada, H. Kawata, M. Tanaka, T. Arima, Y. Moritomo, and Y. Tokura, *Direct Observation of Charge and Orbital Ordering in $La_{0.5}Sr_{1.5}MnO_4$* , Phys. Rev. Lett. **80**, 1932 (1998).
- [50] J. García, M. C. Sanchez, J. Blasco, G. Subias, and M. G. Proietti, *Analysis of the x-ray resonant scattering at the Mn K edge in half-doped mixed valence manganites*, J. Phys. – Condens. Matter **13**, 3243 (2001).
- [51] S. B. Wilkins, P. D. Spencer, P. D. Hatton, S. P. Collins, M. D. Roper, D. Prabhakaran, and A. T. Boothroyd, *Direct Observation of Orbital Ordering in $La_{0.5}Sr_{1.5}MnO_4$ Using Soft X-ray Diffraction*, Phys. Rev. Lett. **91**, 167205 (2003).

- [52] S. B. Wilkins, N. Stojić, T. A. W. Beale, N. Binggeli, C. W. M. Castleton, P. Bencok, D. Prabhakaran, A. T. Boothroyd, P. D. Hatton, and M. Altarelli, *Resonant soft x-ray scattering investigation of orbital and magnetic ordering in $La_{0.5}Sr_{1.5}MnO_4$* , Phys. Rev. B **71**, 245102 (2005).
- [53] S. S. Dhesi, A. Mirone, C. De Nadai, P. Ohresser, P. Bencok, N. B. Brookes, P. Reutler, A. Revcolevschi, A. Tagliaferri, O. Toulemonde, and G. van der Laan, *Unraveling Orbital Ordering in $La_{0.5}Sr_{1.5}MnO_4$* , Phys. Rev. Lett. **92**, 056403 (2004).
- [54] U. Staub, V. Scagnoli, A. M. Mulders, K. Katsumata, Z. Honda, H. Grimmer, M. Horisberger, and J. M. Tonnerre, *Orbital and magnetic ordering in $La_{0.5}Sr_{1.5}MnO_4$ studied by soft x-ray resonant scattering*, Phys. Rev. B **71**, 214421 (2005).
- [55] D. J. Huang, W. B. Wu, G. Y. Guo, H.-J. Lin, T. Y. Hou, C. F. Chang, C. T. Chen, A. Fujimori, T. Kimura, H. B. Huang, A. Tanaka, and T. Jo, *Orbital Ordering in $La_{0.5}Sr_{1.5}MnO_4$ Studied by Soft X-Ray Linear Dichroism*, Phys. Rev. Lett. **92**, 087202 (2004).
- [56] Bruker AXS, Smart and saint area detector control and integration software, 2007.
- [57] G. M. Sheldrick, Sadabs. program for empirical absorption correction of area detector data., 1996.
- [58] A. Komarek, private communication.
- [59] B. J. Sternlieb, J. P. Hill, U. C. Wildgruber, G. M. Luke, B. Nachumi, Y. Moritomo, and Y. Tokura, *Charge and Magnetic Order in $La_{0.5}Sr_{1.5}MnO_4$* , Phys. Rev. Lett. **76**, 2169 (1996).
- [60] K. Ufer, G. Roth, R. Kleeberg, H. Stanjek, R. Dohrmann, and J. Bergmann, *Description of X-ray powder pattern of turbostratically disordered layer structures with a Rietveld compatible approach*, Z. f. Krist. **219**, 519 (2004).
- [61] J. Rodríguez-Carvajal, private communication.
- [62] M. Tokunaga, N. Miura, Y. Moritomo, and Y. Tokura, *High-field magnetization and magnetoresistance of $La_{0.5}Sr_{1.5}MnO_4$* , Phys. Rev. B **59**, 11151 (1999).
- [63] B. Raveau, C. Martin, A. Maignan, M. Hervieu, and R. Mahendiran, *Mn-site doping in colossal magnetoresistance manganites*, Physica C **341**, 711 (2000), International Conference on Materials and Mechanisms of Superconductivity High Temperature Superconductors VI, Houston, Texas, 20-25 Feb 2000.

- [64] A. Shames, E. Rozenberg, M. Auslender, G. Gorodetsky, A. Yakubovsky, S. Gudenko, C. Martin, and A. Maignan, *Ru doping of the Mn site in $La_{0.4}Ca_{0.6}MnO_3$ perovskite: Electron magnetic resonance study of electronic and magnetic ordering*, J. Appl. Phys. **99** (2006).
- [65] P. D. Battle, A. M. T. Bell, S. J. Blundell, A. I. Coldea, E. J. Cussen, G. C. Hardy, I. M. Marshall, M. J. Rosseinsky, and C. A. Steer, *Chemically Induced Magnetism and Magnetoresistance in $La_{0.8}Sr_{1.2}Mn_{0.6}Rh_{0.4}O_4$* , J. American Chem. Soc. **123**, 7610 (2001).
- [66] C. S. Hong, W. S. Kim, N. H. Hur, and Y. N. Choi, *Magnetic and neutron diffraction studies of long-range ferromagnetic order in monolayered manganites*, Phys. Rev. B **68**, 064425 (2003).
- [67] D. Senff, *Neutron Scattering Studies on Magnetic Excitations in Complex Ordered Manganites*, PhD thesis, Universität zu Köln, 2007.
- [68] I. Klassen, *Aufbau eines Magnetkryostaten für Transportmessungen im Hochtemperaturbereich*, Diploma Thesis, Universität zu Köln, 2006.
- [69] R. Kilian and G. Khaliullin, *Orbital polarons in the metal-insulator transition of manganites*, Phys. Rev. B **60**, 13458 (1999).
- [70] M. Ibarra, R. Retoux, M. Hervieu, C. Autret, A. Maignan, C. Martin, and B. Raveau, *Charge-orbital ordering above room temperature in the 2D $Pr_{1-x}Ca_{1+x}MnO_4$ manganites*, J. Solid State Chem. **170**, 361 (2003).
- [71] K. Chao, D. Huang, J. Okamoto, H.-J. Lin, C.-H. Hsu, Y. Kaneko, R. Mathieu, W. Wu, Y. Tokura, and C. Chen, *Orbital ordering of layered manganites from resonant soft X-ray scattering*, J. Magn. Magn. Mat. **310**, 819 (2007), Proceedings of the 17th International Conference on Magnetism, The International Conference on Magnetism.
- [72] S. Chi, F. Ye, P. Dai, J. A. Fernandez-Baca, Q. Huang, J. W. Lynn, E. W. Plummer, R. Mathieu, Y. Kaneko, and Y. Tokura, *Effect of antiferromagnetic spin correlations on lattice distortion and charge ordering in $Pr_{0.5}Ca_{1.5}MnO_4$* , Proc. Nat. Acad. Sci. **104**, 10796 (2007).
- [73] S. Larochelle, A. Mehta, L. Lu, P. K. Mang, O. P. Vajk, N. Kaneko, J. W. Lynn, L. Zhou, and M. Greven, *Structural and magnetic properties of the single-layer manganese oxide $La_{1-x}Sr_{1+x}MnO_4$* , Phys. Rev. B **71**, 024435 (2005).
- [74] J. D. Axe, A. H. Moudden, D. Hohlwein, D. E. Cox, K. M. Mohanty, A. R. Moodenbaugh, and Y. Xu, *Structural phase transformations and superconductivity in $La_{2-x}Ba_xCuO_4$* , Phys. Rev. Lett. **62**, 2751 (1989).

- [75] M. Fujita, H. Goka, K. Yamada, and M. Matsuda, *Competition between Charge- and Spin-Density-Wave Order and Superconductivity in $La_{1.875}Ba_{0.125-x}Sr_xCuO_4$* , Phys. Rev. Lett. **88**, 167008 (2002).
- [76] P. G. Radaelli, D. G. Hinks, A. W. Mitchell, B. A. Hunter, J. L. Wagner, B. Dabrowski, K. G. Vandervoort, H. K. Viswanathan, and J. D. Jorgensen, *Structural and superconducting properties of $La_{2-x}Sr_xCuO_4$ as a function of Sr content*, Phys. Rev. B **49**, 4163 (1994).
- [77] M. Braden, P. Schweiss, G. Heger, W. Reichardt, Z. Fisk, K. Gamayunov, I. Tanaka, and H. Kojima, *Relation between structure and doping in $La_{2-x}Sr_xCuO_{4+\delta}$ a neutron diffraction study on single crystals*, Physica C **223**, 396 (1994).
- [78] O. Friedt, *Interplay between electronic, magnetic and structural instabilities in $Ca_{2-x}Sr_xRuO_4$: A neutron scattering study*, PhD thesis, Université de Paris, 2003.
- [79] T. Hahn, editor, *International Tables for Crystallography*, Vol. A: Space-group symmetry, Kluwer Academic Publishers, fifth edition, 2002.
- [80] R. Patel, C. Simon, and M. T. Weller, *$LnSrScO_4$ ($Ln=La, Ce, Pr, Nd$ and Sm) systems and structure correlations for A_2BO_4 (K_2NiF_4) structure types*, J. Solid State Chem. **180**, 349 (2007).
- [81] W. Fu, D. Visser, K. Knight, and D. IJdo, *Neutron powder diffraction study of phase transitions in Sr_2SnO_4* , J. Solid State Chem. **177**, 4081 (2004).
- [82] J. R. de Paz, M. T. Fernández-Díaz, J. H. Velasco, R. S. Puche, and J. L. Martínez, *Crystal and Magnetic Structure of $PrCaCrO_4$* , J. Solid State Chem. **142**, 29 (1999).
- [83] D. Okuyama, Y. Tokunaga, R. Kumai, Y. Taguchi, T. Arima, and Y. Tokura, *Lattice-form-dependent orbital shape and charge disproportionation in charge- and orbital-ordered manganites*, Phys. Rev. B **80**, 064402 (2009).
- [84] H. Ulbrich, *Strukturelle und dynamische Untersuchungen in 113- und 2144-Manganaten*, Diploma Thesis, Universität zu Köln, 2009.
- [85] Y. Maeno, H. Hashimoto, K. Yoshida, S. Nishizaki, T. Fujita, J. Bednorz, and F. Lichtenberg, *Superconductivity in a layered perovskite without copper*, Nature **372**, 532 (1994).
- [86] K. Ishida, H. Mukuda, Y. Kitaoka, K. Asayama, Z. Q. Mao, , Y. Mori, and Y. Maeno, *Spin-triplet superconductivity in Sr_2RuO_4 identified by ^{17}O Knight shift*, Nature **396**, 658 (1998).

- [87] H. Müller-Buschbaum and J. Willkens, *Ein Beitrag über Sr_2RuO_4 und $Sr_3Ru_2O_7$: Zur Oktaederstreckung von M^{4+} in K_2NiF_4 - und $Sr_3Ti_2O_7$ -Typ-Verbindungen*, Z. Anorg. Allg. Chem. **591**, 161 (1990).
- [88] S. A. Grigera, R. S. Perry, A. J. Schofield, M. Chiao, S. R. Julian, G. G. Lonzarich, S. I. Ikeda, Y. Maeno, A. J. Millis, and A. P. Mackenzie, *Magnetic Field-Tuned Quantum Criticality in the Metallic Ruthenate $Sr_3Ru_2O_7$* , Science **294**, 329 (2001).
- [89] B. J. Kennedy and T. Vogt, *Structural studies of rhodium doped Sr_2RuO_4* , J. Phys. Chem. Solids **63**, 2093 (2002).
- [90] M. V. R. Rao, V. G. Sathe, D. Sornadurai, B. Panigrahi, and T. Shripathi, *Metal to insulator transition in $Sr_2Ru_{1-x}Ir_xO_4$* , J. Phys. Chem. Solids **61**, 1989 (2000).
- [91] S. G. Ebbinghaus, J. Hanss, A. Weidenkaff, A. Kalytta, and R. J. Cava, *Two Ti-doped distrontium ruthenium tetraoxides: $Sr_2Ru_{0.93}Ti_{0.07}O_4$ and $Sr_2Ru_{0.81}Ti_{0.19}O_4$* , Acta. Cryst. C **59**, i35 (2003).
- [92] M. Braden, Y. Sidis, P. Bourges, P. Pfeuty, J. Kulda, Z. Mao, and Y. Maeno, *Inelastic neutron scattering study of magnetic excitations in Sr_2RuO_4* , Phys. Rev. B **66** (2002).
- [93] M. Minakata and Y. Maeno, *Magnetic ordering in Sr_2RuO_4 induced by nonmagnetic impurities*, Phys. Rev. B **63**, 180504 (2001).
- [94] M. Braden, O. Friedt, Y. Sidis, P. Bourges, M. Minakata, and Y. Maeno, *Incommensurate Magnetic Ordering in $Sr_2Ru_{1-x}Ti_xO_4$* , Phys. Rev. Lett. **88**, 197002 (2002).
- [95] N. Kikugawa, A. P. Mackenzie, C. Bergemann, R. A. Borzi, S. A. Grigera, and Y. Maeno, *Rigid-band shift of the Fermi level in the strongly correlated metal: $Sr_{2-y}La_yRuO_4$* , Phys. Rev. B **70**, 060508 (2004).
- [96] S. Nakatsuji and Y. Maeno, *Quasi-Two-Dimensional Mott Transition System $Ca_{2-x}Sr_xRuO_4$* , Phys. Rev. Lett. **84**, 2666 (2000).
- [97] S. Nakatsuji, D. Hall, L. Balicas, Z. Fisk, K. Sugahara, M. Yoshioka, and Y. Maeno, *Heavy-Mass Fermi Liquid near a Ferromagnetic Instability in Layered Ruthenates*, Phys. Rev. Lett. **90**, 137202 (2003).
- [98] L. Balicas, S. Nakatsuji, D. Hall, T. Ohnishi, Z. Fisk, Y. Maeno, and D. J. Singh, *Severe Fermi Surface Reconstruction at a Metamagnetic Transition in $Ca_{2-x}Sr_xRuO_4$ (for $0.2 \leq x \leq 0.5$)*, Phys. Rev. Lett. **95**, 196407 (2005).

-
- [99] O. Friedt, M. Braden, G. André, P. Adelman, S. Nakatsuji, and Y. Maeno, *Structural and magnetic aspects of the metal-insulator transition in $Ca_{2-x}Sr_xRuO_4$* , Phys. Rev. B **63**, 174432 (2001).
- [100] P. Steffens, O. Friedt, P. Alireza, W. G. Marshall, W. Schmidt, F. Nakamura, S. Nakatsuji, Y. Maeno, R. Lengsdorf, M. M. Abd-Elmeguid, and M. Braden, *High-pressure diffraction studies on Ca_2RuO_4* , Phys. Rev. B **72**, 094104 (2005).
- [101] O. Schumann, Röntgen- und Neutronenmessungen an Ruthenium-Verbindungen, Diploma Thesis, Universität zu Köln, 2004.
- [102] S. Nakatsuji, private communication.
- [103] M. Kriener, P. Steffens, J. Baier, O. Schumann, T. Zabel, T. Lorenz, O. Friedt, R. Müller, A. Gukasov, P. G. Radaelli, P. Reutler, A. Revcolevschi, S. Nakatsuji, Y. Maeno, and M. Braden, *Structural Aspects of Metamagnetism in $Ca_{2-x}Sr_xRuO_4$: Evidence for Field Tuning of Orbital Occupation*, Phys. Rev. Lett. **95**, 267403 (2005).
- [104] P. Steffens, *Magnetism in layered Ruthenates*, PhD thesis, Universität zu Köln, 2007.
- [105] R. G. Moore, J. Zhang, V. B. Nascimento, R. Jin, J. Guo, G. Wang, Z. Fang, D. Mandrus, and E. W. Plummer, *A Surface-Tailored, Purely Electronic, Mott Metal-to-Insulator Transition*, Science **318**, 615 (2007).
- [106] J. Baier, *Magnetoelastische Kopplung in multiferroischem $GdMnO_3$ und metamagnetischem $Ca_{2-x}Sr_xRuO_4$* , PhD thesis, Universität zu Köln, 2006.
- [107] M. Braden, W. Reichardt, S. Nishizaki, Y. Mori, and Y. Maeno, *Structural stability of Sr_2RuO_4* , Phys. Rev. B **57**, 1236 (1998).
- [108] M. Braden, W. Reichardt, Y. Sidis, Z. Mao, and Y. Maeno, *Lattice dynamics and electron-phonon coupling in Sr_2RuO_4 : Inelastic neutron scattering and shell-model calculations*, Phys. Rev. B **76**, 014505 (2007).
- [109] S. N. Ruddlesden and P. Popper, *The compound $Sr_3Ti_2O_7$ and its structure*, Acta. Cryst. **11**, 54 (1958).
- [110] S. McCall, G. Cao, and J. E. Crow, *Impact of magnetic fields on anisotropy in $Ca_3Ru_2O_7$* , Phys. Rev. B **67**, 094427 (2003).
- [111] H. L. Liu, S. Yoon, S. L. Cooper, G. Cao, and J. E. Crow, *Raman-scattering study of the charge and spin dynamics of the layered ruthenium oxide $Ca_3Ru_2O_7$* , Phys. Rev. B **60**, R6980 (1999).

- [112] G. Cao, S. McCall, J. E. Crow, and R. P. Guertin, *Observation of a Metallic Antiferromagnetic Phase and Metal to Nonmetal Transition in $\text{Ca}_3\text{Ru}_2\text{O}_7$* , Phys. Rev. Lett. **78**, 1751 (1997).
- [113] G. Cao, K. Abboud, S. McCall, J. E. Crow, and R. P. Guertin, *Spin-charge coupling for dilute La-doped $\text{Ca}_3\text{Ru}_2\text{O}_7$* , Phys. Rev. B **62**, 998 (2000).
- [114] M. N. Iliev, S. Jandl, V. N. Popov, A. P. Litvinchuk, J. Cmaidalka, R. L. Meng, and J. Meen, *Raman spectroscopy of $\text{Ca}_3\text{Ru}_2\text{O}_7$: Phonon line assignment and electron scattering*, Phys. Rev. B **71**, 214305 (2005).
- [115] G. Cao, L. Balicas, Y. Xin, E. Dagotto, J. E. Crow, C. S. Nelson, and D. F. Agterberg, *Tunneling magnetoresistance and quantum oscillations in bilayered $\text{Ca}_3\text{Ru}_2\text{O}_7$* , Phys. Rev. B **67**, 060406 (2003).
- [116] Y. Yoshida, S.-I. Ikeda, H. Matsuhata, N. Shirakawa, C. H. Lee, and S. Katano, *Crystal and magnetic structure of $\text{Ca}_3\text{Ru}_2\text{O}_7$* , Phys. Rev. B **72**, 054412 (2005).
- [117] B. Bohnenbuck, I. Zegkinoglou, J. Strempler, C. S. ler Langeheine, C. S. Nelson, P. Leininger, H.-H. Wu, E. Schierle, J. C. Lang, G. Srajer, S. I. Ikeda, Y. Yoshida, K. Iwata, S. Katano, N. Kikugawa, and B. Keimer, *Magnetic structure and orbital state of $\text{Ca}_3\text{Ru}_2\text{O}_7$ investigated by resonant x-ray diffraction*, Phys. Rev. B **77**, 224412 (2008).
- [118] W. Bao, Z. Q. Mao, Z. Qu, and J. W. Lynn, *Spin Valve Effect and Magnetoresistivity in Single Crystalline $\text{Ca}_3\text{Ru}_2\text{O}_7$* , Phys. Rev. Lett. **100**, 247203 (2008).
- [119] A. J. C. Wilson and E. Prince, editors, *International Tables for Crystallography*, Vol. C: Mathematical, Physical and Chemical Tables, Kluwer Academic Publishers, fifth edition, 2002.
- [120] G. van Rossum, Python reference manual, Technical report, CWI, 1995.
- [121] Nokia Corporation, *Qt Reference Documentation*, 2008, Version: 4.4.
- [122] Riverbank Computing Limited, *PyQt v4 - Python Bindings for Qt v4*, 2008, Version: 4.4.4.
- [123] Riverbank Computing Limited, *SIP - A Tool for Generating Python Bindings for C and C++ Libraries*, 2008, Version: 4.7.9.
- [124] Gnu general public license.
- [125] P. D. Carr, D. W. J. Cruickshank, and M. M. Harding, *The determination of unit-cell parameters from Laue diffraction patterns using their gnomonic projections*, J. Appl. Cryst. **25**, 294 (1992).

-
- [126] C. Wilkinson, J. Cowan, D. Myles, F. Cipriani, and G. McIntyre, *VIVALDI - A thermal-neutron Laue diffractometer for physics, chemistry and materials science*, Neutron News **13**, 37 (2002).
- [127] H. Roth, *Single crystal growth and electron spectroscopy of d1-systems*, PhD thesis, Universität zu Köln, 2008.
- [128] W. Kabsch, *A solution for the best rotation to relate two sets of vectors*, Acta. Cryst. A **32**, 922 (1976).
- [129] H. R. Wenk, F. Heidelbach, D. Chateigner, and F. Zontone, *Laue Orientation Imaging*, J. Synchrotron Rad. **4**, 95 (1997).
- [130] H. Luetkens, H.-H. Klauss, M. Kraken, F. J. Litterst, T. Dellmann, R. Klingeler, C. Hess, R. Khasanov, A. Amato, C. Baines, M. Kosmala, O. J. Schumann, M. Braden, J. Hamann-Borrero, N. Leps, A. Kondrat, G. Behr, J. Werner, and B. Büchner, *The electronic phase diagram of the $LaO_{1-x}F_xFeAs$ superconductor*, Nature Mat. **8** (2009).
- [131] M. Kosmala, *Strukturelle Untersuchung am 1111-FeAs-Supraleiter und halbdotierten, einfach geschichteten Perowskiten*, Diploma Thesis, Universität zu Köln, 2009.

Abstract

The subject of this thesis is the sample preparation and structural investigation of two families of the transition metal oxides.

The first class of transition metal oxide under investigation are single-layered manganites with special focus on the charge-ordering at half-doping. In addition to the synthesis of polycrystalline samples, several large single crystals were prepared with the floating zone method. The charge-ordered phase of $\text{La}_{0.5}\text{Sr}_{1.5}\text{MnO}_4$ and $\text{Pr}_{0.5}\text{Ca}_{1.5}\text{MnO}_4$ was investigated by neutron and x-ray single crystal diffraction. The charge ordering in the lanthanum/strontium compound emerges from the highly symmetric $I4/mmm$ phase with perfect aligned MnO_6 octahedra and could therefore be regarded as a very pure model system. The praseodymium/calcium compound on the other side exhibits tilted octahedra and resembles to a certain extent the situation found in the three-dimensional manganites. For both compounds the investigations presented in this thesis could definitively exclude the Zener-Polaron picture but reveal the realization of a charge- and orbital-ordered phase. Furthermore the substitution of manganese by ruthenium has been explored. This efficiently weakens the order and reduces the transition temperature. While the charge order is suppressed by inclusion of 10% ruthenium, the system stays metallic up to 30% ruthenium content.

The second class of transition metal oxides regarded in this thesis are the ruthenates. A large number of polycrystalline samples of the $\text{Ca}_{2-x}\text{Sr}_x\text{RuO}_4$ series has been prepared to follow the metal-insulator and $S\text{-}Pbca/L\text{-}Pbca$ transition at high calcium concentrations ($x < 0.2$). Furthermore the disappearance of the rotational distortion near the pure Sr_2RuO_4 was explored. Both investigations could be used to refine the existing phase-diagram of O. Friedt and P. Steffens. Finally a neutron single crystal diffraction study of $\text{Ca}_3\text{Ru}_2\text{O}_7$ is presented. This allows to determine the nuclear and magnetic structure in the paramagnetic, antiferromagnetic metallic and antiferromagnetic insulating phase.

Kurzzusammenfassung

Die vorliegende Dissertation befasst sich mit der Präparation und der Strukturuntersuchung in zwei verschiedenen Übergangsmetalloxidfamilien. Zum Einen werden einfach-geschichtete Manganate betrachtet mit einem besonderen Fokus auf der Untersuchung der Ladungsordnung bei Halbdotierung. Hierzu wurden in einem ersten Schritt sowohl poly- als auch einkristalline Proben hergestellt wobei für letztere das Zonenschmelzverfahren zur Anwendung kam. Eine Untersuchung der ladungsgeordneten Phase der beiden Verbindungen $\text{La}_{0.5}\text{Sr}_{1.5}\text{MnO}_4$ und $\text{Pr}_{0.5}\text{Ca}_{1.5}\text{MnO}_4$ erfolgte mittels Röntgen- und Neutroneneinkristalldiffraktion. Die ladungsgeordnete Phase in $\text{La}_{0.5}\text{Sr}_{1.5}\text{MnO}_4$ geht dabei aus einer hochsymmetrischen tetragonalen Phase mit der Raumgruppe $I4/mmm$ hervor, in welcher die MnO_6 Oktaeder keinerlei Verkipfung oder Rotation aufweisen. Dieses stellt damit ein besonders einfach zu behandelndes Modellsystem dar. Das System $\text{Pr}_{0.5}\text{Ca}_{1.5}\text{MnO}_4$ zeigt andererseits bereits eine Verkipfung seiner MnO_6 Oktaeder und ähnelt somit eher den stark verzerrten 3D Manganaten. Für beide Systeme konnte Struktur der ladungsgeordneten Phase bestimmt werden. Hierbei zeigte sich, dass das Zener-Polaron Modell die Struktur nicht beschreiben kann und stattdessen eine kombinierte Ladungs- und Orbitalordnung vorliegt. Weiterhin wurde für das System $\text{La}_{0.5}\text{Sr}_{1.5}\text{MnO}_4$ die Substitution von Mangan durch Ruthenium untersucht. Hierbei wurden eine starke Schwächung der Ladungs- und Orbitalordnung und ein Absinken der Übergangstemperatur beobachtet. Obwohl schon ein Austausch von zehn Prozent Mangan die Ladungs- und Orbitalordnung unterdrücken kann konnte bis zu einer Dotierung von 30 Prozent kein metallisches Verhalten beobachtet werden. Ein weiterer Schwerpunkt dieser Arbeit liegt in der Untersuchung von geschichteten Ruthenaten. Hier konnte der Phasenverlauf des Metall-Isolator- und des strukturellen Übergangs in dem System $\text{Ca}_{2-x}\text{Sr}_x\text{RuO}_4$ präzise bestimmt werden. Die hierzu benötigten Proben bei hohen Kalziumkonzentrationen ($x > 0.2$) wurden ebenfalls im Rahmen dieser Arbeit hergestellt. Weiterhin wurde in diesem System die Rotationsverzerrung untersucht, die bei hohen Strontiumkonzentrationen verschwindet. Mit diesen Daten konnte das Phasendiagramm von O. Friedt und P. Steffens verfeinert werden. Für das System $\text{Ca}_3\text{Ru}_2\text{O}_7$ wurde abschließend die Magnetstruktur in der paramagnetischen, der antiferromagnetisch metallischen und der antiferromagnetisch isolierenden Phase bestimmt.

List of Publications

- [1] **Melting of magnetic correlations in charge-orbital ordered $\text{La}_{1/2}\text{Sr}_{3/2}\text{MnO}_4$: competition of ferro and antiferromagnetic states**
D. Senff, M. Benomar, M. Kriener, O. Schumann, T. Lorenz, Y. Sidis, K. Habicht, P. Link and M. Braden
Phys. Rev. B, **77**, 184413 (2008)
- [2] **Magnetoelastic coupling across the metamagnetic transition in $\text{Ca}_{2-x}\text{Sr}_x\text{RuO}_4$ ($0.2 \leq x \leq 0.5$)**
J. Baier, P. Steffens, O. Schumann, M. Kriener, S. Stark, H. Hartmann,
J. Low Temp. Phys., **147**, 405 (2007)
- [3] **Thermodynamic Properties of $(\text{Ca,Sr})_2\text{RuO}_4$ in Magnetic Fields**
J. Baier, T. Zabel, M. Kriener, P. Steffens, O. Schumann, O. Friedt, A. Freimuth, A. Revcolevschi, S. Nakatsuji, Y. Maeno, T. Lorenz and M. Braden
Physica B, **378**, 497 (2006)
- [4] **Manual of the Cologne Laue Indexation Program**
Available at <http://clip.berlios.de>

Danksagung

An dieser Stelle bleibt mir die angenehme Aufgabe, den vielen Menschen zu danken, mit denen ich während meiner Zeit am II. Physikalischen Institut zusammenarbeiten durfte und die mich bei meiner Promotion unterstützt haben und zu deren Gelingen beigetragen haben.

Als Erstes gilt mein Dank meinem Doktorvater Markus Braden, der mir die Möglichkeit zur Promotion in seiner Arbeitsgruppe gegeben hat. Von ihm konnte ich viel über Streumethoden, Strukturen und korrelierten Elektronen lernen. Insbesondere möchte ich ihm aber für die sehr angenehme Arbeitsatmosphäre danken, die ich in seiner Arbeitsgruppe erleben durfte und die weitgehenden Freiräume die er mir bei der Ausgestaltung meiner Arbeit gewährte, ohne die z.B. mein Laueprogramm Clip nie hätten entstehen können.

Weiter möchte ich den vielen Mitgliedern des Instituts danken, die die Zeit meiner Doktorarbeit so angenehm gemacht haben: Harald Kierspel, der jederzeit ein offenes Ohr hatte, wenn ich mich mit Formularen für die Verwaltung herumschlagen musste oder Probleme mit einer der vielen Anlagen hatte. Viele der Verbesserungen für die Röntgenanlagen habe ich mit ihm diskutieren können und dabei viele wertvolle Tipps bekommen. Ralf Müller, der dafür gesorgt hat, dass nicht nur im Chemielabor immer alle benötigten Sachen zu finden waren und den man bei allen Problemen der Präparation fragen konnte. Auch hat Ralf, wie Inge Simons viele meiner Proben in der EDX untersucht. Weiter möchte ich der Feinmechanik- und der Elektronikwerkstatt für die Anfertigung einer Vielzahl von Bauteilen danken, meine Skizzen waren sicherlich selten normgerecht, trotzdem entstand meist das, was ich mir vorgestellt hatte.

Ein ganz besonderer Dank gilt meinen langjährigen Bürokollegen Daniel Senff und Paul Steffens. Ihnen bin ich in die Arbeitsgruppe gefolgt und mit ihnen habe ich lange Stunden vor dem Kryostat auf der Jagt nach dem Leck verbracht aber auch viele launige Abende auf Messreisen, Konferenzen und Weihnachtsfeiern verlebt. Auch den anderen "Bradens" möchte ich für die gute Zusammenarbeit danken. Oliver Friedt für die geduldige Einführung in Fullprof und die Röntgenstreuung, Wolf-Dieter Stein und Matthias Cwik für die Anleitungen am Einkristalldiffraktometer, Matthias Haider für die Zusammenarbeit bei der Erstellung des Messprogramms für das D5000, Thomas Finger u.a. auch für die Einsicht, dass Alt trotz des Namens tatsächlich trinkbar ist (auf Messreisen nach München, wenn in der Pension kein Bierautomaten steht), Timo Taetz mit dem ich einen sehr einprägsamen Rückweg aus Saclay angetreten bin, Martin Kosmla, der die Auswertungen zum LaFFeAs so lange verbessern musste, bis ich endlich zufrieden war, Max Baum für die Aufheiterungen beim Zusammenschreiben meiner Ar-

beit und Holger Ulbrich, der mit seinem Engagement wahrscheinlich ein würdiger Nachfolger bei der Betreuung der Röntgenanlagen geworden ist.

Den Präparateuren Holger Roth und Mohamed Benomar sei gedankt für ihre Erklärungen zur Einkristallpräparation, Martin Valldor für viele interessante Diskussionen im Chemielabor, allen Nutzern der von mir geschriebenen Programme, für das Ertragen der Fehler. Dem Administratoren-Team Jonas Weinen, Oliver Breunig und Christian Schüßler ebenfalls für gute Zusammenarbeit und meinen Nutzern für die große Geduld, auch wenn sie keinerlei Verständnis von Samba-Servern hatten und profanes "drucken-können" der eleganten Linux-Lösung vorgezogen haben. Letztlich sollten sie dies als meinen Versuch ansehen, das papierlose Büro einzuführen.

Meinen Kollegen von der Neutronova GmbH danke ich für meine ersten und leider sehr kurzen Erfahrungen in der freien Wirtschaft. Mit ihnen musste ich lernen, dass man auch die Aussagen von hervorragenden Wissenschaftlern sehr kritisch hinterfragen sollte.

Meinen Eltern danke ich für die Unterstützung in all den Studienjahren, nicht nur der finanziellen Art.

Ganz speziell möchte ich meinem Studienkollegen, Mitbewohner und besten Freund Felix besonders für die Zeit danken, in denen wir gerade nicht studiert haben. Karneval, Genever, Skiurlaube, Partys, die unvergesslichen WG-Abende und vieles andere hat sicherlich meine Studienzeit zu einer sehr, sehr schönen werden lassen.

Zum Abschluss möchte ich der wichtigsten Person in meinem Leben danken, meiner lieben Frau Silke für all die schönen Momente, die Aufheiterungen, die nahezu unendliche Engelsgeduld während meiner "kurzen" Phase des Zusammenschreibens und die kleinen Ansporne endlich mal fertig zu werden. In diesem Sinne:

Danke